1994

The diffusion and properties of an amorphous bright chromium deposit on an iron-carbon alloy substrate after 700°C exposure

Richard Paul Baron
Lehigh University

AUTHOR:

Baron, Richard Paul

TITLE:

The Diffusion and Properties of an Amorphous Bright Chromium Deposit on an Iron-Carbon Alloy Strustrate After 700 Degree C Exposure

DATE: October 9, 1994

The Diffusion and Properties of an Amorphous Bright Chromium Deposit on an Iron-Carbon Alloy Substrate After 700°C Exposure

by

Richard Paul Baron

A Thesis

Presented to the Graduate and Research Committee

of Lehigh University

In Candidacy for the Degree of

Master of Science

in

Materials Science and Engineering

Lehigh University

August, 1994

Certificate of Approval

This thesis is accepted and approved in partial fulfillment for the degree of Master of Science

August 18, 1994

Date

Professor in Charge

Chairman of Department

Acknowledgements

First, I would like to thank my advisor, Dr. A. R. Marder, for his guidance and encouragement throughout the development and completion of this research. I would also like to thank the graduate students Sean Hayes, Don Susan, Boris Levin, Kevin Stein, Steven Banovic, and Bruce Lindsley for their assistance and friendship. A special thanks goes out to Scott Bluni, John Dupont, and Dr. Brian Smith for their intellectual contributions and ideas. Also, the technical expertise of Kathy Repa and George Yasko is greatly appreciated. The "addictive" work of Wes Cherry is also duly noted. Finally, the author would like to express his eternal gratitude to A. O. Benscoter for his superhuman efforts and camaraderie. Without him, none of this work would have been possible.

Outside the confines of Whitaker Laboratory, I would like to thank my parents, Ronald and Carol Baron, for their moral and financial support. I would also like to thank my brothers, Jeff and Greg, and my sister, Cassandra, for not letting me forget the importance of family ties. The author would like to acknowledge Tony Grigas, Eileen Grudkowski, Mark Kanjorski, Mike Zubritski, and Matt Sowa for their unconditional friendship. Thanks goes to Shannon Van Meter, Amy Heckler, and Carolyn Hobbs for making my summer residence not just a house, but a "home." The comic relief of Kurt Longo and Sean Hayes is also appreciated. A special thanks goes to Chris Chambers for not letting me forget that there is more to life than just work. Finally, I would like to "Big Guy" upstairs for giving me the strength and desire to finish.

Table of Contents

List of Tables

List of Figures

Abstract

The present research investigated 700°C diffusion behavior and oxidation resistance of an amorphous bright chromium deposit (ABCD) plated onto iron-carbon alloy substrates with three initial depths of decarburization, namely 0, 200, and 400μm. The diffusion studies were conducted in a neutral atmosphere and the alloy layer growth as a function of time was characterized. The oxidation tests were performed to measure the oxide attack as the exposure time was increased and, finally, the effect of a pre-annealing treatment on the corrosion and erosion resistance was examined.

After exposure to 700°C, the amorphous chromium electroplate crystallized to αCr along with chromium carbides. The initially formed Cr_7C_3 phase was replaced by the $Cr_{23}C_6$ phase after extended exposure. Three distinct alloy layers formed between the ABCD plate and iron-carbon substrate. The three carbide layers were identified as: (1) a single phase M_7C_3 layer, (2) an M_7C_3 region with M_3C precipitates, and (3) a single phase M_3C zone. Microprobe analysis showed that the diffusion path through the 700°C iron-chromium-carbon ternary isotherm required a modification of the three phase $\alpha + M_{23}C_6 + M_7C_3$ region. Comparing the parabolic rate constants, the growth of the individual and total alloy layers appeared to be relatively independent of initial decarburization. Only the $M_7C_3 + M_3C$ layer was affected by the 400μm decarburization zone.

For the 700°C oxidation studies, the initial decarburization depth had no long-term effect on the percentage of oxide attack at the coating/substrate

interface. However, the maximum depth of oxide penetration increased with initial decarburization. After pre-annealing at 700°C up to 22 hours, carbide layer formation occurred and the percentage of oxide attack decreased. As the pre-anneal was extended to 200 hours, the carbide layer continued to increase, however, the percentage of oxide attack also increased as the morphology of the attack changed from lateral interface growth to discrete oxide particle formation. Finally, erosion behavior of as-plated and annealed ABCD coatings was tested. The room temperature steady state erosion rate for the as-plated coating was 0.105 mg/min, compared to 0.058 mg/min for the annealed coating due to the formation of the Cr_7C_3 phase in a relatively soft matrix.

I. Introduction

The number one cause of lost availability in fossil-fired electric generating units is boiler tube failures. In 1990, at each 200 megawatt and larger coal-fired steam generating unit, an average of five to six generating unit outages resulted from boiler tube failures. These failures caused losses of approximately 110,000 megawatthours and reduced the availability by 2.7 percentage points (Niebo, 1991). These losses can cost up to an estimated $700,000 per day for the large modern plants (EPRI, 1989). Hence, it is of great importance to the utility industry to reduce the number and frequency of boiler tube failures.

The cause of the boiler tube failures can be directly related to the environment that the tubes are subjected to. The tubes are attacked both internally and externally by the harsh boiler environment. The internal attack is caused by impurities flowing in the high pressure water and steam circulating through the tubes. These impurities can chemically destroy the tubes from the inside. Of more importance, however, is the external attack. High temperature combustion flames, corrosive gases, erosive fly ash, and falling slag combine for severe caustic environment on the outside of the tubes. With the large size of modern furnaces, there are several hundred miles of tube surface where failures could occur (Niebo, 1991).

Perhaps the most disturbing statistic related to boiler tube failure is that most of them are repeat failures. In other words, failures occur at the same location with the same material over and over again. These repeat failures can

be caused by insufficient determination of the initial failure. Thus, instead of applying a permanent engineering solution to a failure, a "quick fix" mechanism is often employed (Dooley, 1991). These "quick fix" solutions often include the application of a coating to repair the damage. These coatings are moderately successful for enhancing the erosion and corrosion resistance of the tubes, however, they do not provide a permanent solution -- within time, these coatings fail also. To fix the coating failure, more coating material is applied, and a never-ending cycle is set in motion.

One of the main causes of external coating failure is high-temperature corrosion damage. A popular method of combating this problem is applying a diffusion coating by chromizing. Chromizing is a surface treatment at elevated temperatures in which an alloy is formed by the inward diffusion of chromium into the base metal (ASM, 1985). Chromium has excellent resistance to wear, heat, and many corrosive mediums; thus, it is ideal for protection in the boiler environment. However, the chromizing process causes porosity, voids, columnar grains, and grain boundary carbides in the microstructure which can greatly inhibit the coating performance. Earlier studies have indicated that the detrimental voids and carbides formed during the slow furnace cooling of the chromizing process (Agarwal, 1993). If a procedure could be developed that adequately deposited chromium onto a metal substrate without the degrading the microstructure caused by the chromizing process, the life of the boiler tubes could be greatly extended.

Electrodeposition is a method of chromium deposition that shows a great deal of promise for applying chromium without the harmful effects incurred by the chromizing process. Nevertheless, electrodeposition also has its pitfalls. Upon plating, cracks could develop that act as easy paths to the base metal for corrosion products. To prevent this corrosion attack, a crack-free chromium plate can be produced by manipulating the plating conditions. Thus, the purpose of this research is to successfully produce a crack-free chromium coating and then to test the microstructural integrity of this coating at elevated temperatures in an oxidizing environment.

II. Background

II.A. Electrodeposition

Electrodeposition is the general term used to describe a process where a substance is deposited on an electrode by passing a current through an electrolyte. Electroplating is a term used to characterize the specific process of electrodepositing a metal or alloy in an adherent form on an object serving as a cathode (ASM, 1985). It is performed to change the exterior properties of the basis material. A plated object maintains the properties of the bulk material, but also benefits from the properties of the metal applied metallic coating. Many metals and their alloy systems can be electroplated, including: aluminum, copper, cadmium, chromium, gold, and nickel.

In its simplest form, the electrodeposition of a metal involves a plating

bath, a d.c. source, and two electrodes. Figure 1 (Chapman and Anderson, 1974) represents a simplified plating cell. The d.c. source supplies current flowing in one direction through the external portion of the circuit when a potential difference is imposed across the system. The current flow is that of electrons in the external conductors. The mechanism of electrical transfer in the solution is by means of electrically charged particles (ions). When the potential is applied, the positive ions (cations) travel towards the negative electrode (cathode) and negative ions travel towards the positive electrode (anode), thus completing the electrical circuit (Bunshah et al., 1982).

The deposition reactions at the cathode are characterized as reduction reactions since electrons are depleted, and the valence states of the ions involved are reduced. Conversely, at the anode, oxidation reactions occur where electrons are released and valence states are increased. Each set of reactions occurs independently of the other, but is limited by a material balance condition, i.e., the number of electrons liberated in the anodic reaction must equal the number of electrons consumed in the cathodic reaction, thus maintaining electronic neutrality.

II.B. General Chromium Electroplating

Chromium electrodeposition is commonly used as a final finishing process. There are two principal classes of chromium plating: "decorative," in which thin coatings serve as a nontarnishing, durable surface finish; and industrial (or "hard")

chromium, in which heavy coatings are applied to take advantage of the properties of chromium (Lowenheim et al., 1963). Decorative chromium coatings rarely exceed a thickness of 1.3 μm and are usually applied over undercoats of nickel or of copper and nickel. Hard chromium deposits, however, are normally deposited to thicknesses ranging from 2.5 to 500 μm and are typically applied to the base metal. Hard deposits are primarily intended to increase the service life of functional parts by increasing their resistance to 1) wear, 2) abrasion, 3) heat, and/or 4) corrosion (ASM, 1982). The protective properties of a chromium electroplate are related to the ability of chromium to maintain considerable hardness after heating to an elevated temperature (500°C) and to its excellent resistance to oxidizing atmospheres.

Chromium is electrodeposited through the interaction of a current through an electrolytic solution containing chromic acid (CrO_3) and water. The electrolytic solution usually contains between 250 g/l (conventional solution) and 400 g/l (concentrated solution) of chromic acid. However, unlike the electrodeposition of other metals (i.e. nickel), chromium can not be deposited in a solution containing only chromic acid and water. Successful electrodeposition is only achieved when a significant amount of free radicals is present. These free radicals act as catalysts and are not consumed during the process, but bring about or aid the cathodic deposition of chromium. There are two basic types of catalysts used: conventional sulfate and mixed catalyst. The conventional sulfate bath is produced by adding sulfuric acid (H_2SO_4) to the chromic acid solution. When the

conventional bath (250 g/l chromic acid) is used with 2.5 g/l of sulfuric acid, the resulting bath is commonly called "Sargent's" solution (Dupernell, 1977). Mixed catalyst solutions are produced by the substitution of fluoride ions present in complex acid radicals for a portion of the conventional sulfate catalyst. Due to the presence of these fluoride ions, mixed catalyst baths increase the current efficiency and allow for the use of higher current densities, thereby increasing the plating rate.

II.B.1. Chromium Electroplating Process

The mechanism of the chromium electroplating process has been studied extensively by Snavely (1947). In his work, Snavely proved that the plating of chromium occurs through reduction of hexavalent chromium to trivalent chromium by atomic hydrogen. This reaction occurs within a "film" created at the cathode surface. The reduction reaction requires the cathode film to maintain a pH value within certain limits (between 3 and 6) and an ample supply of atomic hydrogen. The factors governing the cathode film pH and the supply of hydrogen operate concurrently to satisfy the conditions necessary for plating. The reduction reaction described above for chromium plating is different from other metallic plating processes which occur by the direct electron transfer from cathode to metallic ion.

The normal crystal arrangement of chromium is body-centered cubic.

However, variation of the pH (within the deposition range of 3 to 6) of the cathode film can change the structure of plated chromium. When the pH of the film is at the high end of the allowable limit (pH ≈ 6), a face-centered cubic hydride is produced. When an intermediate pH (pH ≈ 4 to 5) is developed, a hexagonal close-packed hydride is formed. Only when the pH value is within a narrow range at the lower end of the allotted realm (pH ≈ 3) is the purely metallic state (body-centered cubic lattice arrangement) of chromium deposited. Between these values, a mixtures of the plate structures are produced. After the plating procedure, the face-centered and hexagonal close packed hydrides decompose to form the equilibrium body-centered cubic structure.

Since the reduction of chromic acid is accomplished by a single electron transfer, the reaction takes place in a step-wise manner. The first step involves a reaction of a chromic/chromous couple in form of the following equation: $Cr^{+6} + 3Cr^{+2} \rightarrow 4Cr^{+3}$. The trivalent chromium formed is then involved in reduction to the chromous state by atomic hydrogen within the cathode film. The reduction of this chromous state to metallic chromium occurs through an intermediate hydride. At this stage, the pH of the cathode film effects the formation of the intermediate hydride. When the pH is relatively high, hydrides of the general form $Cr_{1+n}H$ to CrH_{1+n} (where n = 0 to 1) are produced and crystallize as the face-centered cubic hydride of chromium. At intermediate pH values, hydrides of the general formula CrH_{1+n} to $Cr_{1+n}H$ (where n = 0 to 1) are formed. These hydrides have the hexagonal close-packed hydride structure of chromium and persist

during recrystallization of the plate. The normal body-centered cubic structure of chromium is formed at relatively low pH levels. In this case, hydrogen atoms reduce the chromous ions and combine with the hydroxyl ions wrestled from the chromium. Any hydrides that form when the pH is low are unstable and break up when the chromium atom assumes its position in the body-centered cubic lattice of the plate (Snavely, 1947).

The above explanation of the electroplating process is not conclusive, but due to lack of significant research in this area, it is generally accepted. Recently, however, Hoare (1989) approached the electrodeposition process from a different angle. He proposed that the electrodeposition of chromium depends upon the degree of polymerization of the chromate ions present at the cathodic surface. The degree of polymerization is, in turn, dependent on the pH of the solution. Since commonly used chromate baths are red, Hoare (1989) concluded that the active species present in the electrolytic solution is the trichromate ion, $HCr_3O_{10}^-$. The reduction of this ion can take on several different paths, depending on the number complexes present in the bath. Consequently, when the CrO_3/H_2SO_4 ratio has a value of 100/1, the maximum number of complexes exist (Hoare, 1989).

II.B.2. Chromium Electroplating Process Variables

By properly controlling the variables that control the chromium electroplating process, the desired coating properties can be produced. Many

variables affect the final integrity of the chromium plate, including bath temperature and deposition time, but the two variables that effect the chromium electroplating process the most are bath composition and current density. Essentially, these two process variables change the incidence and size of the cracks that form during the electroplating procedure. These cracks then affect the properties exhibited by the chromium coating. The effect of the process variables on the final chromium electroplate has been studied extensively and proper control of these variables is easily accomplished.

As previously mentioned, there are two basic classes of electrolytic baths utilized for chromium electroplating: conventional sulfate and mixed catalyst. For the conventional sulfate bath, the ratio by weight of chromic acid to sulfate radical is usually maintained between 75:1 and 120:1 (ASM, 1982). The variation of the current efficiency with different sulfate ratios is given in Figure 2. This figure shows that the highest current efficiency is reached when the ratio of CrO_3:SO_4^- is 100:1. Along with altering the current efficiency, varying the sulfate ratio can change the properties of the electroplate considerably. For example, at higher sulfate concentrations, the incidence of cracking decreases, however, the cracks that do form are longer and degrade the mechanical properties of the chromium plate. When the sulfate ratio reaches 150:1, only macrocracks are present and the coating disintegrates when it is not supported. At lower sulfate ratios, the cracks are more numerous, but are much smaller in size (McCormick and Dobson, 1987). These smaller cracks do not greatly degrade, and may even

increase, the mechanical properties of the chromium coating. For example, increasing the crack incidence (many small cracks) by lowering the sulfate ratio causes a corresponding rise in the ultimate tensile strength (McCormick and Dobson 2, 1987). The hardness of the chromium plate, however, is insensitive to sulfate ratio.

Mixed catalyst baths usually involve the introduction of an acid radical (i.e., fluorine) other than sulfate in the electrolyte solution. Mixed catalyst baths are used because they decrease the plating time by increasing the current efficiency. The main drawback of mixed catalyst baths is that the fluoride ion causes low-current density etching of ferrous and other metallic substrates. However, two recently developed mixed catalyst baths have overcome this etching problem. The HEEF 25 (High Efficiency Etch Free, 25% current efficiency) (Jones, 1989) and ANKOR 1126 (Klein, 1987) baths utilize mixed catalysts to increase the allowable current density without etching or burning the substrate. This increase in permissible current density increases the current density that can be obtained.

While the above mixed catalyst baths improve the plating process, they still produce a microcracked plate. Thus, their corrosion resistance is no greater than the corrosion resistance exhibited by chromium plates produced from a conventional bath. One type of mixed catalyst bath procedure that produces a plate with increased corrosion resistance is called the amorphous bright chromium deposition (ABCD) method. The ABCD method involves the addition

of organic compounds containing a -CHO or -COOH group such as formamide, formaldehyde, or formic acid to the electrolytic bath. These additions produce an amorphous bright chromium plate that has no pinhole or crack defects, thereby increasing the corrosion resistance (Hoshino et al., 1986). This plating method is relatively new and is explained in further detail in subsequent sections.

The current density also has a strong effect on the structure of the chromium electroplate produced. The current density is closely related to the temperature of the bath, changing one variable usually requires a concurrent change in the other variable. The variation in the appearance of the deposits with current density and temperature in a conventional sulphate bath is shown in Figure 3. When the sulfate ratio is maintained within the range of 80:1 to 110:1 and proper adjustments of the bath temperature are made, the average length of cracks decreases at very low current densities (20 A/dm^2). As the current density is raised into the range of 30 - 50 A/dm^2, the crack length appears to increase slightly and past a current density of 50 A/dm^2, the crack length remains relatively constant (McCormick and Dobson 2, 1987). When the temperature is not adjusted accordingly, however, an increase in the current density causes an increase in porosity and crack incidence (Blum et al., 1931). Figure 4 shows how the crack incidence varies with current density at different sulfate ratios and Figure 5 depicts how the mean crack length varies with these variables. Both graphs represent data generated at a constant bath temperature of 55°C.

As mentioned above, the extent of cracking in the chromium plate dictates

the properties of the chromium plate. For example, the adhesion and ultimate tensile strength of the chromium plate are greatest at low current densities when the crack incidence is high (McCormick and Dobson 2, 1987). Many small cracks are not as detrimental as a few large cracks which could cause catastrophic failure at low stresses. The hardness of the chromium plate, however, increases from 800 HV to 1000 HV when the current density is raised from 20 to 75 A/dm^2 (McCormick and Dobson, 1987). The variation in microhardness with sulfate ratio and current density is given in Figure 6.

Along with the structure of the chromium plate, the current density also effects the electrodeposition process. Again, with the proper adjustments in temperature, an increase in the current density causes an increase the cathode efficiency and, thus, an increase in the deposition rate.

II.C. Theories of the Formation of Cracks

One of the main reasons why chromium is electroplated to a base metal is to increase the corrosion resistance of the component. However, by using the conventional chromium electrodeposition methods, a cracked electroplate is often produced. Along with degrading the overall mechanical properties of the electroplate, these cracks can form a network of open channels from the plated surface to the base metal. These channels can act as fast diffusion paths for corrosive elements and the chromium plate no longer provides adequate protection. Thus, to avoid the formation of these easy diffusion paths, the

production of a crack-free chromium plate is highly beneficial to increase the corrosion resistance.

It is generally believed (Snavely, 1947) (Wilson and Turley, 1989) (Saiddington and Hoey, 1974) (Brittian and Smith, 1956) that the formation of cracks occurs because of the contractile stresses that build up during the electroplating process. Under normal plating conditions, these stresses usually reach criticality at a deposition thickness of 0.5 μm. Many theories have arisen as to the source of these contractile stresses. Cleghorn and West (1966) have suggested that the observed stress is caused by lattice misfit induced by the rapid diffusion of hydrogen away from the coating-substrate interface. Kushner (1973) proposed the following five theories for the stresses created during electrodeposition: (1) Metals with high overpotentials have much excess energy during electrodeposition and when these metals adhere to the substrate, this excess energy is released in the form of heat. This heat expands the crystal lattice. As the crystal lattice cools to normal size a stress is produced. (2) Matter in the form of oxides, hydrates, etc. is occluded in the grain boundaries of the depositing metal. If this occluded matter undergoes a volume change due to chemical or physical processes, the stress state of the overall deposit could be altered. (3) During electroplating, a metal is being formed on the substrate by the continuous stacking of atomic layers. If one of these layers does not nucleate correctly, a dislocation could be formed. These dislocations could build up a form a considerable internal stress. (4) As crystals of the depositing metal are nucleated,

restraints arise from the adhesion to the base metal. With continued nucleation and growth of these crystals, the restraints build up and internal stress is formed. (5) Hydrogen is taken up during electrodeposition (as molecular hydrogen or as a hydride), and a dilation of the host lattice occurs. As this hydrogen diffuses out, a contraction of the lattice develops and a stress is produced. This last theory is analogous to the concept proposed by Cleghorn and West (1966).

The most accepted theory involves the hydrogen uptake during electrodeposition. In his classic paper, Snavely (1947) explains how the presence of hydrogen in the plating bath effects the structure of the final chromium electroplate. As previously mentioned, chromium can be deposited in three different crystal structures, depending on the pH of the immediate film at the cathode. At high pH values, a hydride with the face-centered cubic crystal structure is deposited; at intermediate pH values, a hydride with the hexagonal arrangement is deposited; at low pH values, the chromium metal is deposited in with the body-centered cubic arrangement. After deposition, the face-centered cubic and hexagonal hydride crystals will decompose to form the equilibrium body-centered cubic structure. This decomposition from face-centered or hexagonal to a body-centered cubic structure causes a considerable volume shrinkage. If a completely unstrained body-centered cubic arrangement is assumed to be the final structure, the volume shrinkage associated with the decomposition of the hydrides could be as much as 15%.

The amount of overall shrinkage depends on the dominate crystal structure

that is deposited which, in turn, depends on the pH of the cathode film. For example, if the pH of the cathode film is such that a mixture of body-centered and hexagonal crystals is plated, the amount of shrinkage depends upon the relative amounts of body-centered and hexagonal crystals. If the plate is predominately body-center cubic, a small amount of overall shrinkage will occur when the hexagonal crystals decompose to produce the equilibrium body-centered cubic structure. The strains produced by this small amount of shrinkage may lie within the elastic and plastic deformation limits of the chromium plate, and hence, no cracking will occur. However, if the plate is predominately hexagonal crystals, the amount of decomposition to the body-centered cubic arrangement will produce a shrinkage so great that the elastic and plastic deformation limits of the plate will be exceeded and cracking will occur (Snavely, 1947). The more crystals that decompose, the more extreme the amount of shrinkage and, thus, the greater the number of cracks.

When the number of cracks increase, the average length of each crack decreases. This behavior is related to the proportion and stability of the hydride crystals in the deposit. If the plate contains only a small amount of hexagonal hydride, the contractile stresses produced may not be high enough to cause cracking. Thus, cracks may not be produced until all the hydride crystals in the plate have decomposed. This may require so much time that, when cracking finally does occur, the plate is thick and the cracks are relatively long. If a large proportion of unstable hydride is deposited, the hydride crystals will decompose

quickly and produce cracks in thin layers of plate. When the cracking occurs rapidly, many cracks are produced and the length of the cracks are limited to the thickness of the plate layer. Generally, under normal plating conditions, cracking begins when the plating thickness reaches 0.5 μm.

As the plating procedure continues, old cracks are sealed over with chromium and new cracks develop. Since the contractile stresses in the underlying "cracked" layer of chromium plate have been relieved, the new cracks that develop extend from the surface to this unstressed layer. Therefore, the length of the cracks is indicative of, but not an absolute measure of, the thickness of plate in which hydride decomposition is occurring at any given time during the plating process (Snavely, 1947).

II.D. Amorphous Bright Chromium Deposition

Several methods have been introduced to produce a crack-free plate. One of the most popular method involves the manipulation of the electrodeposition circuit (Wilson and Turley, 1989) (Saiddington and Hoey, 1974). Many different techniques have been attempted and they can all be grouped under the generic term "pulse plating". All the various "pulse plating" techniques involve stopping the chromium plating process before the critical thickness of 0.5μm is reached. Under the proper conditions, a new unstressed chromium layer is deposited once the plating process is re-initiated. By repeating this "on-off-on" plating procedure, numerous uncracked layers can be deposited to produce a thick crack-free

chromium plate.

Along with manipulation of the electrodeposition circuit, the composition of the electrolytic bath can also be altered to produce a crack-free plate. In the amorphous bright chromium deposition method (ABCD), the bath contains formic acid (HCOOH), along with the usual components of chromic acid (CrO_3) and sulfuric acid (H_2SO_4). The standard ABCD solution consists of 100 g/l of chromic acid, 5 g/l of sulfuric acid, and 20 ml/l of an 85% solution of formic acid (Hoshino et al., 1986) (Tsai and Wu, 1989). The ABCD bath yields a chromic acid to sulfuric acid ratio of 20:1, compared to the common ratio of 100:1 for conventional chromium plating.

The standard ABCD bath is operated at a temperature of 30°C and a current density of 40 A/dm^2. The anodes for the ABCD bath are 5-7% antimony-lead. Under proper operating conditions, the current efficiency can reach as high as 30% (Tsai and Wu, 1990). This current efficiency is significantly higher than the 12% which is normally obtained in conventional chromium plating baths and the 25% which is achieved using mixed catalyst baths like the HEEF 25 process (Jones, 1989). For the ABCD method, the deposition rate can be as high as 40μm/hour.

To reach higher current efficiencies in the ABCD technique, the bath temperature can be lowered. Figure 7 shows the variation in current efficiency with bath temperature and with other plating variables for the ABCD technique. In contrast, for the conventional chromium plating process, the temperature of the

bath would have to be lowered and the current density would have to be raised to increase the current efficiencies. Under these conditions, "burning" of the plate is likely to occur (Dennis and Such, 1993).

II.D.1. Effect of Formic Acid Additions

Generally, the role of an organic additive is to inhibit the growth of metal crystals during electrodeposition. The organic additive absorbs on the surfaces of small crystallites and restricts growth, resulting in an amorphous layer. Tsai and Wu (1990) found that the phase of the deposited chromium is dependent upon the amount of formic acid in the solution. The three phases found in their research were α, β, and amorphous chromium phases. The α phase has a body-centered cubic structure and is the normal phase of electrodeposited chromium. It is the phase present at low concentrations of formic acid (below 0.6 ml/l). As the concentration of formic acid is increased (up to 8 ml/l), the β phase becomes dominant. The β phase is actually a chromium hydride (CrH_x) with a hexagonal crystal structure. At higher concentrations (above 8 ml/l), the amorphous chromium phase is present.

Additions of formic acid also have an effect on the amount of interstitial carbon and hydrogen in the as-deposited chromium. Figure 8 (Tsai and Wu, 1990) displays the effect of formic acid concentration on the hydrogen and carbon content in the chromium plate. The figure also indicates the resulting phase as a function of formic acid content. When the formic acid concentration is low, the

amount of interstitial hydrogen and carbon is low and the resulting phase is the normal body-centered cubic α phase. The highest hydrogen content occurs simultaneously with the presence of the β phase at approximately 3 ml/l. This result is not surprising, since the β phase is basically a hydride. As the formic acid content is increased past approximately 5 ml/l, the amount of the hydrogen decreases dramatically. This behavior correlates well with the well-known fact that the ample addition of an organic additive encourages hydrogen absorption (Snavely, 1947).

Figure 8 also shows that the carbon content in the as-deposited plate increases consistently with formic acid content, indicating that the formic acid supplies the carbon in the plate. On the as-plated surface, the carbon has been found to be both graphitic and in the form of -COOH (Hoflund et al., 1986). Higher additions of formic acid also correlate to the formation of the amorphous phase. Thus, the presence of interstitial carbon and absence of interstitial hydrogen acts to stabilize the amorphous chromium phase.

Along with regulating the chromium phase and amounts of interstitial hydrogen and carbon deposited, the formic acid also effects the current efficiency. Figure 9 (Tsai and Wu, 1990) displays how the current efficiency changes with formic acid content. The resulting phase is also indicated. The current efficiency can reach a maximum of 40%, far higher than the conventional single catalyst bath. In effect, the formic acid acts as another catalyst in the solution, making the electrodeposition process more efficient.

II.D.2. Microstructure of Amorphous Plate at Elevated Temperatures

Since the overall purpose of crack-free amorphous deposition is corrosion protection at elevated temperatures, the integrity of the deposit as the temperature is increased is very critical. Generally, as the temperature of an amorphous solid is increased, crystallization can occur.

Tsai and Wu (1989) subjected amorphous plates to 1 hour anneals at different temperatures. Using TEM and differential scanning calorimetry, they found that the structure of the plates remained amorphous up to temperatures of 200°C. The first dispersoids of metallic chromium were found to develop at a temperature of 273°C. The grain size of these dispersoids were few in number and small, on the order of 300Å. When the temperature was raised to 400°C, the dispersoids were more numerous and grew to a size of 1000Å.

The first precipitation of a chromium carbide, Cr_7C_3, was observed when the annealing temperature was raised to 480°C. The Cr_7C_3 carbide crystallized inhomogeneously from the carbon-rich matrix between the chromium dispersoids. At 480°C, the dispersoids themselves grew a size of 2700Å.

Besides the continued growth of the chromium dispersoids, not much happened to the structure of amorphous plate as the temperature was increased to 700°C. Above 700°C, abnormal grain growth of the dispersoids occurred, resulting in grains approximately 5000Å in size. Also, at 710°C, another chromium carbide, $Cr_{23}C_6$, began to precipitate, replacing Cr_7C_3. When the temperature reached 750°C, the replacement was complete.

II.D.3. Properties of the Amorphous Plate at Various Temperatures

Because it is essentially crack-free, the amorphous electrodeposit has superior corrosion resistance compared to the conventional chromium plate. Figure 10 (Hoshino et al., 1986) compares the dissolution rates between the as-deposited amorphous chromium and conventional chromium in a hydrochloric acid (1:1) solution at 30°C. The corrosion rate of the amorphous plate is approximately 1/3 that of the conventional chromium deposit.

Figure 10 also contains the dissolution rates of the amorphous chromium plate after an annealing operation at different temperatures. As the annealing temperature is increased up to 300°C, the dissolution rate of the amorphous plate decreases. This increase in corrosion resistance with temperature results from the formation and growth of chromium metal crystals. From 400°C to 700°C, although the corrosion rate is still lower than the conventional plate, the corrosion rate of the amorphous plate increases. This increase in corrosion resistance results from the formation of two chromium carbides, Cr_7C_3 (at 480°C) and $Cr_{23}C_7$ (at 710°C). The formation of these carbides depletes the grain boundaries of chromium, thereby making the plate more susceptible to corrosive attack.

Unlike the conventional chromium plate, deposits fabricated with the ABCD process actually increase in hardness with increasing temperature. Figure 11 (Hoshino et al., 1986) shows the Vickers hardness values for amorphous plates and conventional plates as a function of annealing temperature. Whereas the conventional plate experiences a continuous decline in hardness with increasing

temperature, the amorphous plate increases in hardness to a maximum Vickers hardness value of approximately 1700 at 500°C. The maximum hardness results from a microstructure consisting of a uniform distribution of small chromium dispersoids (less than 3500Å) in a carbide matrix of Cr_7C_3 (Tsai and Wu, 1990).

As the temperature is increased above 500°C, grain growth continues past the optimum size and, as a result, the hardness decreases. When the temperature reaches approximately 700°C, abnormal grain growth occurs and $Cr_{23}C_7$, a soft carbide, begins to replace Cr_7C_3. The result is a dramatic decrease in hardness. However, this hardness value is still considerably higher than the hardness value for the conventional plate at the same temperature.

II.E. Diffusion

One of the purposes of this project is to study the diffusion behavior of carbon through a decarburized region in a low alloy steel plated with chromium. Hence, a review of the basic diffusion principles is necessary. The general equation for Fick's law is given by

$$\frac{dc}{dt} = D\frac{d^2c}{dx^2}$$

in which D is assumed to be independent of concentration. For a semi-infinite solid, the above general diffusion equation can be approximated by the solution

$$1 - \frac{c}{c_o} = -\frac{2}{\sqrt{\pi}} \int_0^{\frac{x}{2\sqrt{Dt}}} e^{-y^2} dy$$

where **c** is the concentration of the diffusing element at a depth **x** after a time **t**, c_o is the surface concentration of the diffusing element, and, finally, **D** is the interdiffusion coefficient over the concentration range c_o to **c**.

Upon integration, the above integral yields,

$$x^2 = 4ADt$$

where **x** is the thickness of the diffusion layer after a time **t**, **A** is a constant derived from the boundary conditions **c** and c_o. The constant **A** is seen to vary with carbon content and temperature, but its value lies close to unity (Menzies and Mortimer, 1966).

The interdiffusion coefficient, **D**, is calculated by plotting the squared thickness of the alloy layer versus the exposure time. If the growth of the alloy layer is indeed diffusion controlled, this plot will be a straight line. From the above equation, the slope of this line is the interdiffusion coefficient (multiplied by a constant) for that particular alloy layer.

After finding the interdiffusion coefficient, **D**, from the above equation, the activation energy and frequency factor, or diffusivity, can be found by using the Arrhenius relation

$$D = D_o e^{\frac{-E}{RT}}$$

where D_o is the diffusivity, **E** is the activation energy, **T** is the absolute temperature, and **R** is the gas constant.

To successfully characterize the diffusion with the proposed system, the properties of the principal elements involved and how they interact with each other must be considered.

II.E.1. Primary Elements

Iron:

Three solid phases of iron exist. Below 912°C (1674°F), the stable solid phase of iron is the alpha (α) phase. This phase commonly called ferrite and it has the body-centered cubic (BCC) structure. Between 912° (1674°F) and 1394°C (2541°F), the stable solid phase of iron becomes gamma (γ) iron, or austenite. Austenite has the face-centered cubic (FCC) crystal structure. Since the FCC crystal structure is more densely packed than the BCC crystal structure, there is a ≈ 1% contraction in volume during the $\alpha \rightarrow \gamma$ transformation. Above 1394°C (2541°F), this austenite phase transforms to delta (δ) iron. Like ferrite, this phase has the BCC crystal structure. Again, because of the difference in density between the FCC and the BCC structures, there is a 0.5% expansion upon the $\gamma \rightarrow \delta$ transformation. Finally, at a temperature of 1537°C (2798°F), the δ-iron phase melts (ASM, 1985). Another temperature of interest is the ferromagnetic Curie

temperature of iron. It lies between 767° and 771°C.

The degree of solubility of the added elements in the FCC or BCC iron determine the phase equilibria of binary and higher systems. Solid solutions in FCC iron are denoted by γFe and solid solutions in BCC iron are designated by αFe or δFe. The notation αδFe indicates that αFe and δFe are continuous in the BCC solid solution (Rivlin, 1984).

Carbon:

Carbon can have four different solid phases: graphite, rhombohedral graphite, diamond, and hexagonal diamond (ASM, 1985). The only phase pertinent to this study is graphite, the most commonly occurring phase of carbon. Graphite has the hexagonal cubic structure up to a temperature of 3727°C (6740°F) at which carbon sublimes.

Chromium:

The stable form of chromium has the body-centered cubic lattice. Other forms of chromium, i.e., hexagonal and face-centered cubic, have been reported to exist when chromium is electrodeposited, but these can not be considered true allotropes of chromium (Sully, 1954). Because of its high reactivity, high purity chromium is difficult to obtain and, thus, measurement of the melting temperature of chromium is difficult. The accepted mean melting temperature of chromium is 1878±22°C (3412±72°F) (Rivlin, 1984).

II.E.2. Binary Systems

Iron-Carbon:

The iron-carbon system has been widely studied and different segments of this binary phase diagram is shown in Figures 12a, 12b, and 12c. The iron-carbon crystal structure data is given in Table 1. The composition range of carbon in γFe (FCC) can be as high as 2.0 weight percent. However, when iron has the BCC structure, as for δFe and αFe, the maximum carbon composition drops to 0.1 weight percent in δFe and 0.05 weight percent for αFe (Rivlin, 1984).

The diffusion of carbon in iron follows the Arrhenius relation given above and depends heavily upon the magnetic state of iron. Below approximately 770°C (1418°F), the Curie temperature (T_c), ferromagnetic state of iron exists and the diffusion of carbon has the following properties: $D_o = 7.9 \times 10^{-3}$ cm²/s and E = 75280 J/mole. Above 770°C (1418°F), iron undergoes a transition from ferromagnetic to paramagnetic. This transition effects the carbon diffusion; the new values for the Arrhenius expression are: $D_o = 8.1 \times 10^{-3}$ cm²/s and E = 82500 J/mole (Varotsos et al., 1988).

Iron-Chromium:

The iron-chromium phase diagram is given in Figure 13 (ASM 2, 1990). The accompanying crystal structure data for the iron-chromium system is given in Table 2.

This system has a much wider range of solid solubility than most binary systems; chromium and BCC iron dissolve in all proportions from chromium to

iron. The continuous solid solution αδFE forms from the unification of αFe and δFe at over 12 weight percent chromium. This phase is stable up to the solidus. As a result, the range of the γFe (FCC) is restricted. Thus, chromium is a stabilizer of αδFe. At 820°C (1508°F) and 46 weight percent chromium, the σ-phase forms congruently from the αδFe phase. This σ-phase determines the phase equilibria below 800°C (1472°F). Below 820°C, a eutectoid decomposition to Fe-rich (αδFE) and Cr-rich (Cr) BCC phases takes place. Over the eutectoid temperature of 440°C, metastable αδFe and (Cr) can form at the expense of the σ-phase. The type of sluggishness behavior of all the reactions involving the sigma phase has caused dispute concerning its placement on the equilibrium phase diagram (Rivlin, 1984).

Like carbon, the diffusion of chromium in iron is contingent on the magnetic state of the iron atom. Below its Curie temperature (≈ 770°C), iron is in the ferromagnetic state and the diffusion characteristics of chromium in iron are governed by: D_o = 0.44 cm²/s and E = 253530 J/mole. In the paramagnetic state of iron, chromium has the following diffusion properties: D_o = 8.52 cm²/s and E = 251720 J/mole (Varotsos, 1988).

Chromium-Carbon:

The pertinent areas of the phase diagram of the chromium-carbon binary system is given in Figure 14. Special points with the chromium-carbon system and crystal structure data for the carbon-chromium system is given in Table 3.

The equilibria phases in the chromium-carbon system are dominated by

three carbides of chromium, $Cr_{23}C_6$, Cr_7C_3, and Cr_3C_2. Each of these carbide compounds has a limited range of solubility (indicated by the broken lines in the phase diagram) (Rivlin, 1984) and are often referred to as "line compounds."

Carbon has limited solid solubility in chromium, only extending to 0.07 weight percent carbon at the eutectic temperature of 1534±10°C (ASM, 1990). The Cr_7C_3 and Cr_3C_2 compounds form peritectically and $Cr_{23}C_6$ can form either eutectically or peritectically.

As a summary for the chromium-carbon and iron-chromium binary systems, Table 4 depicts the characteristics of the binary solid phases found in these systems.

II.E.3. Ternary System

Much information is available on the iron-chromium-carbon system at elevated temperatures. Since the research proposed will deal with diffusion studies at 700°C (1292°F), only the isothermal section (Figure 15) dealing with this temperature will be addressed. By close inspection of Figure 15, $M_{23}C_6$ dissolves up to 35 weight percent iron, but this figure rises to 50 weight percent iron in M_7C_3. The equilibrium amount of ferrite in both these carbides contains 5.6 weight percent carbon (Rivlin, 1984). Some disagreement exists as to the amount of chromium that can replace iron in M_3C. Kou (1953) found that chromium is seen to replace iron in M_3C up to approximately 18 weight percent chromium. However, Jellinghaus and Keller (1971) found this value to be as high as 25

weight percent chromium.

Jellinghaus and Keller (1971) also proposed the existence of two three-phase equilibria, $\alpha Fe + \sigma + M_{23}C_6$ and $(Cr) + \sigma + M_{23}C_6$ divided by a two-phase region $\sigma + M_{23}C_6$. Solubility of carbon in this σ phase is negligible. Although no definitive values of carbon solubility in σ phase at 700°C were obtained, earlier studies determined that the solubility of carbon in 43 weight percent chromium at 595°C (1103°F) is approximately 0.016 weight percent. The existence of this sigma phase, however, has only been observed in alloys which had not been homogenized.

As a summary for the phases in the ternary iron-chromium-carbon system at low temperatures, Table 5 shows the tie lines between αFe, γFe, and M_3C at 770, 750, and 700°C.

II.E.4 Previous Diffusion Studies with Electrodeposited Chromium Coatings

Agarwal (1993) performed diffusion studies on the Fe-Cr-C system at two different temperatures, 600° and 1000°C. His research involved the diffusion of an pure electrodeposited chromium layer on the top of a decarburized region of a steel (0.2% carbon) substrate. Below the decarburized (ferritic) region, the microstructure was pearlitic.

After 500 hours at 600°C, Agarwal (1993) found that two thin reaction layers formed under the chromium plate. A micrograph of this reaction layer is shown in Figure 16. Through microprobe analysis, the upper layer consisted

mainly of carbides in the form of $M_{23}C_6$. Since solubility of carbon increases from 0.005 wt% at room temperature to 0.1 wt% at 600°C in the ferritic region, the movement of carbon through the decarburized region to the chromium plate is greatly enhanced. The exact composition of the lower layer was not determined, but it was believed to be either an iron-rich layer with chromium and carbon in solid solution or a ferritic layer containing fine carbide precipitates.

When Agarwal (1993) increased the exposure temperature to 1000°C, the ferritic region directly below transformed into austenite. Since the solubility of carbon is much greater in austenite (2.0 wt%) than it is in ferrite (0.02 wt%), the uptake of carbon was significantly enhanced (ASM, 1990). After only 4 hours of exposure at 1000°C, pearlite formed throughout the decarburized region on cooling as a result of the redistribution of carbon.

Due to the uneven thickness of the decarburized regions, two distinct microstructures were formed. In the regions of thinner decarburized layers, the presence of the chromium layer enhanced the eutectoid reaction of austenite (γ) to pearlite (α + Fe_3C). At the thicker decarburized regions, a typical chromized microstructure formed. The region consisted of voids and grain boundary carbides; no pearlite was produced. The concentration profile of carbon was not high enough to induce the eutectoid reaction.

At both exposures temperatures, Agarwal (1993) discovered that the reaction layers below the chromium electroplate grew at a parabolic rate with time, indicating diffusion-controlled growth. He also produced a considerable

decarburized region below the chromium layer *after* the 1000°C heat treatments. During the exposure at 1000°C, the presence of the chromium layer caused a significant uptake of carbon in the form carbides, thereby depleting the adjacent region of carbon. This behavior signifies the large affinity chromium has for carbon.

II.E.5. Diffusion Studies on Chromized Coatings

Much work has been performed on the diffusion of chromium into base metals during the chromizing process. Even though the chromizing process commonly operates at temperatures around 1000°C, the information obtained concerning the alloy layer formation and diffusional behavior should be applicable to the present study performed at 700°C.

Although the formation of alloy layers during chromizing is highly dependent on the processing parameters and the base material, three types of carbides are commonly encountered: $M_{23}C_6$, M_7C_3, and M_3C (Zancheva et al., 1978) (Glowacki and Kabula, 1982) (Kabula and Wachowiak, 1983). The $M_{23}C_6$ carbide is a chromium-rich carbide found near the surface of the chromized coating (close to the chromium source) after sufficient diffusion has occurred. The M_7C_3 carbide has a needle-shaped and columnar morphology and readily forms directly below the $M_{23}C_6$ carbide layer. Finally, the M_3C carbide is composed of coarse-grained blocks and forms adjacent to the iron-carbon source.

Kabula and Foct (1987) performed extensive studies concerning the growth

of the three carbide layers on different substrates. They found that the double layer of M_7C_3 and M_3C commonly form on hypoeutectiod steels at temperatures below A_1. In this temperature range, the growth of the intermediate M_3C layer takes place on a matrix composed of ferrite and cementite. They also discovered that the appearance of the $M_{23}C_6$ carbides is contingent on the chromizing environment. A chromizing medium low in carbon and high in chromium promotes the formation of the $M_{23}C_6$ carbide layer.

Although the aforementioned three carbide layers are often found during the chromizing procedure, the ternary diffusion mechanisms that dictate the carbide layer formation are unknown. While it is widely accepted that the carbide layers inhibit interdiffusion, which diffusing element is required for further layer growth is uncertain. Glowacki and Kaluba (1982) determined that the growth of the carbide layers is controlled by the diffusion of chromium through the M_7C_3 layer. On the other hand, Zancheva et al (1978) found that the diffusion of carbon regulates the growth of the carbide layers.

Instead of attempting to interpret the complex ternary diffusion behavior in the Fe-Cr-C system at temperatures above 900°C, previous research has focused on the parabolic rate constants associated with the alloy layer growth. When the growth of the layer is diffusion controlled, the alloy layer thickness grows at a parabolic rate with exposure temperature. Plotting the thickness as a function of the square root of time produces a straight line. The slope of this line is called the parabolic rate constant, or k_p. This parabolic rate constant can then be

squared to give a crude interdiffusion coefficient for the growth of the alloy layer during the chromizing process (Zancheva et al., 1978) (Menzies and Mortimer, 1966). Zancheva et al (1978) calculated the parabolic rate constants for the whole layer of carbides in a chromizing environment at 1000°C. His parabolic rate for steel substrates that contained 0.2% carbon produced an interdiffusion coefficient of $4x10^{-11}$ cm^2/sec. When he increased the amount of carbon in the steel substrates to 0.45%, the interdiffusion coefficient increased slightly to $13x10^{-11}$ cm^2/sec.

In their classic chromizing paper, Menzies and Mortimer (1966) studied the interdiffusion coefficient for chromizing as a function of chromizing temperature and carbon content in the steel. At a chromizing temperature of 950°C and a carbon content of 0.04 weight percent, Menzies and Mortimer (1966) found the interdiffusion coefficient of the chromized coating to be $2.6x10^{-10}$ cm^2/sec. When the carbon content in the steel was increased to 0.16 weight percent, the interdiffusion coefficient dropped to $7.0x10^{-11}$ cm^2/sec. This decrease in interdiffusion coefficient of chromized coating with increasing carbon content suggests that carbide formation inhibits the diffusion of chromium into the steel.

III. Experimental Procedure

III.A. Substrate Preparation

The substrate material was a high purity iron-carbon alloy. The chemical composition of the alloy (in weight percent) is given below.

Fe	C	Cu	P	S	Si	Ni	Cr
BAL	0.20	0.002	<0.003	0.003	<0.01	0.01	<0.01

The substrates were machined to rectangular coupons with dimensions 38x19x3mm. The coupons were then ground on 120 grit to remove any predominant burs and oxide formation.

III.A.1. Decarburization of Substrates

To remove any excess oils and dirt, the samples were ultrasonically cleaned in alcohol. The samples were then coated with Carburizing Stop-Off LX 1397, a commercially available stop-off from the Heatbath Corporation, to prevent any unnecessary decarburization. The stop-off paste was only applied to one 38x19mm face of the sample. The samples were air dried for at least eight hours to ensure that the paste had sufficiently solidified.

A schematic diagram of the decarburization set-up is shown in Figure 17. Only one sample was decarburized at a time. With the protected face lying face down, the sample was placed in the tube furnace at the "hot spot." The "hot spot"

was determined through several furnace mappings. When the external temperature of the furnace was set at approximately 400°C, the "hot spot" consistently reached temperatures of 815°C (±5°C). This temperature was found in the literature to be the optimum temperature for most efficient decarburization rate (Marder et al., 1985). The sample was oriented in the furnace so that the 19mm dimension was parallel to the direction of the tube furnace.

Both ends of the tube furnace were sealed with metallic covers that allowed for the introduction and removal of gas atmospheres. When the furnace was turned on, the furnace tube was purged with pure argon gas. This argon purge served to inhibit any bulk oxidation of the sample as it reached temperature by removing as much oxygen as possible from the furnace tube. Excess oxygen and moisture was removed from the argon gas itself as it passed through the two corresponding filters (Figure 17). The argon gas also passed through a bubbler filled with tap water. Being an inert gas, however, argon did not absorb water and carry it through the furnace tube. The argon was allowed to exit the tube furnace through a tube at the end of the furnace that lead to a bunsen burner. This bunsen burner was also connected to an outside gas line so it could be ignited without gas flow from the tube.

By welding thermocouple wire to a typical sample, the temperature profile with time was determined. The sample took approximately 24 minutes to reach the desired temperature of 815°C. Therefore, to ensure uniform temperature throughout, the sample was heated under the argon atmosphere for 30 minutes.

After the heat-up/purge stage, the argon gas was turned off at the source and bled through the system. When an ample amount of argon was removed from the tubes, the decarburizing gas mixture was turned on. This gas mixture had the composition of 82% nitrogen and 18% hydrogen. This particular gas mixture is commonly used to decarburize steel components (Agarwal, 1993) (Marder et al., 1985). Like the argon gas, the N_2-H_2 mixture passed through successive filters to remove any excess oxygen and moisture from the gas (Figure 17). Unlike the argon gas, however, as the N_2-H_2 mixture passed through the bubbler, a significant amount of water was absorbed by the gas. This "wet" atmosphere is necessary for the decarburization mechanism to occur. To ensure that no excess hydrogen escaped to the environment surrounding the tube furnace, the gas mixture was burned after exiting the furnace at the bunsen burner.

The "duration" of the decarburization was defined as the actual time that the sample was exposed to the N_2-H_2 gas atmosphere at temperature (815°C). Of course, the longer the exposure, the deeper the decarburization depth. Two exposure times were employed, namely 1 hour and 2 hour.

After the particular exposure time was reached, the external temperature control of the furnace was turned off and the N_2-H_2 gas mixture was turned off at the tank. After the tubes were sufficiently free of the decarburizing gas, the argon gas was again turned on to purge the furnace of the N_2-H_2 gas mixture as the sample cooled down. The sample was allowed to furnace cool under a argon

atmosphere for 30 minutes. After the 30 minutes, the sample was removed and quenched in cool water.

III.A.2. Pre-plating Sample Grind, Polish, and Mask

After the decarburization process, the thicknesses of the samples were recorded. To produce the desired decarburization depths of 200μm and 400μm, the samples were ground from a 60 to a 600 grit finish. After each grinding step, the samples were measured to determine the extent of material removed. The samples were then polished to a 6μm diamond finish.

Since only the decarburized face of the coupon was to be plated, the remaining faces of the sample were masked with Microstop to prevent any unnecessary plating. The samples were first ultrasonically cleaned to remove any contamination. Small labels were placed on the upper middle portion on the back of the samples to prevent Microstop coverage. The samples were then painted with the Microstop on all faces except the decarburized face. The Microstop was allowed to dry overnight.

After the Microstop was dry, the labels were removed to provide a site for the ensuing electrical connection. To remove any gross scratches that were imposed during the application of the Microstop, the samples were again polished to a 6μm finish. To eliminate any surface effects that may have inhibited plating (Fan et al., 1992), the samples were further polished to 0.3 alumina and then colloidal silica.

For the samples that did not undergo a decarburization step, the same grinding, polishing, and masking procedure was followed. However, the only criteria was a polished surface; the amount of material removed from the face of interest was not important.

III.B. Plating of the Samples

A schematic diagram of the plating facilities is displayed in Figure 18. One hotplate/stirrer was utilized for the cleaning step and the other one was used for the actual plating operation. Since only one load could be controlled by the power source at any given time, the sample was manually moved from the cleaning beaker to the plating beaker and the leads into the power source were switched accordingly. All the plating and cleaning operations were performed under a hood to eliminate any fume inhalation. Figure 19 displays a photograph of the plating facilities and the power source.

The insoluble anodes used for plating had a composition of 93% lead and 7% tin (Jones, 1993). To ensure even plating, the effective area of the anode was approximately 1.5 times the area of the cathode (24x44mm). Before any of the desired samples were plated, the anodes were "activated" with a dummy cathode to obtain the proper plating conditions. A short plating operation was performed with a dummy cathode to form the required anodic film (Jones, 1993) (Herczeg, 1994). This film had a dark yellow color and was an indicator that the necessary anodic condition was reached.

Immediately after the samples were polished to a colloidal silica finish, they were anodically cleaned in ElectroM&T ES solution, a commercially available powdered cleaner. The solution was placed in a stainless steel container which acted as the cathode. Following the accompanying published optimum values (Jones, 1993) for ElectroM&T ES solution operation, the samples were cleaned in a 75 g/l solution for 2 minutes with a current density of 10.8 A/dm^2 and at a temperature of 82°C. After the cleaning, the samples were rinsed with deionized water and placed in the amorphous bright chromium deposition (ABCD) solution. The ABCD plating solution was contained in a pyrex beaker and had the following composition: 100 g/l of chromic acid (CrO_3), 5 g/l of sulfuric acid (H_2SO_4), and 20 ml/l of an 85% solution of formic acid (Hoshino et al., 1986) (Tsai and Wu, 1989). To increase the current efficiency (see Figure 7), the temperature of the plating bath was maintained around 20°C with an ice bath surrounding the pyrex beaker.

To activate the cathodic surface before plating, a short "reverse etch" was employed. This "reverse etch" involved making the sample anodic and the anode cathodic for 30 seconds. The current density used for the reverse etch was 1 A/in^2 (Jones, 1993).

Immediately following the reverse etch, the electrical leads were reversed, making the sample cathodic, and the plating was initiated. The current density was set at 40 A/dm^2, following the published optimum value for the ABCD technique from Hoshino et al (1986). To maintain adequate circulation of the

plating solution during deposition, the solution was mixed using a magnetic stirrer set at a speed of 300 rpm. The duration of deposition was 30 minutes. To remove any adherent solution after plating, the sample was rinsed with deionized water and wiped clean.

III.C. Sample Exposure

III.C.1. Elevated Temperature Diffusion Studies

After plating, the samples were sectioned with a diamond saw to a size of 20x19mm, removing the unplated portion. The plated portion was then sectioned again with the diamond saw to form two halves of a plated sample with dimensions of 20x9.5mm. One of the halves was exposed and the other portion was unaffected to obtain a before-and-after effect.

To eliminate high-temperature atmospheric effects, the samples (20x9.5mm) were vacuum encapsulated. Each sample was placed in a section of cylindrical quartz tubing (inner diameter of 10.5mm, outer diameter of 12.75mm) and subjected to a series of vacuum pulls and purges with argon. The capsules were pumped down to a pressure between 40 and 55 millitorr and sealed. To ensure that the capsules were airtight, they were submerged in water. If no water entered the capsule, it was deemed hermetic.

The samples were then placed in a muffle furnace at a temperature of 700±7°C. Five different exposure times were used: 5, 10, 20, 50, and 200 hours. For each exposure, the three different decarburization depths were tested (no

decarburization, 200μm, and 400μm), for a total of fifteen encapsulated samples.

When the samples were removed from the furnace, the capsules were quenched in cool water and broken, in order to quench the plated sample itself. The samples were quenched in an attempt to "freeze in" the microstructure produced at 700°C for the exposure duration.

III.C.2. Elevated Temperature Oxidation Studies

To study the high-temperature corrosion behavior of the ABCD coatings, plated samples were placed in the furnace without being encapsulated. The unplated portion of the as-plated samples was removed by sectioning with a diamond saw. This sectioning step produced a sample plated on one face with the dimensions 15x19x3mm.

These samples were subjected to an oxygen atmosphere at 700°C for various exposure times up to a maximum of 1200 hours. Again, samples of no decarburization, 200μm decarburization depth, and 400μm decarburization were tested. Unlike in the encapsulation studies, the plated samples for the oxidation studies were allowed to air cool from 700°C to preserve the surface oxidation and to prevent any cracking of the ABCD plate from thermal stress.

The samples with no decarburization were exposed for 50, 100, 200, 400, 500, 800 and 1200 hours. The samples with the 200μm decarburization depth were exposed for 50, 100, 500, 600, 800, and 1200 hours. The 400μm samples were exposed for 50, 100, 200, 500, 600, 800, and 1200 hours. Even though all the

different samples were not exposed for the same durations, the general trends of the oxidation behavior between the different samples could be evaluated and compared.

III.C.3. Oxidation Studies of a Diffused ABCD Coating

To determine the effect of an annealing step on the oxidation behavior of the ABCD coating, as-plated samples were encapsulated and exposed at 700°C for various times. Two pieces of the same ABCD plate were placed in each encapsulation. The encapsulated exposure times were 1, 5, 22, 200, and 500 hours.

After exposure, the samples were quenched and ultrasonically cleaned in alcohol. For each encapsulation, one piece of the ABCD plate was saved to characterize the effects of the annealing step on the properties of the plate; the other piece was exposed to an oxidizing atmosphere at 700°C for 500 hours. The oxidation of the exposed section can then be compared to the as-plated 500 hour oxidation studies to determine if the diffusion stage has a pronounced effect on the oxidation resistance. These diffused samples underwent the same preparation and characterization techniques as the normal oxidation samples.

III.C.4. Erosion Studies

As a preliminary test to investigate the applicability of the ABCD coating for erosive environments, room temperature erosion tests were performed on as-

plated and annealed samples. The annealed samples were as-plated samples that were encapsulated, exposed for 1 hour at 700°C, and quenched in cool water. The erosion test was performed to determine if the annealing step improved the erosion resistance of the ABCD coating.

The samples were cut into 1/2"x1/2" squares. The angle of impingement was 90°, the erodent material was alumina, the erodent velocity was 40 m/s and, finally, the feed rate was approximately 80 grams/minute. To obtain steady-state erosion, five test times were chosen: 10, 30, 50, 80, and 100 minutes. The erosion test apparatus is described in detail elsewhere (Lindsley et al., 1993).

III.D. Metallographic Preparation

All the samples were mounted in thermosetting epoxy. To eliminate excessive rounding, the 1/4" circular mounts were prepared with stabilizers surrounding the specimen. The samples were allowed to cure for at least 8 hours. When necessary, some samples were subjected to a heat lamp at 70°C for one hour after the 8 hour cure to increase the hardness of the mounts.

The mounts were prepared using a Abrapol Automatic Grinder/Polisher. The samples were ground using 120, 240, 320, 400, 600, 800, 1200, and 3μm grit silicon carbide papers. After the 600, 800, 1200, and 3μm grit grinding steps, the samples were etched with 2% Nital to preserve the ferritic structure. The samples were also polished on the Abrapol using a 1μm diamond cloth. The mounts were then subjected to a final polish on a vibratory polisher equipped with a colloidal

silica cloth.

To observe the assorted constituents in the samples, various etchants were utilized. When necessary, the particular etchant used will be indicated in the **Results and Discussion** section.

III.D.1. Elevated Temperature Diffusion Studies

For metallographic observation, the exposed encapsulated samples were paired with their corresponding as-plated piece. The samples were positioned in the mount such that the plated sides were facing each other. The samples were then prepared using the above technique.

III.D.2. Elevated Temperature Oxidation Studies

To preserve the oxide product on the chromium plate, the oxidation samples (15x19x3mm) were first mounted in thermosetting epoxy. The samples were placed in 1/4" mounts with the plated side facing up. The mount was only filled with enough epoxy to cover the plated face.

These mounts were then sectioned into two pieces with the dimensions 15x9.5x3mm using a diamond saw. These epoxy-coated pieces were then re-mounted in epoxy with the plated sides facing each other. For extra stabilization, a thin piece of metal was placed between the epoxy-coated samples. The samples were then prepared using the aforementioned method.

III.E. Characterization and Analysis Techniques

III.E.1. As-plated Samples

After the grinding and polishing steps, the mounted samples were etched and examined with the aid of light optical microscopes. Optical micrographs of regions of interest were taken with a Riechert MeF_3 Microscope.

To determine if the ABCD technique did actually produce a chromium plate with an amorphous structure, x-ray diffraction was performed on the as-plated samples with copper K_α radiation. The accelerating voltage was 45 kV and the current was 30 mA. Previous research on the ABCD process (Hoshino et al, 1986) (Tsai and Wu, 1989) included x-ray diffraction studies. Therefore, by comparison of the diffraction patterns, the reproducibility and resultant structure of the process can be tested.

The microhardness of the as-plated samples was also performed and compared to previous work. To compare to previous studies, a Leco M-400FT Hardness Tester equipped with a Vickers indentor was used for the top surface of the coating. The load was 100 grams and the dwell time was 15 seconds.

The microhardness of the cross section of the coating was also measured. For these measurements, a Knoop indentor had to be used (ratio of long to short diagonal is 7 to 1). The load used was 10 grams and, again, the dwell time was 15 seconds. The indentations were made with the long diagonal parallel to the coating/substrate interface.

III.E.2. Elevated Temperature Diffusion Studies

Again, the samples were initially examined light optically and micrographs were taken with the Riechert MeF_3 microscope. To further reveal the alloy layers, some micrographs employed a Nomarski filter.

To characterize the diffusion behavior of the plated and encapsulated samples after exposure, light optical image analysis was coupled with electron probe microanalysis. The image analysis was performed on a Leco Image Analysis 2001 System. The image analysis provided information on the alloy layer formation and growth as a function of exposure time and initial decarburization depth. The samples were subjected to different etchants to reveal the region of interest.

The electron probe microanalysis was performed on a JEOL 733 SuperProbe equipped with WDS capabilities (including light elements). As described in detail above, the exposed samples were first mounted in epoxy. The samples were then coated with a light layer of aluminum and adequately covered with carbon tape to eliminate any charging. To maintain accurate measurements, the pure iron, chromium, and carbon standards were also covered with a light layer aluminum. The accelerating voltage was 15 KV and the probe current was 20 nA. To accurately account for light element analysis (carbon), the Bastin PROZA Phi (ρz) (EQ-91) correction scheme was implemented. Unfortunately, the JEOL was not equipped with any anti-contamination devices. Therefore, the values of carbon obtained may be affected by hydrocarbon contamination.

Microhardness tests were also performed on the encapsulated and exposed samples. The procedure used for the Knoop microhardness measurements is the same as in section **III.E.1.**. The hardness of the cross section of the alloy layers was measured.

III.E.3. Elevated Temperature Oxidation Studies

As mentioned above, the mounted oxidation samples were observed and recorded with the use of light optical microscopes and a Riechert MeF_3 microscope.

The mounted samples were analyzed using the Leco Image Analysis 2001 system. The image analysis provided information of the oxidation attack as a function of exposure time and initial decarburization depth. The samples were subjected to different etchants to reveal the areas of interest.

III.E.4. Oxidation Studies of a Diffused ABCD Coating

To characterize effects of the exposure time on the ABCD plates, Vickers microhardness tests and x-ray diffraction studies were performed on the surface of the non-oxidized pieces of the annealed ABCD plate. Five pieces were examined, corresponding to 1, 5, 22, 200, and 500 hour vacuum exposure. The procedure for the Vickers microhardness tests and x-ray diffraction studies are explained in detail in section **III.E.1.**.

For the samples oxidized for 500 hours after the initial annealing step, light

optical microscopes, a Riechert MeF_3 microscope, and Leco image analysis was used for characterization. The image analysis was employed to determine the effect of the initial annealing stage on the oxidation resistance of the ABCD coating.

III.E.5. Erosion Studies

For the erosion experiments, the behavior of the annealed and as-plated ABCD samples was characterized by the weight change. Before the erosion test, the annealed and as-plated samples were ultrasonically cleaned in acetone and weighed on a Mettler College 150 scale. After the erosion test, the samples were again ultrasonically cleaned in acetone and weighed. The weight change of the samples was then calculated. The weight change as a function of erosion exposure time was then studied to determine the effects of the pre-anneal.

IV. Results and Discussion

IV.A. Pre-plated and As-plated Samples

IV.A.1. Light Optical Analysis

After the decarburization step, some of the samples were examined metallographically to ensure that a uniform decarburization layer was achieved. Figure 20a and Figure 20b show representative microstructures after 1 hour and 2 hour decarburization times, respectively. In both cases, the decarburized depth is very uniform and consists of equiaxed grains. This result is consistent with previous research (Agarwal, 1993).

Figure 21 is a photomicrograph of the equiaxed grain structure in the decarburized region. The arrows in Figure 21 mark carbides located in the grain boundaries. The carbides formed in the grain boundaries during the rapid quenching step when the samples were decarburized. As the temperature of the iron-carbon alloy was increased to 700°C, the solubility of carbon in alpha iron increased slightly, to approximately 0.02 weight percent carbon (see Figure 12c). During the quenching step, the solubility of carbon in iron decreased significantly and at a rapid pace. Thus, the carbon was forced out of solution and formed carbides in the alpha iron grain boundaries.

Once a uniform decarburized depth was consistently produced, the samples were ground to achieve the desired final decarburization depth. The thickness of the samples was measured before, during, and after the grinding procedure to ensure that the proper amount of material was removed. The

samples were then polished with 6μm diamond, 0.3μm alumina, and finally, colloidal silica. Figure 22a and Figure 22d show typical cross-sectional views of the polished samples after the designated amount of material was removed. In Figure 22a, the final decarburization depth is 200μm and Figure 22b shows a final depth of 400μm.

After the necessary cleaning, the samples were plated using the ABCD method. Figure 23 shows the top surface of the as-plated sample. The ABCD plate is very bright and uniformly distributed across the surface. The plate is also covered with long cracks that seem to extend from the edges. These surface cracks were found on all the as-plated samples. Figure 24 shows a representative plate on top of a decarburized substrate. The plate is very uniform and appears to be defect and crack-free. Figure 25 shows another as-plated sample. This micrograph shows the chromium plate at a higher magnification and on top of a non-decarburized substrate. The thickness of the plate is approximately 20μm. Again, no cracks or defects are apparent. This type of microstructure for the chromium plate is consistent with previous research (Hoshino et al., 1989).

Upon further microscopic inspection of the chromium plate, however, macrocracks are visible. Figure 26 shows a representative macrocrack in the ABCD plate. These macrocracks typically extend through the entire coating perpendicular to the coating/substrate interface and are believed to correlate with the cracks seen on the surface of the plate (Figure 23). The cause of these macrocracks has not been determined, but they may result from the relief of stress

within the chromium plate after the plating operation (Hoflund, 1994).

Although the ABCD technique did not produce a completely crack-free chromium coating, it did greatly reduce the number of cracks that form during chromium electroplating. A typical chromium electroplate is displayed in Figure 27 (Agarwal, 1993). Numerous cracks (indicated by the arrows) are evident throughout the entire thickness of the coating. The ABCD procedure produced a chromium plate with approximately 1.4 macrocracks per millimeter. Although the number of macrocracks were not measured, the number of microcracks in a conventional plate is on the order of 100 cracks/mm.

IV.A.2. X-ray Diffraction Analysis

To determine if the chromium plate was indeed amorphous, x-ray diffraction was performed on the as-plated samples. Figure 28a shows the x-ray pattern of the as-plated sample. A diffused peak lies at approximately the position (44°) for the strongest crystalline chromium peak. The diffused nature of the peak obtained indicates that the as-plated chromium plate is not truly crystalline. This outcome is consistent with the results acquired by Hoshino (1986) for the as-plated ABCD plate (displayed in Figure 28b). The relatively sharp peak immediately before the diffused chromium peak is not a detected crystalline peak; it was caused by noise in the x-ray diffraction system.

IV.A.3. Room Temperature Microhardness

To compare with previous studies, the microhardness of the top surface of the coating was measured using a Leco M-400FT Hardness tester. Using a 100 gram load and a 15 second dwell time, the average Vickers hardness was 1033.5 HV. This value closely resembles the as-plated hardness of Hoshino et al (1986) (in Figure 11) and Tsai and Wu (1989). Both investigations produced an as-plated Vickers hardness of approximately 1000 HV.

The cross-sectional microhardness of the coating and the substrate was also measured. The substrate was not initially decarburized. To obtain accurate measurements, the Knoop indentor with a 10 gram load was utilized instead of the Vickers indentor used on the surface. A micrograph of a representative trace through the as-plated coating is shown in Figure 29a and the average Knoop hardness values across the coating are shown in Figure 29b. As expected, the chromium coating has significantly higher hardness values than the iron-carbon alloy substrate material.

IV.B. Elevated Temperature Diffusion Studies

IV.B.1. Light Optical Analysis

After exposure to 700°C for various times, all the vacuum encapsulated samples showed very little oxide formation, indicating that the vacuum imposed was sufficient enough to prevent atmospheric effects. The exposed samples had a greyish, matte appearance as opposed to the bright unexposed plated samples

and the severity of cracking appeared to increase with exposure time.

A cross-sectional micrograph of an diffused coating is shown in Figure 30a and Figure 30b. The micrograph was taken from the 200 hour exposed sample with no initial decarburization. From the micrograph, five distinct regions can be observed. All five regions are separated by relatively planar interfaces. This type of alloy layer formation was observed in each encapsulated sample for all exposure times, albeit at a lesser extent. Since the non-decarburized sample exposed for 200 hours developed the largest alloy layers, it was often used in subsequent analyses. In other words, it acted as a representative sample.

Even though the as-plated ABCD coating contained cracks, the number of cracks did not increase greatly after the elevated temperature exposure. The exposed coating comprised of approximately 1.6 cracks per millimeter, compared to 1.4 cracks per millimeter prior to exposure.

IV.B.2. X-ray Diffraction Analysis

To determine the behavior of the structure of the ABCD plate after exposure at 700°C for various times, x-ray diffraction was performed on the annealed samples. However, the conditions of the annealed plates was not conducive for accurate x-ray analysis. For example, due to the thicknesses of the ABCD plates (approximately 20 microns), the annealed samples were not ground or polished to obtain a flat surface. Also, even though a majority of the oxidation was inhibited by the encapsulation procedure, some oxide scale did form. These

scales, along with the surface finish of the samples, could shift or alter the diffraction peaks associated with the components present. However, although no definitive x-ray analysis could be performed on the annealed plates, the changes observed in the overall diffraction pattern offer information as to how the structure of the plate reacts to elevated temperature exposure after different annealing times.

The encapsulated samples were exposed for 1, 5, 22, and 200 hours. The diffraction patterns with their "plausible" peak labels are displayed in Figures 31a, 31b, 31c, and 31d. As seen in Figure 31a, even after only 1 hour of exposure at 700°C, the original diffused chromium peak seen in the as-plated sample (Figure 29) has transformed into a distinct chromium peak (at 44°). Other, minor chromium peaks have also formed, confirming the existence of crystalline chromium.

Along with the development of the crystalline chromium peaks, the diffraction pattern indicates the presence of chromium carbides and chromium oxides. The pattern seems to strongly indicate the presence of Cr_7C_3. This result is consistent with the diffraction patterns of Hoshino (1986) and Tsai and Wu (1989) after one hour exposure at 700°C. The presence of various chromium oxides confirms that some minor oxidation of the encapsulated samples occurred during exposure.

When the exposure time is increased to 5 hours (Figure 31b), no new peaks have formed; the pattern indicates the existence pure chromium, Cr_7C_3, and

several chromium oxides. However, the intensity of the Cr_7C_3 peaks has increased, indicating the growth of the chromium carbides in the ABCD coating.

As the exposure time is increased to 22 hours, a continued increase in the peak intensity of the chromium and Cr_7C_3 phases is observed. (The vertical scale of Figure 31c is larger than the previous patterns.) Again, the x-ray diffraction pattern distinctly signifies the presence of crystalline chromium, Cr_7C_3, and assorted chromium oxides.

When the exposure time is increased to 200 hours (Figure 31d), however, a distinct change in the diffraction pattern occurs. The crystalline chromium and chromium oxide peaks still exist, but now the previously numerous Cr_7C_3 peaks are no longer explicit. Some peaks exist which may indicate the presence of Cr_7C_3, but due to the oxide scale and errors involved in the analysis, no definitive identification can be made. A new type of chromium carbide, $Cr_{23}C_6$, dominates the diffraction pattern. Due to the large difference in exposure time between the 22 hour and 200 hour exposure samples, the exact exposure time at which the $Cr_{23}C_6$ phase materializes could not be ascertained.

Tsai and Wu (1989) determined that as the temperature is increased, different phases precipitate out of the amorphous chromium matrix. They exposed the ABCD plate to various temperatures for one hour. At 300°C, the crystalline chromium starts to precipitate out of the amorphous matrix. The Cr_7C_3 phase begins to precipitate when the temperature is increased to 480°C. The chromium and Cr_7C_3 phases continue to coarsen as the temperature is increased

to 700°C. At approximately 710°C, the $Cr_{23}C_6$ phase begins to emerge out of the Cr_7C_3 phase after one hour of exposure. The data from the present research indicates that the appearance of the $Cr_{23}C_6$ phase can occur at lower temperatures (700°C), albeit after much longer exposure.

IV.B.3. Room Temperature Microhardness

The room temperature microhardness was measured on the top surface of five plates after they had been exposed for 1, 5, 22, 200, and 500 hours respectively. The Vickers hardness values are plotted as a function of exposure time in Figure 32. Included in the figure is the Vickers hardness measured by Hoshino (1986) after exposure of one hour at 700°C.

Inspection of Figure 32 reveals that when the ABCD plate is exposed for one hour, the hardness increases dramatically. This elevation in hardness can be accredited to the crystallization of the amorphous chromium and the precipitation of Cr_7C_3 from the amorphous matrix. However, as the exposure time is increased, the hardness of the coating decreases. Hoshino (1986) and Tsai and Wu (1989) demonstrated that the hardness of the ABCD plates reaches a maximum after one hour exposure at 500°C and then begins to diminish as the exposure temperature is increased. Tsai and Wu (1989) attributed this decrease in hardness to increasing chromium dispersoid and chromium carbide size. Also, as the temperature is increased further, Cr_7C_3 is replaced by $Cr_{23}C_6$, a softer carbide. (Cr_7C_3 typically has a hardness of 2100 DPH compared to 1650 DPH for $Cr_{23}C_6$.).

Thus, the decrease in hardness with extended exposure time at 700°C can also be explained by continued growth of the chromium dispersoids and precipitation of the $Cr_{23}C_6$ phase. The longer the exposure time, the greater the coarsening of the crystalline chromium dispersoids and precipitation of the $Cr_{23}C_6$ phase and, as a result, the lower the hardness value.

Using a Knoop indentor and a 10 gram load, the cross-sectional microhardness of the diffused samples was also determined. A micrograph of a representative trace through the alloy layers is shown in Figure 33a. The change in the size of the Knoop indentations across the alloy layers is indicative of the changing hardness of the alloy layers. Clearly Layer #1 and #2 have substantially higher hardness values than the other alloy layers. Several traces were performed and the average Knoop hardness values are shown in Figure 33b.

In subsequent sections, the alloy layers are identified using microprobe analysis and the 700°C slice of the iron-chromium-carbon ternary phase diagram. Knowing the composition of the alloy layers, the change in hardness across the alloy layers can be justified (Figure 33). The alloy layers initial observed are in fact carbide layers of different compositions. The presence of these continuous layers causes the hardness to increase between the initial ABCD plate and the iron-carbon substrate. From Figure 33, alloy layer #2 exhibited the highest hardness values. This layer turned out to be a two-phase M_7C_3 + M_3C region; essentially a precipitation hardened material.

IV.B.4. Light Optical Image Analysis

To determine the diffusional behavior with exposure time, the diffused samples were analyzed using a Leco 2001 Image Analysis System. The Leco system was used to measure the thicknesses of the various microscopic diffusion layers. A schematic diagram of the alloy layers and their respective designations is shown in Figure 34.

Each individual alloy layer thickness and the total alloy layer thickness was measured as a function of exposure time. The results are given in Figures 35a, 35b, 35c, and 35d. In each case, the growth of the alloy layer changes with exposure time in a parabolic nature. This type of behavior indicates diffusion controlled growth.

Since the growth is diffusion controlled, the thicknesses of the alloy layers versus the square root of exposure time could be plotted to produce a straight line. The squared slope of this straight line could then be calculated to extract a rudimentary interdiffusion coefficient for that particular alloy layer. The graphs for the alloy layers are shown in Figures 36a, 36b, 36c, and 36d.

By using linear regression analysis, the slope of the lines were calculated. These slopes act as a parabolic growth rate constant, or k_p value, for the different alloy layers that formed. The k_p value has units of $\mu m/h^{1/2}$ and is a direct indication on the velocity of alloy layer growth; the higher the k_p value, the faster the alloy layer grows. The calculated parabolic growth rates for the individual alloy layers for the three initial decarburization depths are shown in Table 6 at

the end of this report. Also, the k_p value for the growth of all three alloy layers combined is given.

From the k_p values shown in Table 6, several observations on the effect of initial decarburization on the subsequent growth of alloy layers can be made. First, considering the errors involved in such a small measurement (the layer thickness is on the order of 1 micron), the k_p values for alloy layer #1 do not change dramatically with increasing initial decarburization. Thus, the formation of alloy layer #1 seems to be independent of initial decarburization.

For the second layer, however, a relatively significant decrease in k_p values is seen as the initial decarburization depth increases from 200μm to 400μm. The two parabolic constant values for the zero and 200μm initial decarburization layer appear to be numerically close. However, when the initial decarburization depth is increased to 400μm, the formation of layer #2 appears to be inhibited.

For alloy layer #3, again within probable error, the k_p values for all three initial decarburizations seem to be reasonably close. Therefore, as seen in alloy layer #1, the initial decarburization depth do not appear to affect the growth of alloy layer #3.

Finally, for the combination of all three alloy layers (total layer), the k_p values for the zero and 200μm decarburizations are very similar. However, for the 400μm initial decarburization, the k_p value again decreases. Since layers #1 and #3 have relatively comparable parabolic rate constants for all depths of decarburization, the k_p value for layer #2 can be the reason for the decrease in

total layer parabolic constant for the 400μm initial decarburization.

Agarwal (1993) also calculated the parabolic rate constant for the total alloy layer growth. In his study, a conventional pure chromium plate was placed on a iron-carbon alloy substrate initially decarburized to a depth of 475μm. After exposure at 600°C for various extended times, his calculated k_p value was 0.07 $\mu m/h^{1/2}$, substantially less than the parabolic rate constants obtain from the present study. The considerable deviation between k_p values can be justified by differences in the research conditions. For example, the difference in the composition of the chromium plate plays a major role in the layer formation. In the present study, carbon existed in both the coating and the substrate, acting as two separate sources. With these two isolated sources, the diffusion of carbon is facilitated and, thus, the growth of the alloy layers is augmented. Also, the larger initial decarburization depth and lower exposure temperature of 600°C hindered the layer formation observed by Agarwal (1993).

Comparing the parabolic rate constants between the individual alloy layers, layer #3 grows considerably faster than either layer #1 or #2. As shown in subsequent sections, all three alloy layers are carbide layers. Even though the ABCD coating contains a considerable amount of carbon, upon exposure to elevated temperature, most of the carbon in the ABCD coating becomes tied up as chromium carbides (Tsai and Wu, 1989). Some carbon can move from the ABCD plate into the alloy layers, but it seems likely that only layer #1 would benefit from this carbon source. Thus, a majority of the carbon used for the

formation of the carbide layers (layer #2 and layer #3) is being supplied from the iron-carbon substrate. Layer #3 acts as a diffusion barrier and impedes the growth of alloy layers #1 and #2 by slowing down the flow of carbon from the substrate. Therefore, the accelerated growth of layer #3 with respect to layers #1 and #2 is justified.

For the sake of comparison to previous studies, the parabolic rate constant for the total alloy layer with no initial decarburization displayed above can be converted to interdiffusion coefficients. From the general diffusion equation,

$$x^2 = 4ADt$$

the value of **4AD** can be determined from the slope of the graph x^2 versus t, which is also equal to k_p. Thus,

$$k_p = 4AD$$

Since the value of **A** is close to unity (Menzies and Mortimer, 1966), it will be disregarded. Therefore, to convert the calculated parabolic rate constants to interdiffusion coefficients, the k_p initially calculated values must be squared, divided by four, and converted from $\mu m^2/hr$ to cm^2/sec. The results are shown in Table 7 at the end of this report. The table includes interdiffusion coefficient of previous investigations with their respective substrate carbon content and the temperature of the diffusion study.

The value of the interdiffusion coefficient from the present work varies by as much as three orders of magnitude when compared to the previous research.

However, when one takes into account the significant differences between the analyses, the interdiffusion coefficient calculated from the present work appears reasonable. For example, the present work involves the diffusion of a chromium electroplate containing approximately 3% carbon into a iron-carbon (0.2 wt% carbon) substrate. The previous investigations studied the diffusion behavior of pure chromium into various steel substrates with varying carbon contents. Also, the previous studies were all performed above at higher temperatures, above the A_1, when the interdiffusion of chromium, iron, and carbon should be substantially enhanced. Above the A_1 temperature, the interdiffusion is amplified by the increase in temperature and the phase change of iron from a BCC crystal structure to a FCC crystal structure. Even though the FCC crystal is more closely packed than the BCC crystal, interstitial diffusion of carbon occurs more readily in the FCC crystal structure.

IV.B.5. Electron Probe Microanalysis and Ternary Diffusion

To determine the composition of the various diffused alloy layers, electron probe microanalysis (WDS) was employed. The probe was stepped at 1μm intervals across the various layers. The information obtained from the WDS analysis was then put through the Bastin PROZA Phi (ρz) (EQ-91) correction scheme. The Bastin PROZA correction scheme was chosen because it is specially designed for light element analysis. The compositional trace across the layers according to the Bastin PROZA correction is shown in Figure 37. Also included

in the figure is a micrograph of the alloy layers displaying the probe trace. Figure 38 shows the WDS map that was acquired from the probed region of the sample. The actual compositional values for the three elements is displayed in Table 6. Only one point was not within the standard 2% acceptable error, indicating a rather accurate elemental analysis.

From the probe trace, the carbon content in the coating was found to be approximately 3.0 weight percent. This value correlates well with previous chemical analysis of the ABCD plate (see Figure 8). The carbon content stays relatively constant through the ABCD coating. As expected, the chromium content is very high and the iron content is very low in the ABCD plate.

When the trace enters alloy layer #1, the carbon content abruptly jumps to approximately 9.25 weight percent. The chromium content drops to 80% at the end of alloy layer #1. Conversely, the iron content begins to rise in alloy layer #1 to a maximum value of approximately 10%.

In alloy layer #2, the carbon content decreases only slightly -- to about 8.25%. The chromium content drops to 35% and the iron content continues to increase to a value of 55% near the end of the second alloy layer.

The carbon content changes more drastically as the probe enters alloy layer #3; it falls to a value of roughly 6.25%. It remains relatively constant throughout the entire layer. Alloy layer #3 also brings dramatic changes in the chromium and iron content. At the ABCD coating side of layer #3, the chromium and iron content is approximately 12% and 81%, respectively. However, by the end of

layer #3, the chromium content falls below 2% and the iron content climbs above 97%.

When the probe exists layer #3 and enters the decarburized substrate, the carbon content decreases to a value below 2% and the chromium content is below 1% and can be considered to be a trace amount. The substrate is basically all iron. Further into the substrate, the carbon content dips below 1%. This relatively high content of carbon in a decarburized region could be attributed to the inherent carbon contamination acquired during the probe analysis. From the iron-carbon phase diagram (Figure 12), the carbon content in the decarburized region should be no more than 0.02%. As mentioned in the **Experimental Procedure**, the JEOL 733 probe used in this microanalysis was not equipped with any anti-contamination devices. The absence of such an apparatus allows for the buildup of hydrocarbons. Thus, there is contamination error associated with each point. Also, as the analysis progressed, hydrocarbon contamination could have accumulated -- thereby degrading the accuracy as the probe trace proceeded. Since the carbon value detected is approximately 1% in this decarburized region, the error associated with the carbon content should not be greater than 1% throughout the analysis.

Using the composition values from the probe trace, a diffusion path through the ternary iron-chromium-carbon diagram can be proposed and information as to what phases exist can be extracted. The 700°C isotherm of the ternary diagram is displayed in Figure 39 (from Rivlin, 1984). At temperatures

above 440°C, a solid solution of αFeCr can form at the expense of the σ phase because of the very small differences in the Gibbs free energy (Rivlin, 1984). Since the existence of the sigma phase is still under debate, it has been omitted. Also, two regions are taken from the 1000°C ternary isotherm. These regions are shown as dotted lines on the 700°C slice because the exact position of these points has not been determined (Rivlin, 1984). Also, since no tie lines were found in the literature for the ternary slice, no tie lines are included. The actual measured compositional values are plotted as open circles and the proposed ternary diffusion path (dark line) is shown in Figure 39, following the ternary rules of Clark (1963). The lines drawn in the two phase and three phase regions should travel along tie lines, unless otherwise indicated.

To accurately determine the nature of the diffused alloy layers, several electron micrographs were acquired. Figure 40 shows a SEM micrograph of the diffusion zone of a non-decarburized sample exposure for 200 hours at 700°C and etched with Murakami's agent. From this secondary electron image, five distinct regions can be discerned. To gain more atomic information, a backscattered image of the diffusion zone in the same sample was also obtained (Figure 41). This time, however, the sample was polished and not etched. Therefore, the only contrast visible is caused by the differences in atomic number between the alloy layers. Again, five well-defined regions can be distinguished.

The starting composition in the ABCD coating indicates the existence of a two-phase region, namely $\alpha Cr + M_{23}C_6$. A backscattered SEM micrograph of the

exposed ABCD coating is shown in Figure 42. From the figure, two distinct phases can be discerned, confirming the compositional analysis. Since carbides have lower average atomic weight than pure chromium, they appear as white dots in the black matrix. In previous chromizing studies (Kaluba and Foct, 1987), the $M_{23}C_6$ phase typically formed in areas rich in chromium.

When x-ray analysis of the surface of the ABCD plate after 200 hours of exposure was performed, some peaks appeared to indicate the presence of either the Cr_7C_3 phase or various chromium oxides. The microanalysis performed here, however, securely placed the composition of the exposed plate in the two phase $\alpha Cr + M_{23}C_6$ region on the equilibrium ternary phase diagram. If the peaks from the x-ray diffraction analysis are actually Cr_7C_3 peaks, a discrepancy between the two analyses is encountered. These conflicting results on the same sample can be taken as an indication that 200 hours of exposure at 700°C was not sufficient for the system to reach equilibrium. If the sample had not reached equilibrium, no path could be established on the 700° slice of the equilibrium ternary phase diagram.

To determine if equilibrium was in fact reached, microanalysis was performed within the ABCD plate on a sample exposed for 500 hours. Again, the composition indicated that the ABCD plate consisted of two phases, $\alpha Cr + M_{23}C_6$. The values from the trace on the 500 hour sample are imposed on the ternary diagram (closed circles on Figure 39). Taking into consideration the errors associated with the x-ray diffraction analysis mentioned above, the results

obtained with the "more reliable" probe traces confirm the existence of the two-phase region consisting of $\alpha Cr + M_{23}C_6$, without any Cr_7C_3. Thus, after 200 hours of exposure, the system has reached equilibrium, and a diffusion path can be proposed on the ternary phase diagram.

For the ternary analysis, the annealed plate is treated as a diffusion couple with the ABCD coating on one side and the non-decarburized iron-carbon alloy on the other. To start the journey across the ternary phase diagram, a straight dash-dot line is first drawn from the starting and finishing concentrations of the diffusion couple. Following these plotted points, the composition travels (dark line) across the two phase $\alpha Cr + M_{23}C_6$ region to the single phase $M_{23}C_6$ region as the ABCD coating is traversed. It is assumed that the data follows tie lines even though no tie lines were found in the literature. Although the diffusion path appears to head directly for the $M_{23}C_6$ region, no single phase $M_{23}C_6$ compositional values were measured between the coating and the first alloy layer.

Moving from the ABCD plate into alloy layer #1, the compositional values (open circles) on the ternary isotherm appear to signify the existence of a single phase M_7C_3 region adjacent to the ABCD plate. The formation of the M_7C_3 phase is common during the chromizing process (Kaluba and Foct, 1987) (Zancheva et al., 1978) (Glowacki and Kaluba, 1982). To get from the two phase $\alpha Cr + M_{23}C_6$ region to the M_7C_3 region without passing through the single phase $M_{23}C_6$ region, the diffusion path must travel through the three phase $\alpha Cr + M_{23}C_6 + M_7C_3$ zone. Because this region has no spatial extent in the diffusion couple, the path through

the three phase region is presented as a straight, dotted line (Clark, 1963).

Following the plotted composition points, the diffusion path does not seem to extend to the existing triple point on the ternary phase diagram (marked **TP** on Figure 39). If, in fact, the present data is accurate, the position of the triple point would be moved to a higher chromium concentration. A ternary slice with the new proposed position of the triple point is shown in Figure 43. The position of the "old" triple point is indicated by dotted lines. Figure 43 also contains the proposed diffusion path and actual measured compositional points from the 200 hour (open circles) and 500 hour (closed circles) samples.

After passing through the three phase $\alpha Cr + M_{23}C_6 + M_7C_3$ zone, the compositional values lead to the existence of a single phase M_7C_3 region. Even though the compositional values do not lie exactly on the M_7C_3 line compound, observation of the binary diagram (ASM, 1990) between carbon and chromium indicates that carbide line compounds actually have some limited solubility. Coupled with the inherent error of measuring the carbon content, the slight deviation from the composition of the line compound is justified. The backscattered images of Figure 41 and 42 confirm the existence of the single phase region. Following the compositional points plotted on the ternary slice, the diffusion path travels down the M_7C_3 line compound.

An SEM micrograph of layer #1 and layer #2 is shown in Figure 44. Layer #2 appears to precipitate out of a matrix of M_7C_3. From the ternary slice and the compositional analysis, the precipitates seem to be M_3C carbides. Thus, layer #2

is actually a two-phase region with M_3C precipitates in a M_7C_3 matrix. The backscattered images of Figure 41 and 42 support the presence of a two-phase region. Whereas the development of separate layers of M_7C_3 and M_3C has been documented in chromizing studies (Kaluba and Foct, 1987), the formation of a two-phase M_7C_3 + M_3C region has not been previously observed. Figure 44 also shows needle-like grain boundaries near the bottom of the single phase M_7C_3 region. This morphology is typical of the M_7C_3 region (Kaluba and Foct, 1987) (Zancheva et al., 1978).

Moving from the single phase M_7C_3 region to the two phase M_7C_3 + M_3C zone, the diffusion path travels down the M_7C_3 phase and traces a "loop" into the M_7C_3 + M_3C region, beginning and ending on the dotted single phase M_7C_3 line compound. This "loop" crosses the tie lines in the two phase region and signifies precipitation of the M_3C phase in a matrix of M_7C_3. The diffusion path then travels as a solid, straight line along tie lines through the two phase M_7C_3 + M_3C region to the next phase, M_3C.

Another SEM micrograph is shown in Figure 45. This micrograph shows layer #3 as it touches the two phase M_7C_3 + M_3C (layer #2) region. Again following the ternary diagram and observing the aforementioned backscattered images, this region seems to be a single phase M_3C region. Again, from previous chromizing studies, the formation of a M_3C layer typically occurs between the M_7C_3 phase and the steel substrate (Kaluba and Foct, 1987) (Zancheva et al., 1978) (Kaluba and Wachowiak, 1983). The direction of the columnar grain structure

(into the two phase M_7C_3 + M_3C zone) in this layer is an indication that diffusion is occurring from the iron-carbon substrate into the alloy layers.

Given the extensive errors associated with carbon microanalysis and the limited solubility of the carbide compound, the compositional values associated lie approximately along the M_3C compound line. As this layer is traversed, the iron content increases and the diffusion path travels directly down the M_3C phase.

Adjacent to the single phase M_3C region is a decarburized zone of iron-carbon alloy substrate. The compositional analysis indicated a large amount of carbon in the decarburized region. However, due to the inherent hydrocarbon contamination problems associated with the microprobe analysis, these values are not considered to be valid.

Moving into the substrate, the measured compositional values signify the presence of a single phase αFe region. The compositional values also cause the diffusion path to travel close to the initial composition in the iron-carbon alloy. Adhering to the ternary rules set by Clark (1963), the diffusion path crosses the straight line drawn from the initial to final composition. Since the decarburized region is much larger than the alloy layers, the conservation of mass on both sides of the straight line is also followed (Metselaar, 1988).

From the x-ray diffraction analysis, electron probe microanalysis, and the 700°C slice of the ternary phase diagram, a comprehensive study on the composition of ABCD plate and the resulting alloy layers after elevated temperature exposure for 200 hours was performed. As a summary, Table 9

identifies equilibrium phases present and the range of compositions of chromium, iron, and carbon in these layers.

The starting "diffusion couple" consisted of an amorphous chromium plate containing approximately 3 weight percent chromium on top of a non-decarburized iron-carbon alloy. After 200 hours of exposure at 700°C, the amorphous plate crystallized and produced chromium carbides, three distinct alloy layers formed between the two initial constituents, and significant decarburization of the iron-carbon alloy occurred. Combining x-ray and probe analyses, the exposed ABCD plate consisted of two distinct phases, namely αCr and $M_{23}C_6$. The alloy layer (layer #1) directly below the ABCD plate became a single phase region of M_7C_3. The layer adjacent to the M_7C_3 phase (layer #2) became a two-phase M_7C_3 + M_3C region, with discrete M_3C precipitates forming in a M_7C_3 matrix. The last alloy layer (layer #3) formed to be another single phase region, M_3C. Finally, the decarburized substrate was found to be a single phase αFe region.

IV.C. Elevated Temperature Oxidation Studies

IV.C.1. Light Optical Analysis

Figure 46 shows the typical appearance of the plated samples after exposure. Even though long cracks are visible in the plate before exposure (Figure 23), the cracking appears more severe after exposure. The extent of cracking and the width of the cracks appears to increase with increasing exposure.

The green color that covers the exposed plate indicates that chromium oxide has formed from the high temperature exposure. The cracks, however, appear black -- signifying that a different type of oxide has formed through the crack network.

Figures 47a and 47b display representative microstructures of the exposed plates. The oxide first attacks down a pre-existing crack and then travels along the coating/substrate interface. The oxide also "mushrooms" up through the original crack. Due to the exposure of the iron-carbon alloy substrate, this oxide is probably a type of iron oxide. The different shades in the oxide "mushroom" seems to indicate that different varieties of iron oxides are being formed.

IV.C.2. Lateral Percentage of Oxide Attack at the Coating/Substrate Interface

Using Leco Image Analysis, the lateral percentage of oxide attack versus exposure time was determined for all three decarburization depths (0μm, 200μm, and 400μm). The lateral percentage was calculated by measuring the planar length of oxide attack observed at the interface over the entire length of sample observed. The results are given graphically in Figure 48.

At first, as the exposure time is increased, the lateral oxide attack at the interface resembles parabolic growth. This parabolic nature continues for all initial decarburization depths until 500 hours. After this exposure, the lateral percentage of oxide attack for all the samples jumps over 20%, indicating "break-away" corrosion. This type of corrosive attack is common in unprotected metals.

From 800 to 1200 hours, the oxide attack at the interface does not increase

for any sample; the percentage of oxide attack appears to level-off at 26%, again resembling parabolic corrosive attack. Therefore, the depth of initial decarburization does not seem to influence the long-term oxidation resistance.

IV.C.3. Maximum Oxide Penetration into the Substrate Material

Along with attacking along the interface, the oxide also penetrated into the substrate. Again using Leco Image Analysis, the maximum depth of oxide attack into the interface was determined. The maximum depth was defined to be the perpendicular distance from the coating/substrate interface to the bottom of the oxide intrusion. The results are displayed graphically in Figure 49.

As shown in Figure 49, the depth of the initial decarburization does not seem to affect the maximum oxide penetration up to 600 hours. However, past 600 hours, the maximum penetration of oxide intrusion is increased as the initial decarburization is increased from zero to 400μm. As shown in previous sections, as the initial decarburization is increased, the rate of alloy formation decreases. Since carbide layers have excellent corrosion resistance (Kaluba and Wachowiak, 1983), the samples that form these carbide layers the quickest should exhibit improved oxidation resistance. This speculation is confirmed by the superior performance against oxide penetration of the non-decarburized samples.

For all the samples, the maximum depth of oxide penetration increases dramatically from 800 to 1200 hours. Thus, although the oxide attack at the interface appears to "arrest" after 800 hours, the oxide attack into the substrate

material shows no signs of abating. This dramatic increase in oxidation attack resembles "break-away corrosion", a type of corrosion commonly found in unprotected steel components.

IV.C.4. Oxidation Studies of Diffused ABCD Coating

Since carbide layers have good corrosion resistance (Kaluba and Wachowiak, 1983), sufficient formation of such a layer before substantial oxide attack could increase the corrosion resistance. Therefore, the samples that form the carbide layer the quickest should show an increased resistance to oxide attack. With this in mind, ABCD plates on non-decarburized substrates were first encapsulated and then exposed to 700°C for various times, namely 1, 5, 22, 200, and 500 hours. These samples were then exposed to an oxidizing atmosphere, again at 700°C, for 500 hours. By observing the oxidation attack, the effectiveness of forming an alloy layer can be determined.

Figure 50 displays the lateral percentage of oxide attack as a function of pre-anneal exposure time. To increase the visibility of the short time data points, the graph is displayed with a log scale along the x-axis. Inspection of Figure 50 reveals that, within measuremental error, there is little change in the oxide attack as the annealing time at 700°C is extended to 5 hours. However, when the exposure time reaches 22 hours, a significant decrease in the attack is observed. This decrease can be accredited to the formation of carbide layers below the ABCD coating. Therefore, even though the ABCD initially contains macrocracks,

the formation of the alloy layers prevent accelerated oxide penetration down these cracks when the plate is exposed to elevated temperature oxidation. Figure 51 shows a pre-existing macrocrack in the ABCD coating in the 22 hour anneal sample after 500 hours of elevated-temperature oxidation exposure. No extensive oxidation attack is visible. Unfortunately, not all the cracks have experienced the same carbide layer protection. Figure 52 displays dramatic oxide attack down a pre-existing crack in the ABCD plate. Thus, although some cracks do not permit any attack, other cracks are not as supported by the underlying carbide layers.

When the pre-annealing step is increased to 200 hours, the oxide attack at the interface exhibits a different appearance. Due to the extended time of the pre-anneal, the carbide layers have grown substantially and no visible attack is observed down any of the pre-existing cracks. Thus, instead of travelling down pre-existing cracks in the ABCD plate and forming a continuous layer, the oxide attack occurs in discrete areas along the coating/substrate interface. Figure 53 exhibits how the oxide creates spherical cavities along the interface, resembling internal oxidation attack (Stott and Wood, 1988).

The formation of these cavities at the coating/substrate interface may be caused by the diffusion of oxygen through the ABCD plate. Since the carbide layers have inhibited oxide attack down the macrocracks in the ABCD coating, oxygen no longer has a fast diffusion path to the coating/substrate interface. Instead, oxygen must now diffuse through the bulk coating to reach the substrate material. Tsai and Wu (1990) exhibited how the Cr_7C_3 phase is replaced by the

$Cr_{23}C_6$ phase as the temperature is increased. This same behavior was shown above in the x-ray diffraction analysis as the exposure time was increased. Thus, as the pre-anneal time is increased, the Cr_7C_3 phase is replaced by the $Cr_{23}C_6$ phase, and, as a consequence, more chromium is tied up in carbides. Unlike the alloy layers below the ABCD coating, the carbides formed in the plate do not form a continuous layer (Figure 42). The formation of these carbides may produce boundaries which can act as fast diffusion paths for the transport of oxygen. However, due to the elevated temperature of exposure (700°C), both grain boundary and lattice diffusion may play a significant role in the movement of oxygen from the surface to the coating/substrate interface.

Although the oxide attack caused by the diffusion of oxygen through the coating appears to be less severe than the attack down the pre-existing cracks, the planar percentage of attack is actually greater as the pre-anneal is increased past 22 hours (Figure 50). When the attack is down macrocracks, the penetration along the interface is very severe near the macrocrack, but other areas of the interface are untouched. On the other hand, when the attack is caused by the diffusion of oxygen through the coating, the discrete penetrations extend along the entire coating/substrate interface, thereby increasing the percentage of oxide attack.

When the pre-anneal time is increased to 500 hours, the percentage of oxide attack continues to rise, indicating a more efficient transport of oxygen through the ABCD plate. Again, the morphology of the attack is small spherical cavities. The exact mechanism of this transport is not understood at this time.

IV.D. Erosion Tests

The weight loss of the as-plated and annealed ABCD samples as a function of exposure time is shown in Figure 54. To compare the erosion behavior of the as-plated and annealed plates, the data points can be fit with a straight line and the slope of this straight line yields the steady-state erosion rate. The steady-state erosion rate is an indication of the extended erosion behavior of a material. For the as-plated ABCD samples the erosion rate is 0.105 mg/min. However, for the annealed ABCD samples, the steady state erosion rate is 0.058 mg/min, considerably less than for the as-plated samples.

The significant increase in erosion resistance of the annealed ABCD plate can be attributed to the crystallization of the chromium dispersoids and precipitation of chromium carbides. As previously exhibited, when the ABCD plate is annealed for one hour at 700°C, chromium crystallizes and the Cr_7C_3 phase precipitates out of the amorphous matrix. As a consequence, the hardness increases (from 1033 to 1221 HV), principally from the precipitation of the carbide phase. In effect, the annealed ABCD plate becomes a dispersion-hardened alloy -- hard carbides in a relatively "soft" chromium matrix. Together, the hard chromium carbides and the "soft" chromium matrix may provide the optimal combination of mechanical properties for better erosion resistance compared to the as-plated, amorphous plate.

V. Conclusions

By exposing amorphous bright chromium deposits (ABCD) to 700°C for various times under neutral and oxidizing atmospheres, the diffusion and corrosion behavior of the electroplates was characterized. From the analyses, the following conclusions can be drawn:

1.) The ABCD technique utilized in the present study produced a uniform, bright amorphous chromium plate. Although macrocracks formed throughout the plate, the number of cracks in the ABCD plate is greatly reduced to approximately 1.4 cracks/mm compared to the conventional chromium plate which is on the order of 100 cracks/mm.

2.) From the x-ray diffraction studies, when the ABCD plate is vacuum encapsulated and annealed at 700°C for one hour, chromium crystals and Cr_7C_3 precipitate out of the amorphous chromium matrix. These constituents continue to grow as the exposure time is increased to 22 hours. However, after 200 hours of exposure at 700°C, the $Cr_{23}C_6$ phase completely replaces the Cr_7C_3 phase. The observed transformation and growth of the precipitating phases has a marked effect on the surface hardness. Initially, the precipitation of the chromium crystals and Cr_7C_3 phase causes a increase in the hardness. However, as the elevated temperature exposure time is increased, the chromium dispersoids and the Cr_7C_3 phase coarsen, causing a decrease in the hardness. With extended exposure, the Cr_7C_3 phase is replaced by a softer carbide, $Cr_{23}C_6$, resulting in a further reduction in hardness.

3.) The vacuum encapsulation studies also allowed for the study of the diffusion behavior of the ABCD plate. The effect of the initial decarburization depth on the growth of the alloy layers was studied. Since the growth of the layers was diffusion controlled, the parabolic rate constants (k_p values) of the layer growth could be calculated and compared. Within experimental error, the growth of alloy layer #1 (M_7C_3) and alloy layer #3 (M_3C) appeared to be independent of initial decarburization depth. However, for alloy layer #2 (M_7C_3 + M_3C), the growth was decreased when the initial decarburization depth was 400μm; no significant deviation in layer growth was observed between the non-decarburized and 200μm samples. Due to the aberration of the growth of alloy layer #2, the 400μm samples exhibited a slower total alloy layer growth compared to the other decarburization depths.

4.) With the electron microprobe and light optical analysis, a path through the ternary Fe-Cr-C phase diagram at 700°C is proposed. After 200 hours of exposure, the ABCD coating consists of a two phase αCr + $M_{23}C_6$ region. The adjacent alloy layer (layer #1) appears to be a single phase region of M_7C_3 carbides. The next alloy layer (layer #2) consists of two phases, namely M_3C precipitates in a M_7C_3 matrix. Alloy layer #3 appears to be a region of single phase M_3C carbides. Finally, the substrate is comprised of a decarburized iron-carbon alloy, thereby making it single phase αFe region.

5.) Using the probe trace and various micrographs, a diffusion path across the ternary isotherm can be proposed. The ternary diagram was modified to include

a shift in the triple point to a higher chromium value and a two phase region of M_7C_3 +M_3C similar to the 1000°C ternary isotherm.

6.) The elevated temperature oxidation behavior of the ABCD plate was also studied. The initial decarburization appeared to have no effect on the extended exposure resistance; after 1200 hours at 700°C, approximately 25% of the coating/substrate interface was attacked for all initial decarburizations. The maximum depth of oxide penetration, on the other hand, seems to be dependent on the initial decarburization depth. The smaller the initial decarburization depth, the less the oxide penetration. The increased oxidation resistance can be attributed to the growth of corrosion resistant alloy layers. Since the non-decarburized samples had the fastest alloy layer growth, they experienced the increased corrosion resistance.

7.) A pre-anneal was incorporated on non-decarburized substrates to form the alloy layers prior to the oxidation exposure of the ABCD plates. A significant decrease in the planar oxide attack at the interface was encountered when the pre-anneal was extended to 22 hours. Most of the macrocracks were "protected" by the carbide alloy layers and did not act as fast diffusion paths for oxygen to the coating/substrate interface. However, when the pre-anneal time was extended to 200 hours, the oxide attack increased. This increase was observed even though none of the pre-existing macrocracks facilitated oxide attack; the morphology of the attack changed from lateral oxide attack to discrete oxide particle formation at the coating/substrate interface. The bulk diffusion of oxygen through the

exposed ABCD plate is speculated to be the cause of the augmented attack.

8.) As a preliminary test, the room temperature erosion behavior of as-plated and annealed ABCD plates was examined. After a one hour anneal at 700°C, the steady state erosion rate decreased dramatically compared to the as-plated condition, from 0.105 to 0.058 mg/min. This increase in erosion resistance can be attributed to the precipitation a hard Cr_7C_3 phase in a relatively soft chromium matrix, effectively making the annealed ABCD plate a dispersion-hardened alloy.

VI. Future Work

The present work studied the formation and growth of carbide alloy layers between an ABCD coating and an iron-carbon alloy substrates after elevated temperature exposure (700°C) as a function of time. In particular, the effect of three different decarburization depths on the alloy layer growth was investigated. The composition of these alloy layers was also determined.

Preliminary analyses were also performed on the corrosion and erosion properties of the as-plated and annealed ABCD plate. The increased resistance of the annealed ABCD plate compared to the as-plated ABCD coating to oxidation and erosion provides impetus for further study. Of particular importance is the mechanisms that cause the increased resistance. By isolating these mechanisms and knowing the behavior of the exposed coating from the present research, the proper heat treating can be imposed and tested.

Another area of future research is the behavior of the coatings after exposure to different temperatures. Using different temperatures, the alloy layer growth can be carefully controlled to provide the optimum combination of properties. In the end, combining all the information, a "customized" coating can be developed.

VII. References

(Agarwal, 1993):
Agarwal, Vishal, "A Model System for the Study of Chromized Coatings", A Thesis Presented to the Graduate Committee of Lehigh University in Candidacy for the Degree of Master of Science in Materials Science and Engineering, July 1993

(American Society for Metals, 1985):
American Society for Metals, Metals Handbook, Desk Edition, 1985

(American Society for Metals, 1982):
American Society for Metals, Metals Handbook, Ninth Edition (Volume 5, Surface Cleaning, Finishing and Coating), 1982 pages 170-187

(American Society for Metals, 1990):
American Society For Metals, Binary Alloy Phase Diagrams, Second Edition (Volume 1), Massalski, Thaddeus B., Ed.

(American Society for Metals 2, 1990):
American Society For Metals, Binary Alloy Phase Diagrams, Second Edition (Volume 2), Massalski, Thaddeus B., Ed.

(Blum et al., 1931):
Blum, W., Barrows, W.P., and Brenner, A., "The Porosity of Electroplated Chromium Coatings", *Bureau of Standards Journal of Research*, July 1931, Volume 7, pages 697-711

(Brittian and Smith, 1956):
Brittian, C.P. and Smith, G.C., "A Preliminary Investigation of the Formation of Cracks in Hard Chromium Electrodeposits and the Evolution of Hydrogen During Deposition", *Transactions of the Institute of Metal Finishing*, 1956, Volume 33, pages 289-300

(Bunshah, 1982):
Bunshah, Rointan F., et al., Deposition Technologies for Films and Coatings, 1982 pages 385-390

(Chapman and Anderson, 1974):
Chapman, Brian N. and Anderson, J. C., Science and Technology of Surface Coatings, 1974 pages 69-73

(Clark, 1963):
Clark, J.B., "Conventions for Plotting the Diffusion Paths in Multiphase

Ternary Diffusion Couples on the Isothermal Section of a Ternary Phase Diagram", *Transactions of the Metallurgical Society of AIME*, October 1963, Volume 227, pages 1250-1251

(Cleghorn and West, 1966):
Cleghorn, W.H., and West, J.M., "Stress in Very Thin Chromium Electrodeposits", *Transactions of the Institute of Metal Finishing*, 1966, Volume 44, pages 105-110

(Dennis and Such, 1993):
Dennis, J.K. and Such, T.E., Nickel and Chromium Plating (Third Edition), 1993, Woodhead Publishing Limited and ASM International, pages 205-217

(Dooley, 1991):
Dooley, Barry, "Boiler Tube Failures - A Perspective and a Vision", from International Conference on Boiler Tube Failures in Fossil Plants, Sponsored by EPRI, November 5-7, 1991

(Dupernell, 1977):
Dupernell, George, Electrodeposition of Chromium from Chromic Acid Solutions, 1977, Pergamon Press

(EPRI, 1989):
Boiler Tube Failure: Correction, Prevention, and Control, EPRI report GS-6467, Research Project 1890-7, Palo Alto, California, 1989

(Fan et al., 1992):
Fan, C., Celis, J.P., and Roos, J.R., "Effect of Substrate Pretreatment on the Porosity in Thin Nickel Electrodeposits", *Surface and Coatings Technology*, Volume 50, 1992, pages 289-294

(Glowacki and Kaluba, 1982):
Glowacki, Z. and Kaluba, W., "On Some Features of Chromium Carbide Diffusion Layer Formation", *Metallurgical Transactions A*, May 1982, Volume 13A, pages 753-759

(Herczeg, 1994):
Herczeg, Ronald, Homer Research Laboratory, Bethlehem Steel, Bethlehem, PA 18015, Personal communication

(Hoare, 1989):
Hoare, James P., "An Electrochemical Mystery Story: A Scientific Approach to Chromium Plating", *Plating and Surface Finishing*, September 1989, Volume 76, pages 46-52

(Hoflund, 1994):
Hoflund, Gar B., Department of Chemical Engineering, University of Florida, Gainsville, FL 32611, Personal communication

(Hoflund et al., 1986):
Hoflund, Gar B., Asbury, Douglas A., Babb, Steven J., Grogan, Austin L. Jr., Laitinen, Herbert A., and Hoshino, Shigeo, "A Surface Study of Amorphous Chromium Films Electrodeposited from Chromic Acid Solutions. Part I", *Journal of Vacuum Science Technology A*, January/February 1986, Volume 4, Number 1, pages 26-30

(Hoshino et al., 1986):
Hoshino, Shigeo, Laitinen, Herbert A., and Hoflund, Gar B., "The Electrodeposition and Properties of Amorphous Chromium Films Prepared from Chromic Acid Solutions", *Journal of the Electrochemical Society*, April 1986, Volume 133, Number 4, pages 681-685

(Jellinghaus and Keller, 1971):
Jellinghaus, W. and Keller, W., *Arch. Eisenhüttenwes.*, 1971, Volume 43, Number 4, pages 319-328

(Jones, 1989):
Jones, Allen R., "New in Hard Chromium Plating", *Products Finishing*, April 1989, Volume 53, pages 62-69

(Jones, 1993):
Jones, Allen R., Atotech USA Incorporated, Somerset, NJ 08875, Personal communication

(Kaluba and Foct, 1987):
Kaluba, W. and Foct, J., "Structural and Physicochemical Factors Controlling the Formation of Chromium Carbide Cases During Chromizing", Advances in Surface Treatments, Pergamon Press, New York, 1987

(Kaluba and Wachowiak, 1983):
Kaluba, W., and Wachowiak, A., "Microstructure and Formation Mechanism of Complex Chromium Diffusion Layer", *Arch. Eisenhüttenwes.*, April 1983, Volume 54, Number 4, pages 161-166

(Klein, 1987):
Klein, D., "Trend-setting Chromium Techniques", *Finishing*, October 1987, Volume 11, Number 10, pages 34-36

(Kou, 1953):
Kou, K., *Journal of the Iron and Steel Institute*, 1953, Volume 173, pages 363-375

(Kushner, 1973):
Kushner, J.B., "Stress in Electrodeposited Metals: 115 Years Later", *Plating*, September 1973, Volume 60, pages 1246-1251

(Lindsley et al., 1993):
Lindsley, B.A., Marder, A.R., and Lewnard, J.J., "The Effect of FBC Particle Characteristics on Erosion of a Low Alloy Steel", 12th International Conference on Fluidized Bed Combustion, May 9-13, 1993, San Diego, CA, USA

(Lowenheim, 1963):
Lowenheim, Frederick A.,Ed., Modern Electroplating (Second Edition), John Wiley & Sons, Inc., 1963

(Marder et al., 1985):
Marder, A.R., Perpetua, S.M., Kowalik, J.A., and Stephenson, E.T., "The Effect of Carbon Content on the Kinetics of Decarburization in Fe-C Alloys", *Metallurgical Transactions A*, June 1985, Volume 16A, pages 1160-1163

(McCormick and Dobson, 1987):
McCormick, M. and Dobson, S.J., "Characteristics and Properties of Electrodeposited Chromium from Solutions with Varying Sulphate Ratios", *Transactions of the Institute of Metal Finishing*, 1987, Volume 65, page 24-32

(McCormick and Dobson 2, 1987):
McCormick, M. and Dobson, S.J., "Characteristics and Properties of Electrodeposited Chromium from Aqueous Solutions", *Journal of Applied Electrochemistry*, 1987, Volume 17, pages 303-314

(Menzies and Mortimer, 1966):
Menzies, I. A. and Mortimer, D., "Observations on the Chromizing of Iron and Plain Carbon Steels", *Journal of the Iron and Steel Institute*, 1966, Volume 204, pages 539 - 558

(Metselaar, 1988):
Metselaar, R., "Diffusion in Solids, Part III: Diffusion in Multicomponent Systems", *Journal of Materials Education*, 1988, Volume 10, Number 6 pages 621-644

(Niebo, 1991):
Niebo, Ronald J., "Implementing a Boiler Tube Failure Mechanism Reporting Program", from International Conference on Boiler Tube Failures in Fossil Plants, Sponsored by EPRI, November 5-7, 1991

(Rivlin, 1984):
Rivlin, V.G., "Phase Equilibria in Iron Ternary Alloys 14: Critical Review of Constitution of Carbon-Chromium-Iron and Carbon-Iron-Magnesium Systems", *International Metals Reviews*, 1984, Volume 29, Number 4, pages 299-327

(Saiddington and Hoey, 1974):
Saiddington, J.C. and Hoey, G.R., "Crack-free Chromium from Conventional Plating Baths", *Plating*, October 1974, Volume 61, pages 923-930

(Snavely, 1947):
Snavely, Cloyd A., "A Theory for the Mechanism of Chromium Plating; A Theory for the Physical Characteristics of Chromium Plate", *Transactions of the Electrochemical Society*, 1947, Volume 92, page 537-577

(Stott and Wood, 1988):
Stott, F.H. and Wood, G.C., "Internal Oxidation", *Materials Science and Technology*, December 1988, Volume 4, Number 12, pages 1072-1078

(Sully, 1954):
Sully, A.H., Chromium, Butterworths Scientific Publications, 1954

(Tsai and Wu, 1989):
Tsai, Rung-Ywan and Wu, Shinn-Tyan, "The Microstructure of Devitrified Amorphous Chromium Plating", *Journal of the Electrochemical Society*, May 1989, Volume 136, Number 5, pages 1341-1346

(Tsai and Wu, 1990):
Tsai, Rung-Ywan and Wu, Shinn-Tyan, "Phase Stability of Chromium Plating from Chromic Acid Electrolyte Containing Formic Acid", *Journal of the Electrochemical Society*, October 1990, Volume 137, Number 10, pages 3057-3060

(Varotsos et al., 1988):
Varotsos, C., et al., "Correlation of the Diffusion Coefficients of Various Elements Diffusing in Ferromagnetic and Paramagnetic αFe", *Physica Status Solidi (a)*, 1988, Volume 107, pages K109-K114

(Wilson and Turley, 1989):
Wilson, B.A. and Turley, D.M., "Development and Characteristics of Crack-free Chromium Coatings Produced by Electroplating", *Transactions of the Institute of Metal Finishing*, 1989, Volume 67, pages 104-108

(Zancheva et al., 1978):
Zancheva, L., Hillert, M., Lange, N., Seetharaman, S., and Staffansson, L.-I., "On the Formation of Carbide Coatings by Chromizing Carbon Steels", *Metallurgical Transactions A*, July 1978, Volume 9A, pages 909-915

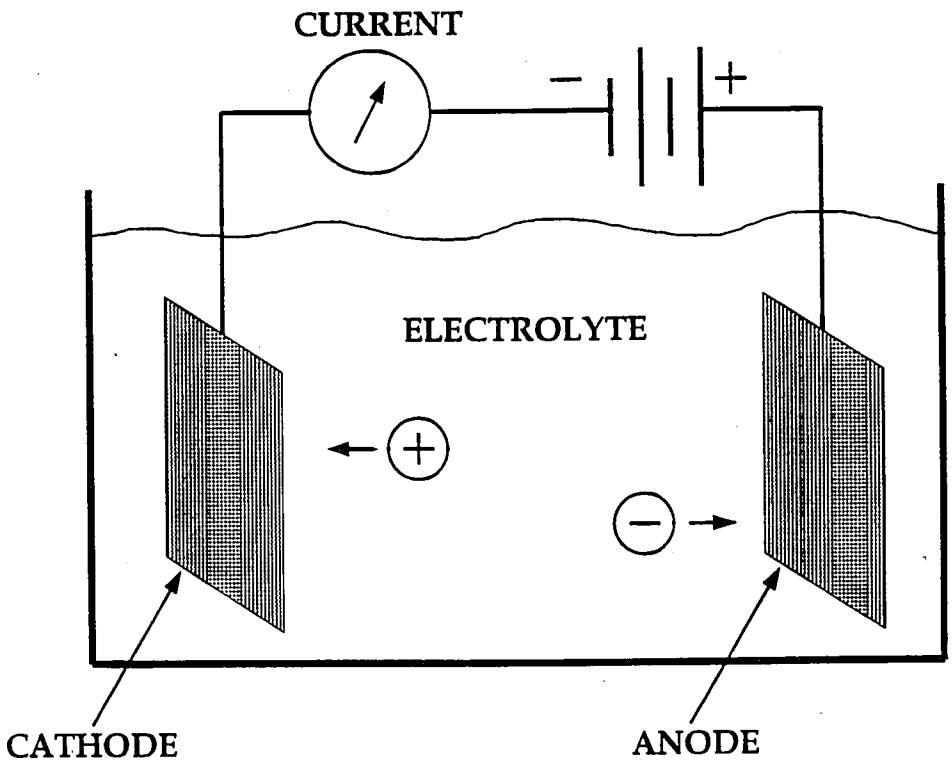

Figure 1. A schematic diagram representing a simplified plating cell (Chapman and Anderson, 1974)

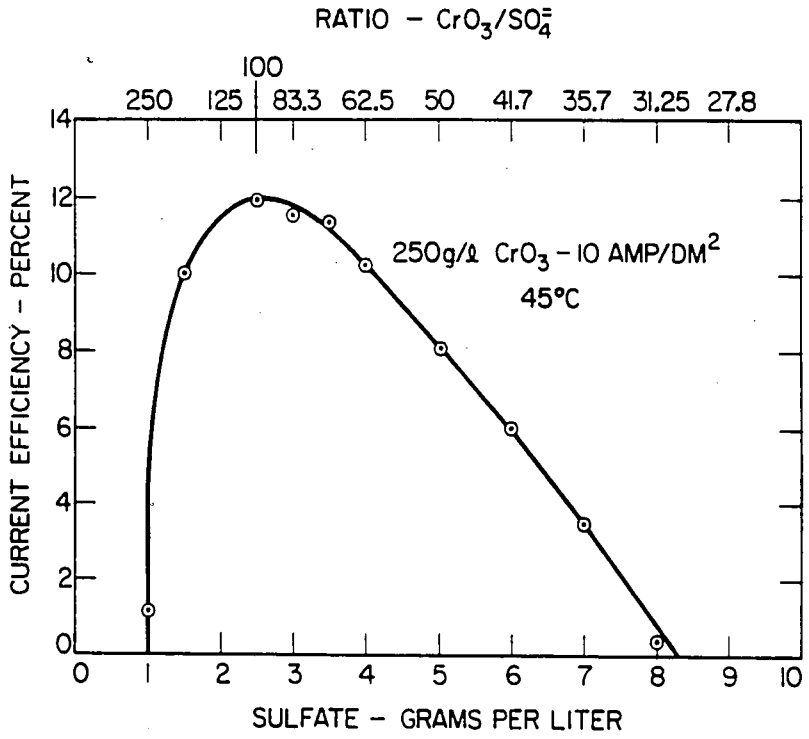

Figure 2. Current Efficiency versus Sulfate Concentration. Maximum current efficiency is reached at approximately the 100:1 ratio of CrO_3:SO_4^- (Dubpernell, 1977).

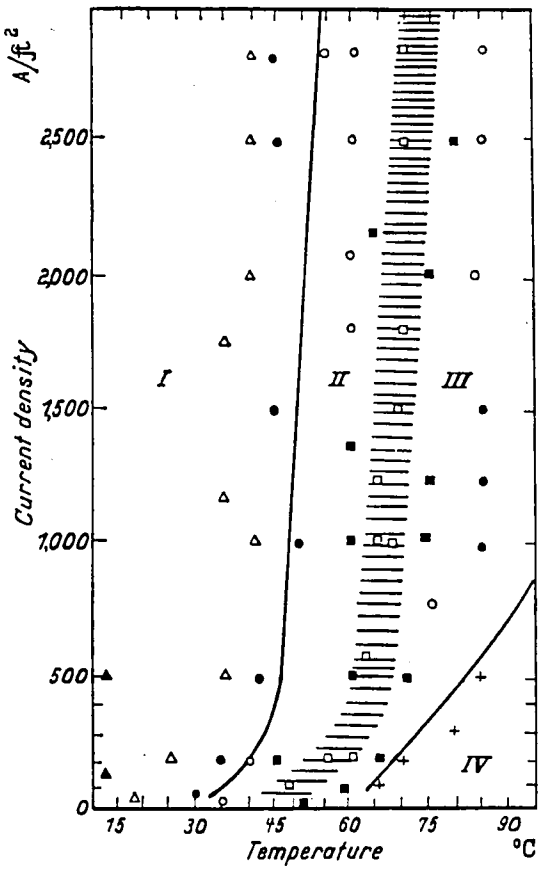

Figure 3. Variation of appearance of deposits with current density and with temperature. (Sully, 1954)

***Zone I*: Not bright, but dark matte appearance; at lower temperatures they were dark brown and at low current densities they became flaky**

***Zone II*: Deposits were brighter as the temperature was increased, brightest deposits were found between *Zones II* and *III*, but boundary between these zones is not well-defined**

***Zone III*: Occurred at temperatures >60°C and current densities >400 to 500 A/ft²; deposits became less bright and developed a matte appearance**

***Zone IV*: No deposition at all**

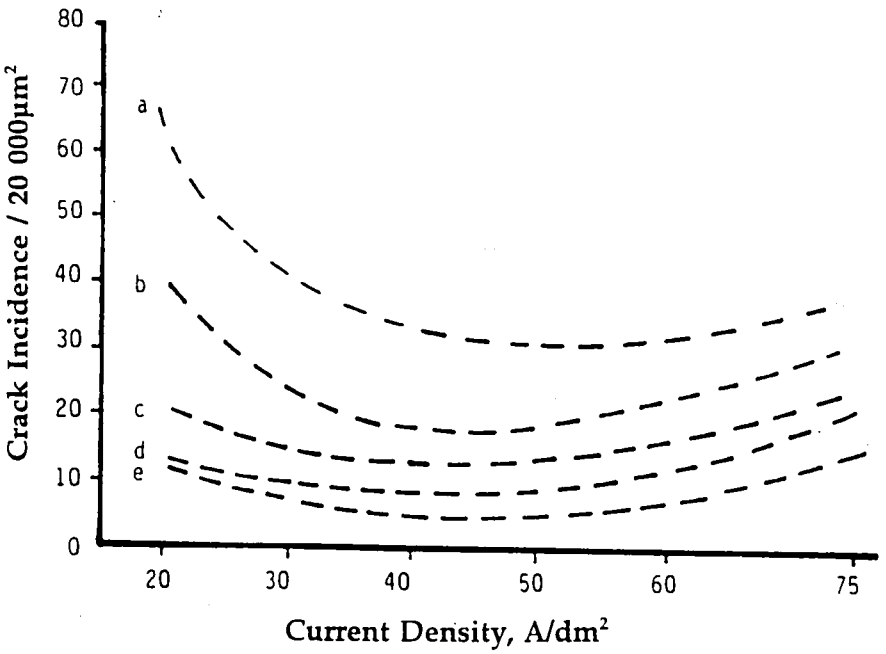

Figure 4. Crack incidence per 20 000 μm² versus current density for various sulphate ratios: (a) 80:1, (b) 90:1, (c) 100:1, (d) 110:1, and (e) 125:1 (McCormick and Dobson 2, 1987)

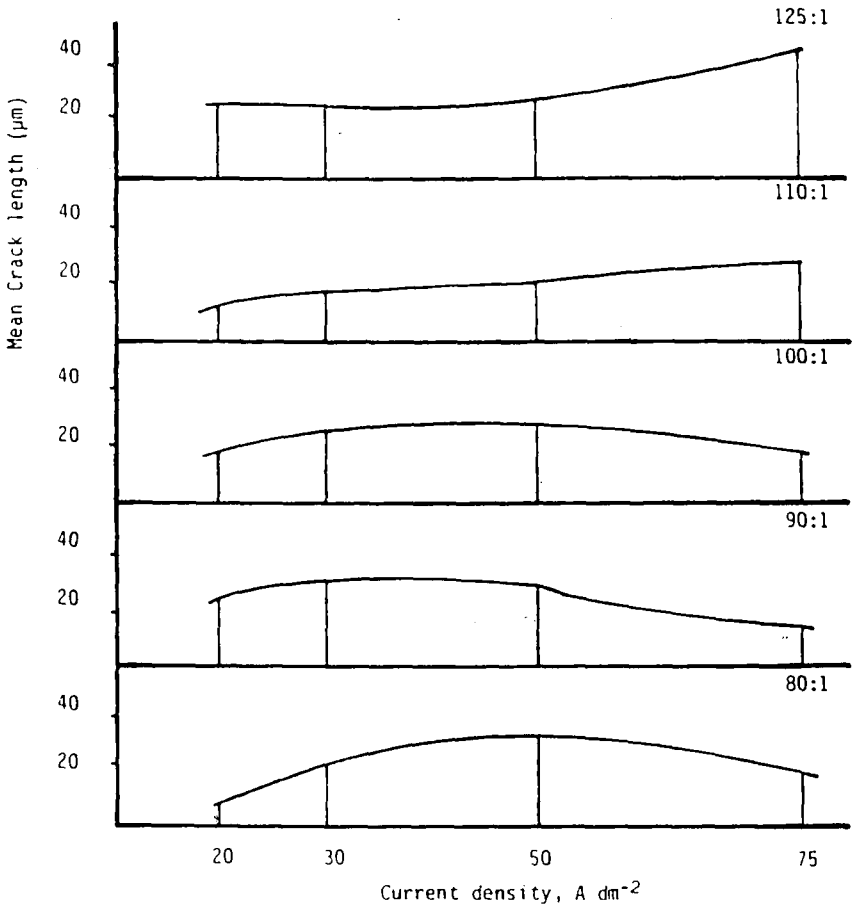

Figure 5. Mean crack length versus current density for various sulphate ratios (McCormick and Dobson 2, 1987)

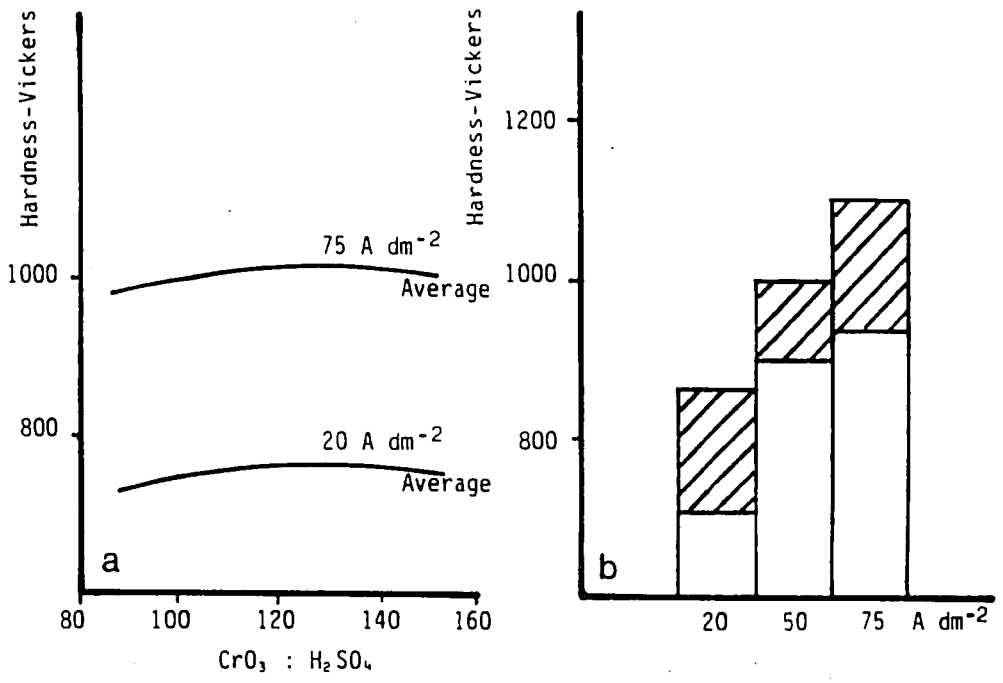

Figure 6. (*right*) **Variation of microhardness with sulphate ratio;** (*left*) **Variation in microhardness with current density for a sulphate ratio of 100:1 (McCormick and Dobson 2, 1987)**

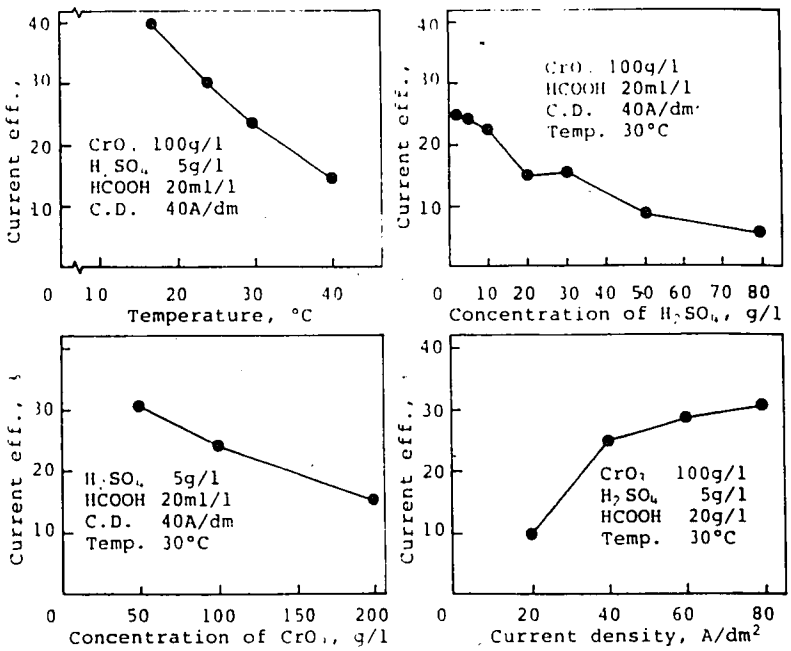

Figure 7. Current efficiency of ABCD bath as a function of temperature, sulfuric acid concentration, chromic acid concentration, and current density (Hoshino et al., 1986)

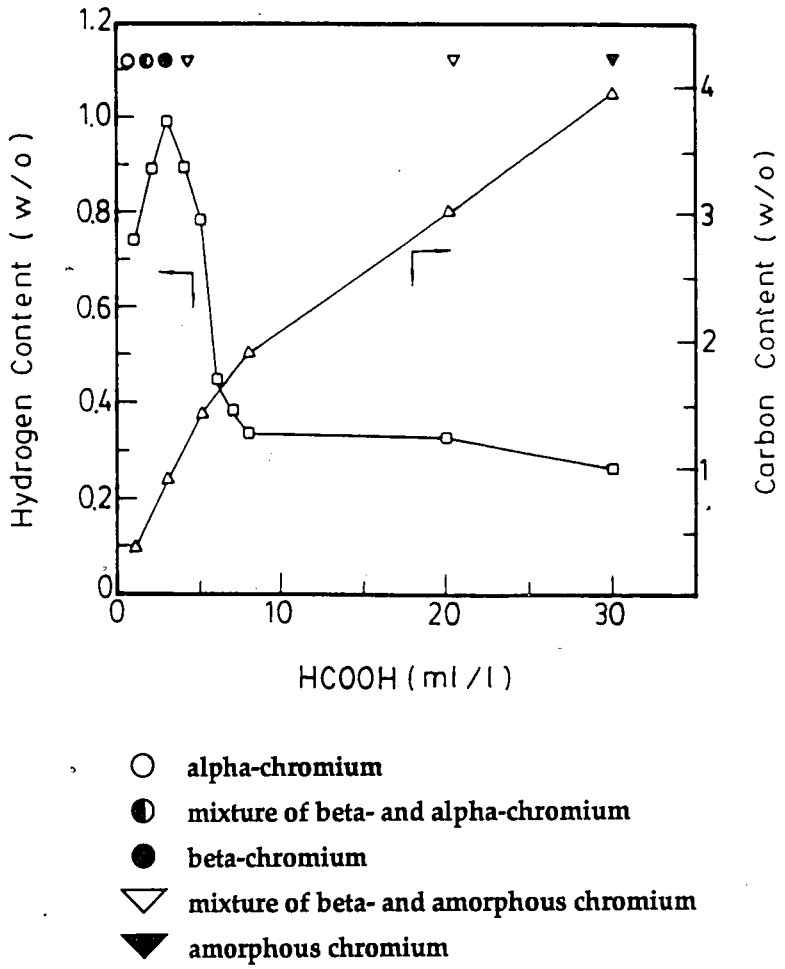

Figure 8. Amount of hydrogen and carbon in ABCD plate as a function of formic acid concentration (Tsai and Wu, 1989)

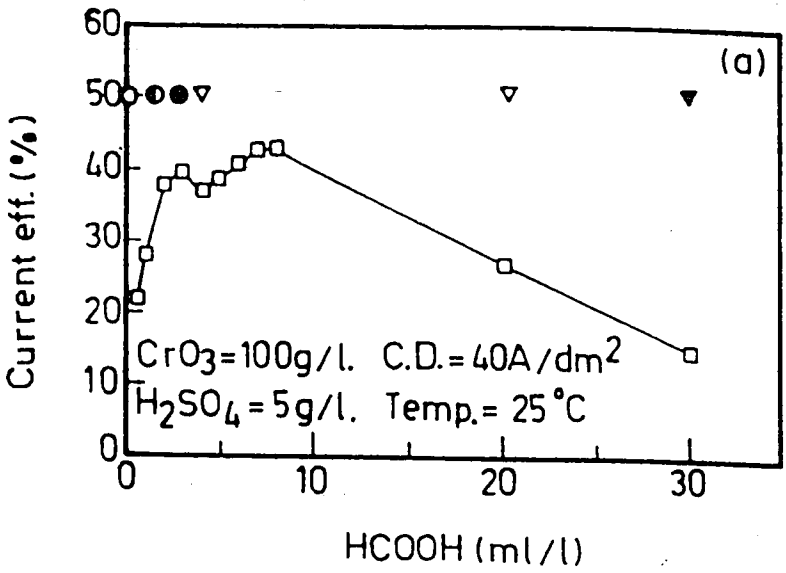

○ alpha-chromium

◐ mixture of beta- and alpha-chromium

● beta-chromium

▽ mixture of beta- and amorphous chromium

▼ amorphous chromium

Figure 9. Current efficiency of ABCD bath as a function of formic acid concentration (Tsai and Wu, 1990)

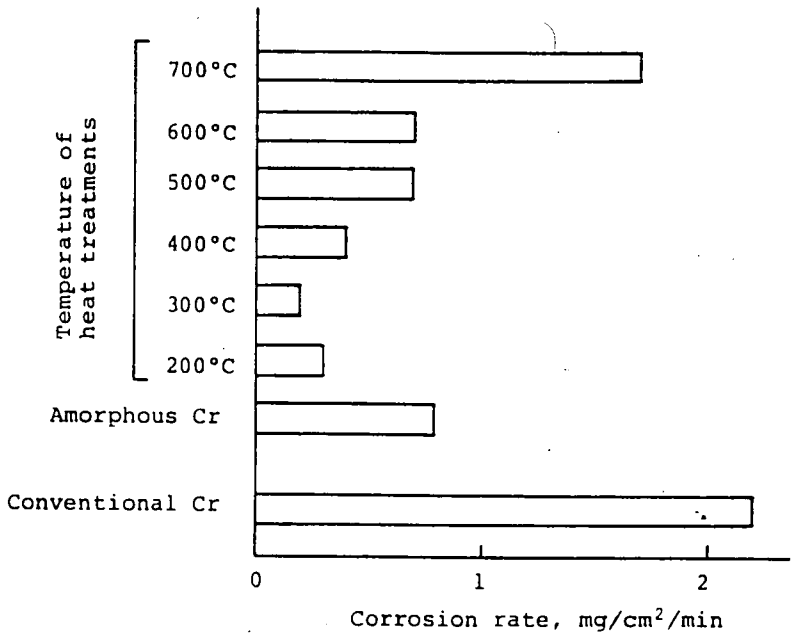

Figure 10. Dissolution rates of as-plated and annealed ABCD plates in a hydrochloric acid (1:1) solution. The dissolution rate of a conventional chromium plate is also displayed (Hoshino et al., 1986)

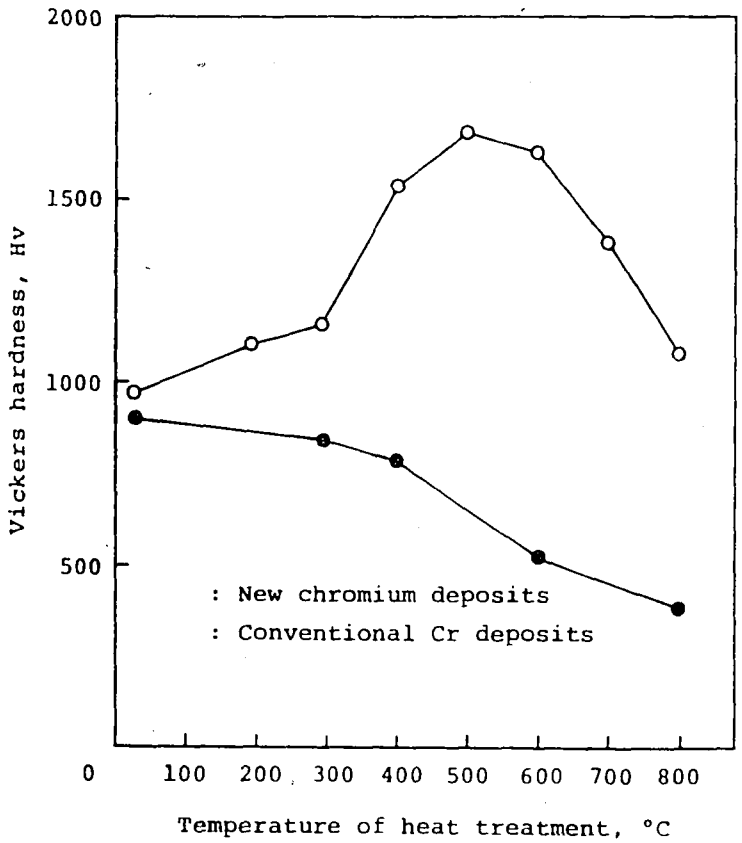

Figure 11. Vickers hardness values of ABCD plates as a function of annealing temperature. The plates were exposed for one hour (Hoshino et al., 1986)

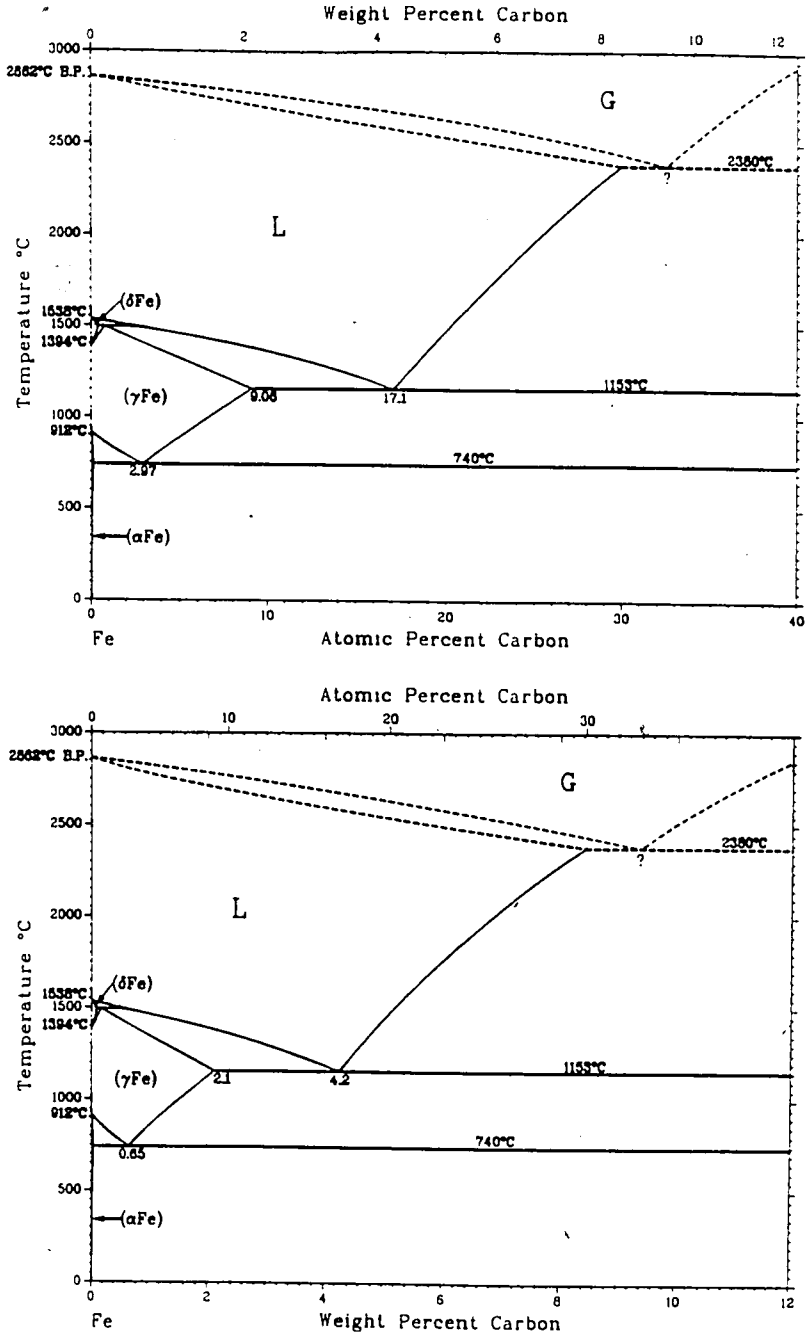

Figure 12a. Iron-carbon phase diagram (ASM, 1990)

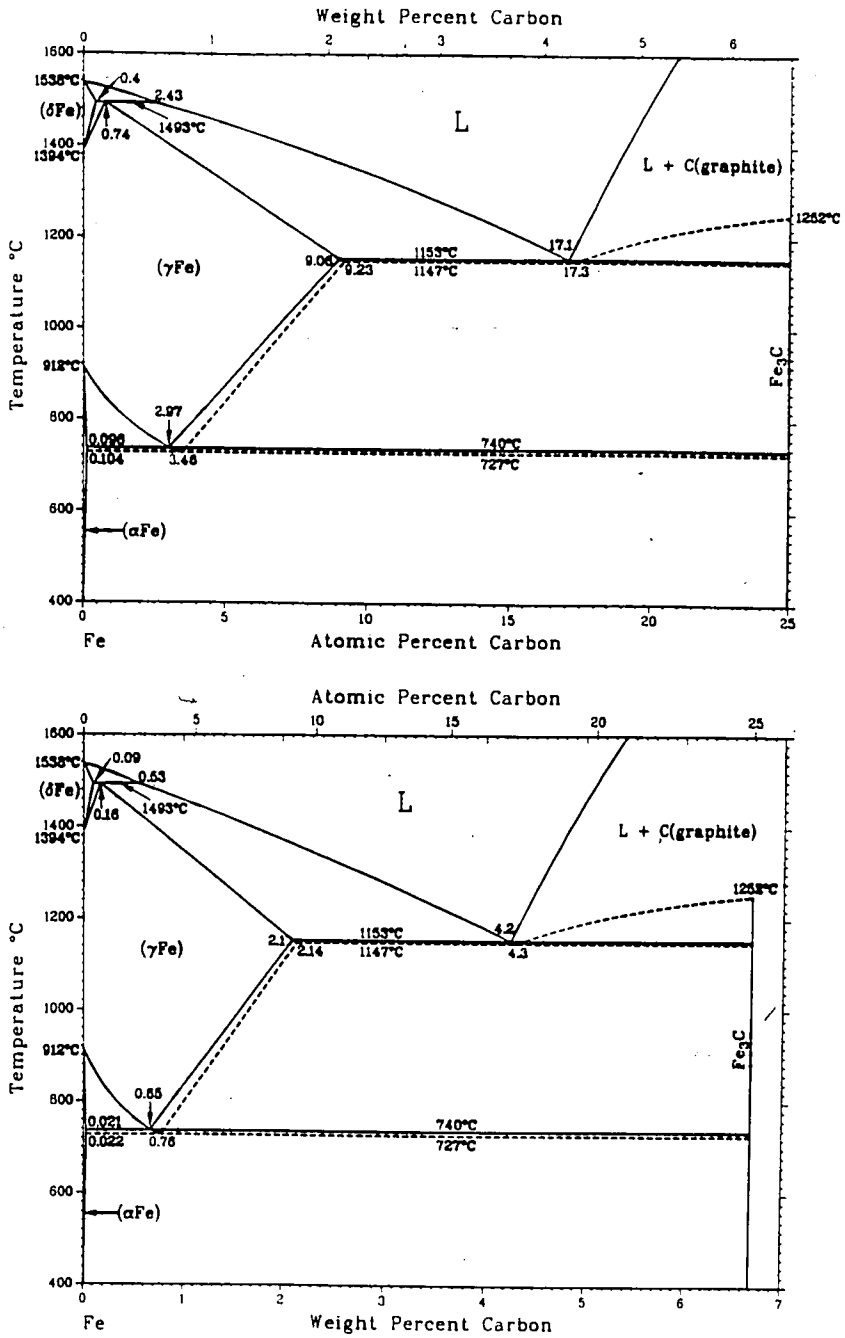

Figure 12b. Iron-carbon phase diagram (ASM, 1990)

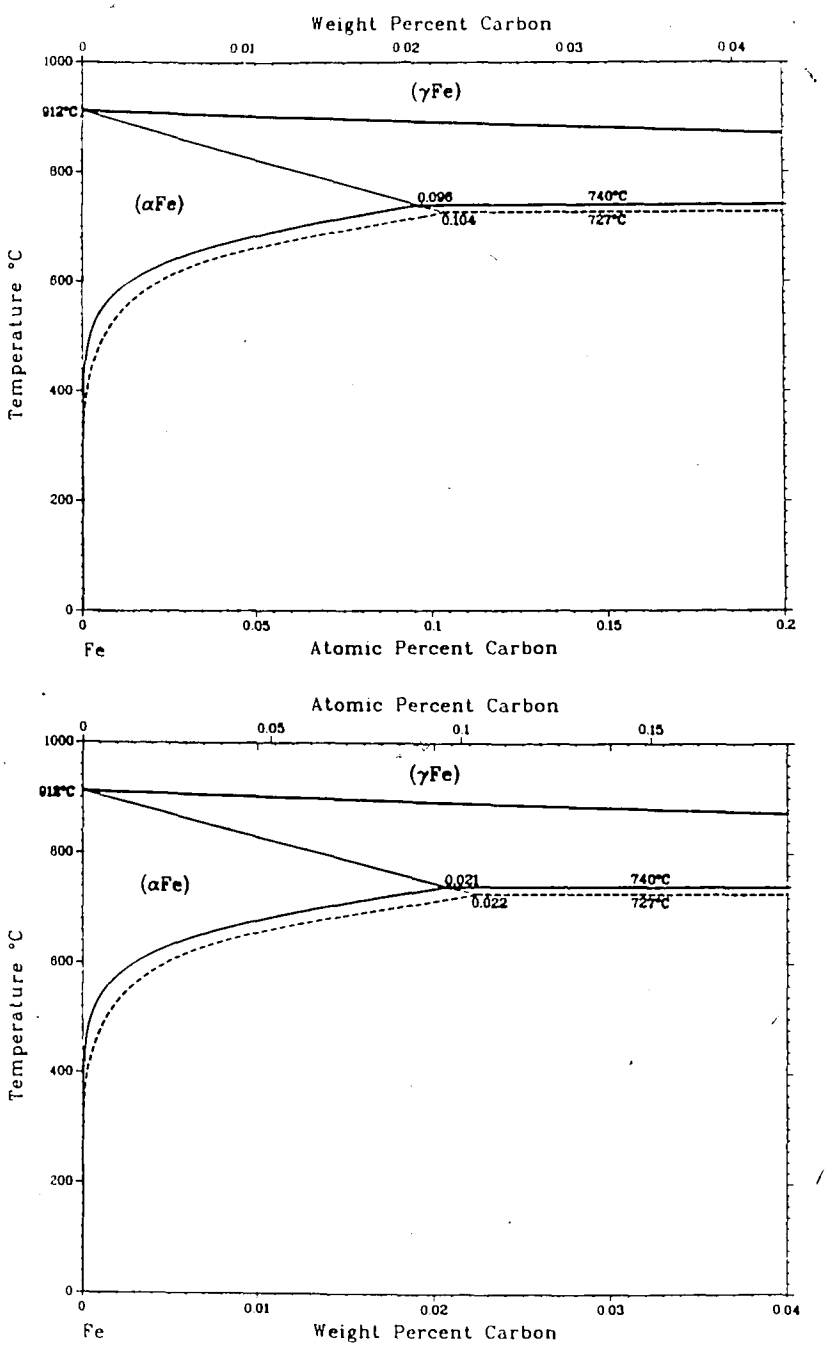

Figure 12c. Iron-carbon phase diagram (ASM, 1990)

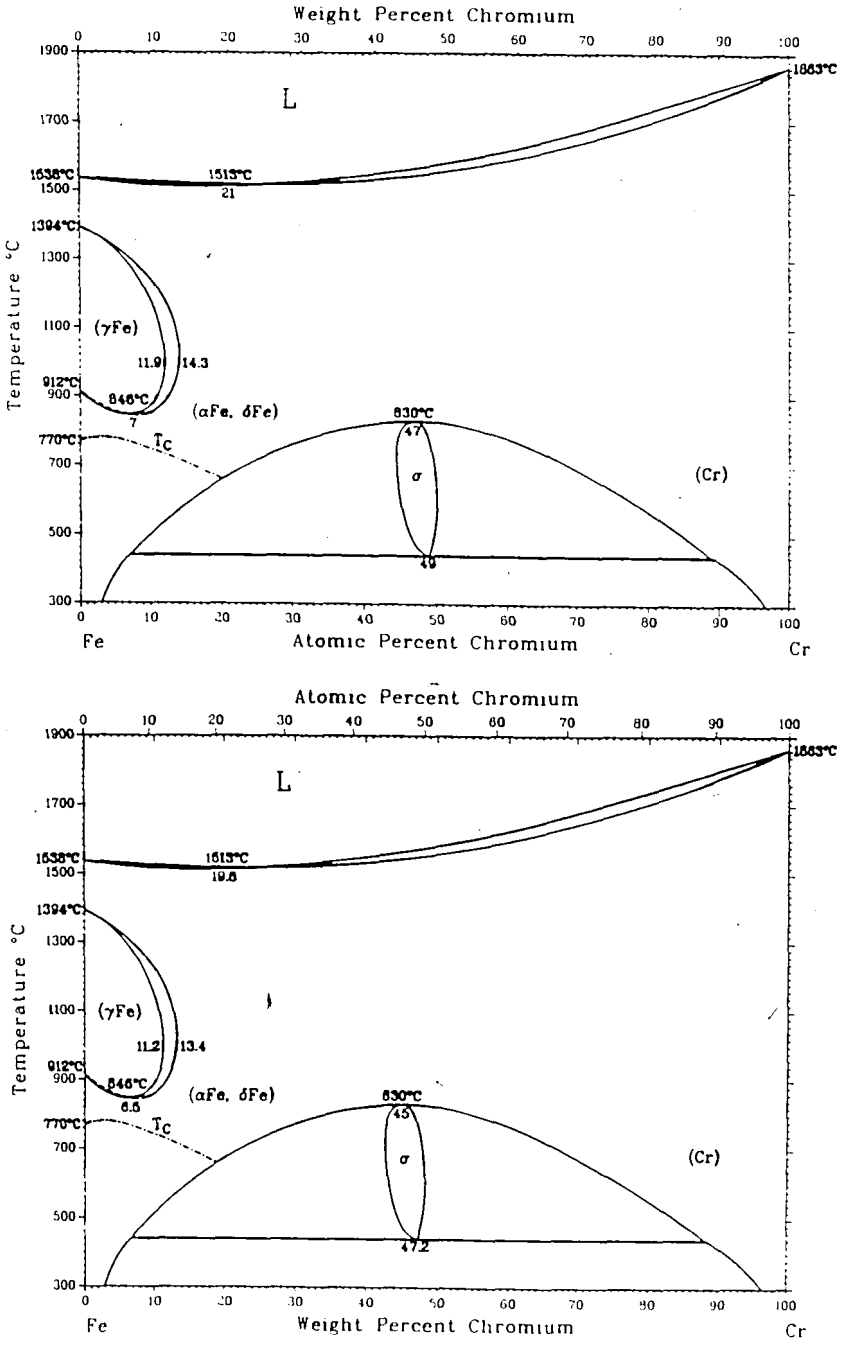

Figure 13. Iron-chromium phase diagram (ASM 2, 1990)

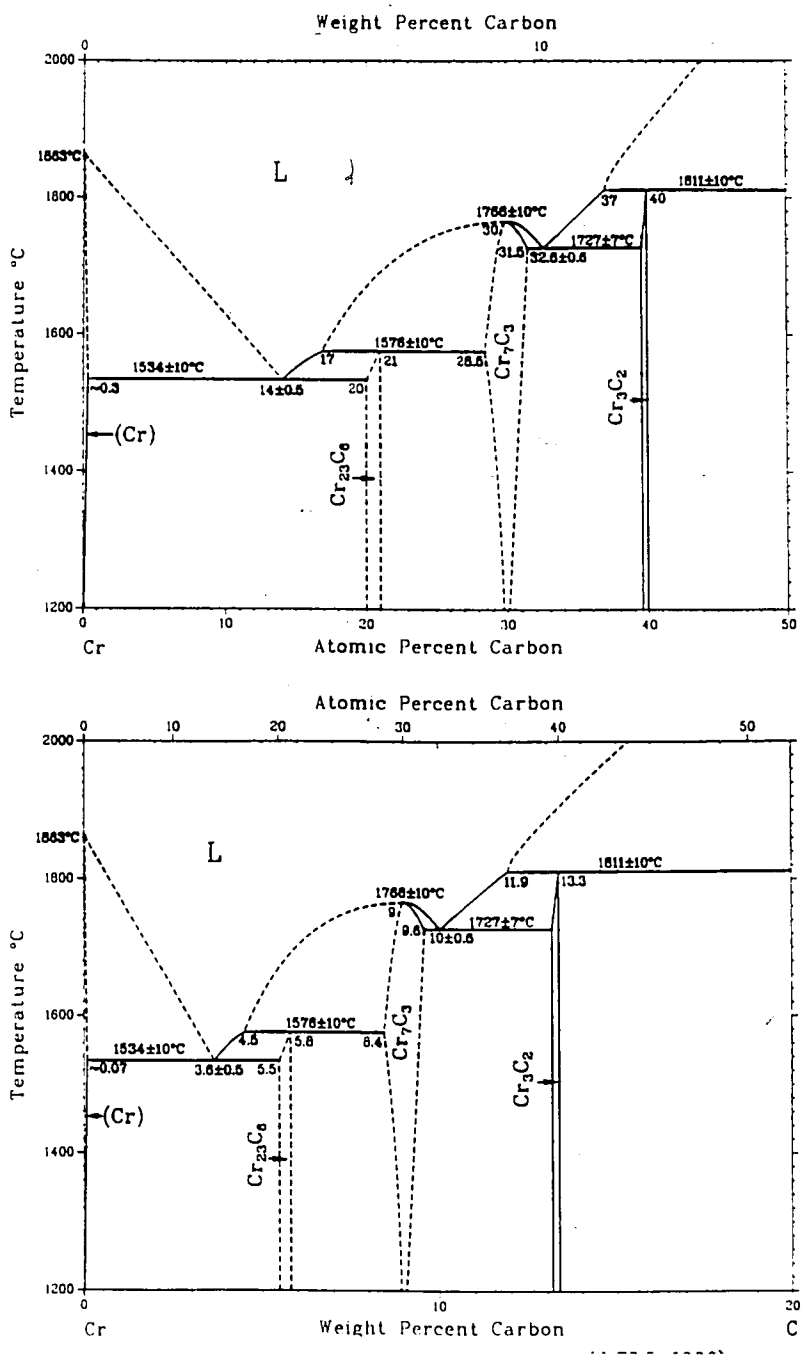

Figure 14. Chromium-carbon phase diagram (ASM, 1990)

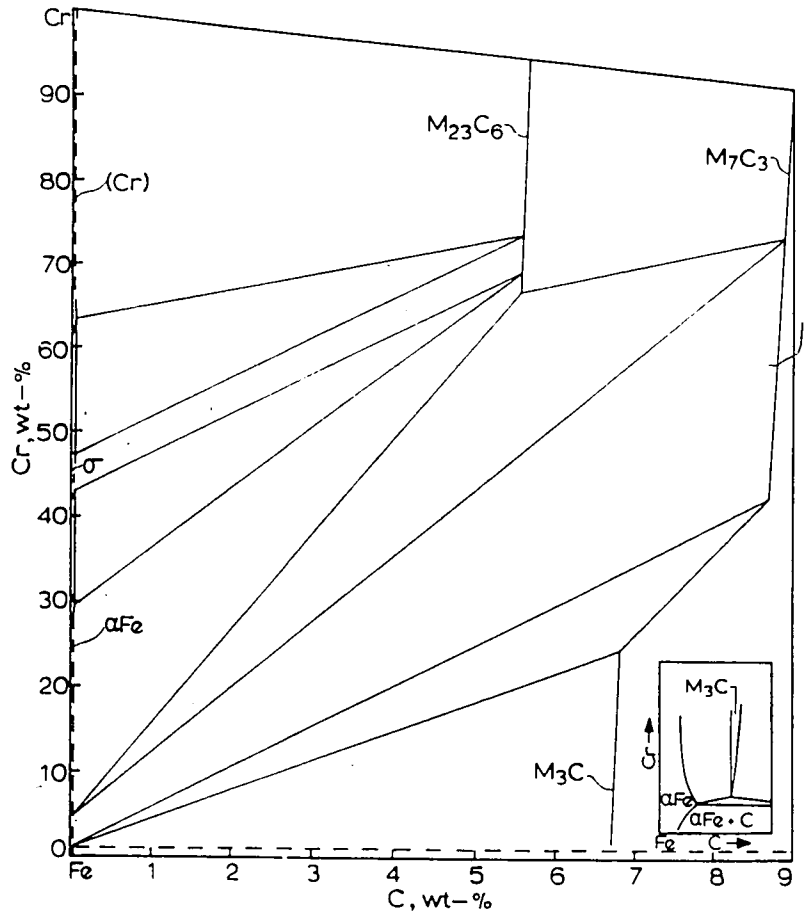

Figure 15. 700°C isotherm of the iron-chromium-carbon system. Inset sketch illustrates the expected stable equilibria between γFe and cementite (Rivlin, 1984)

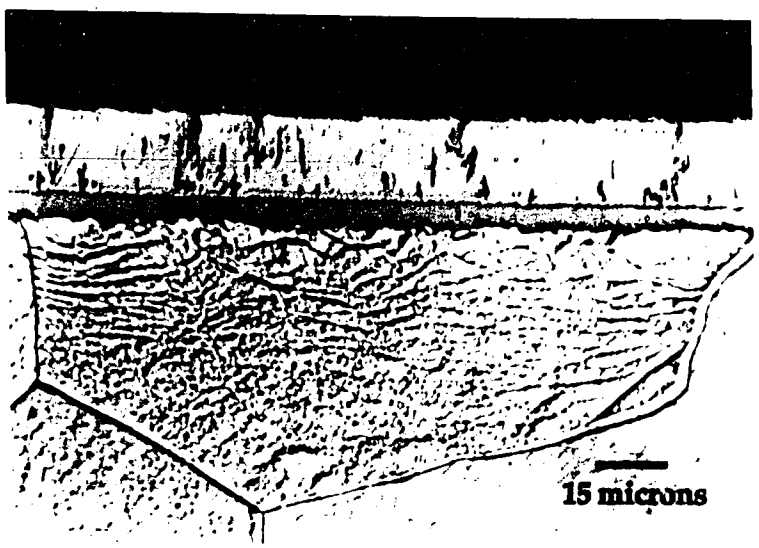

Figure 16. Light optical micrograph showing the reaction layer below the conventional chromium plate after exposure at 600°C (1500x) (Agarwal, 1993)

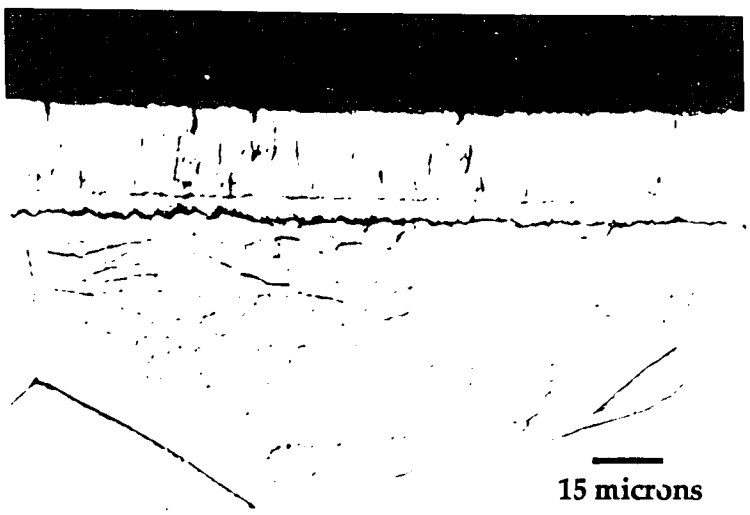

Figure 16. Light optical micrograph showing the reaction layer below the conventional chromium plate after exposure at 600°C (1500x) (Agarwal, 1993)

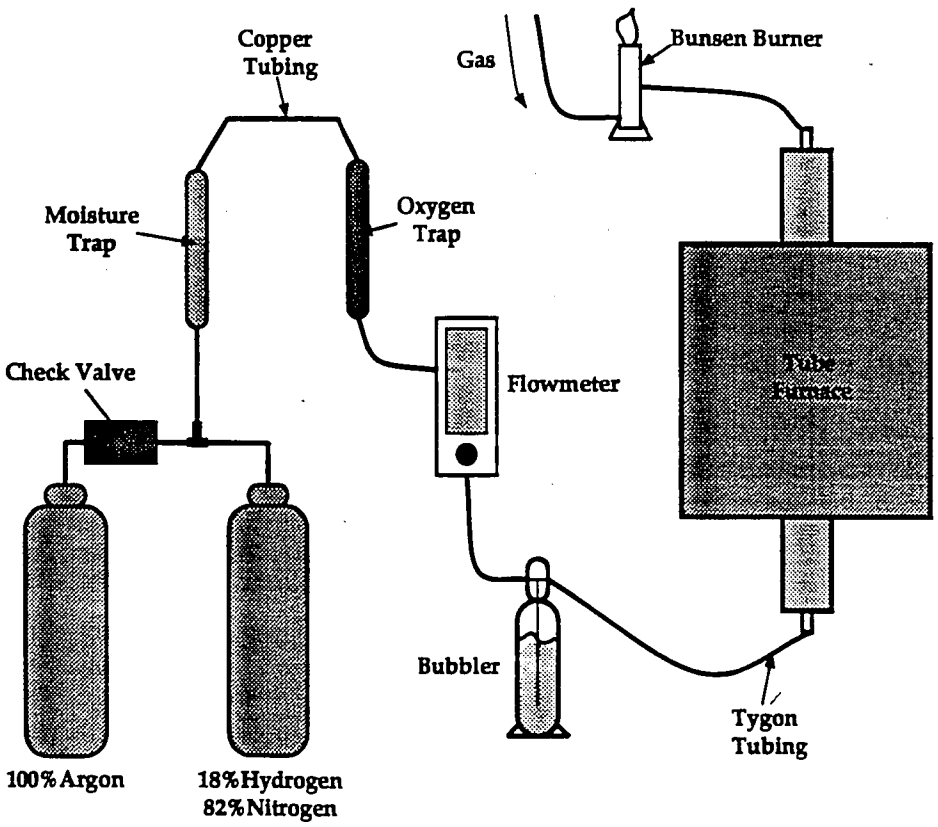

Figure 17. Schematic diagram of the decarburization set-up

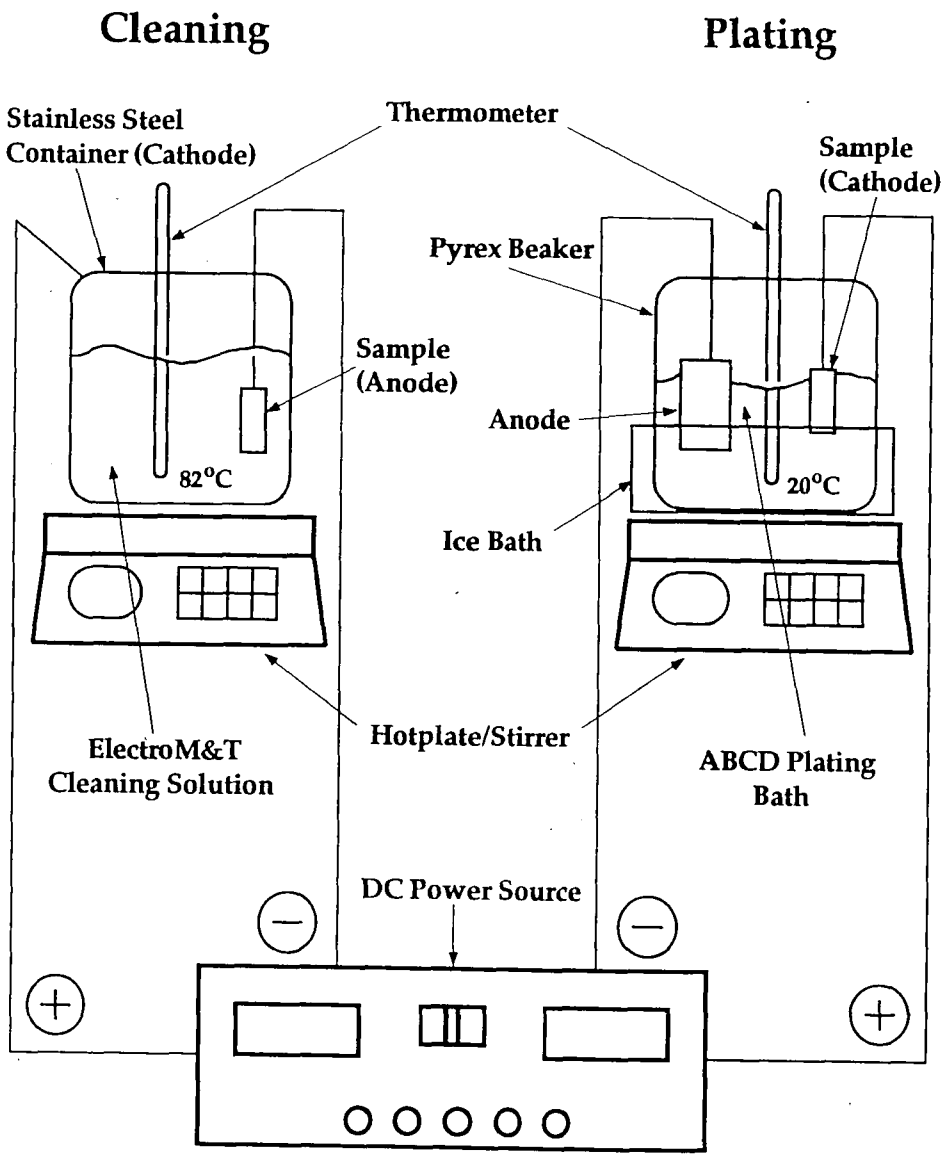

Figure 18. Schematic diagram of electrodeposition facilities

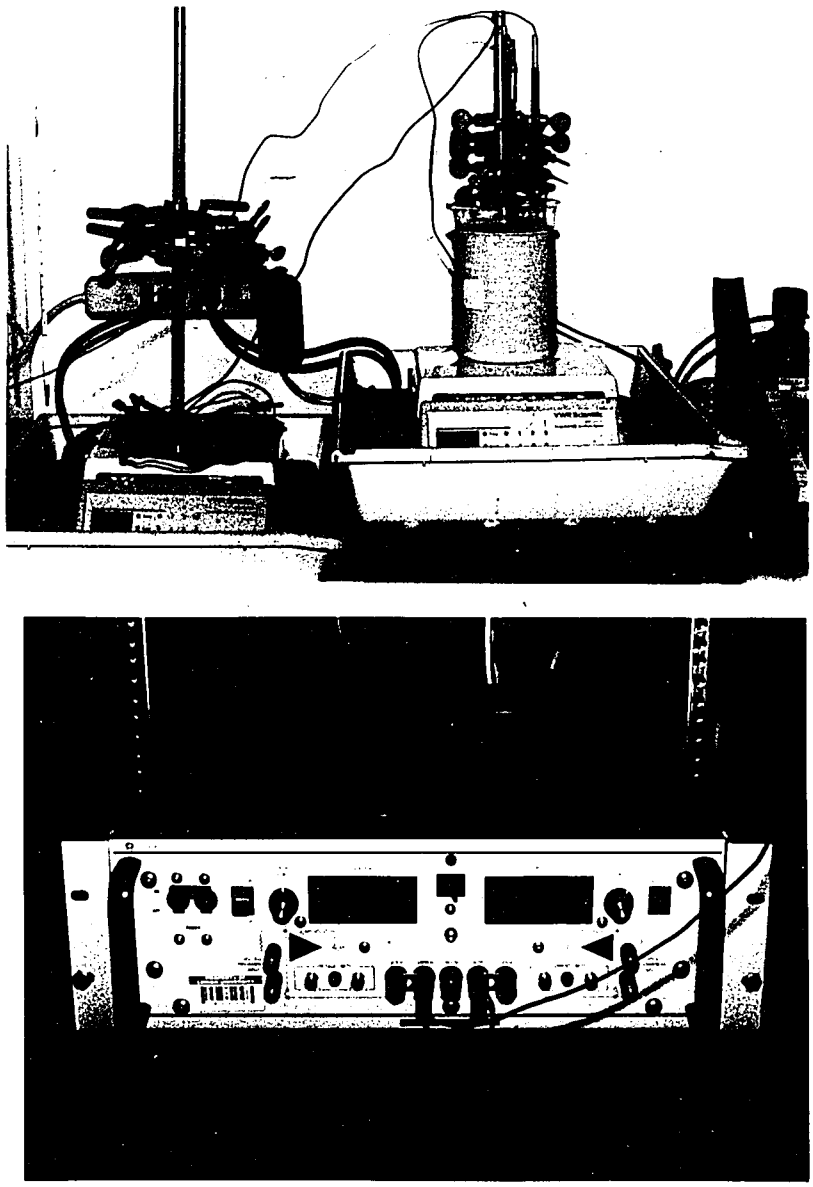

Figure 19. Picture of electrodeposition facilities and power source at Lehigh University

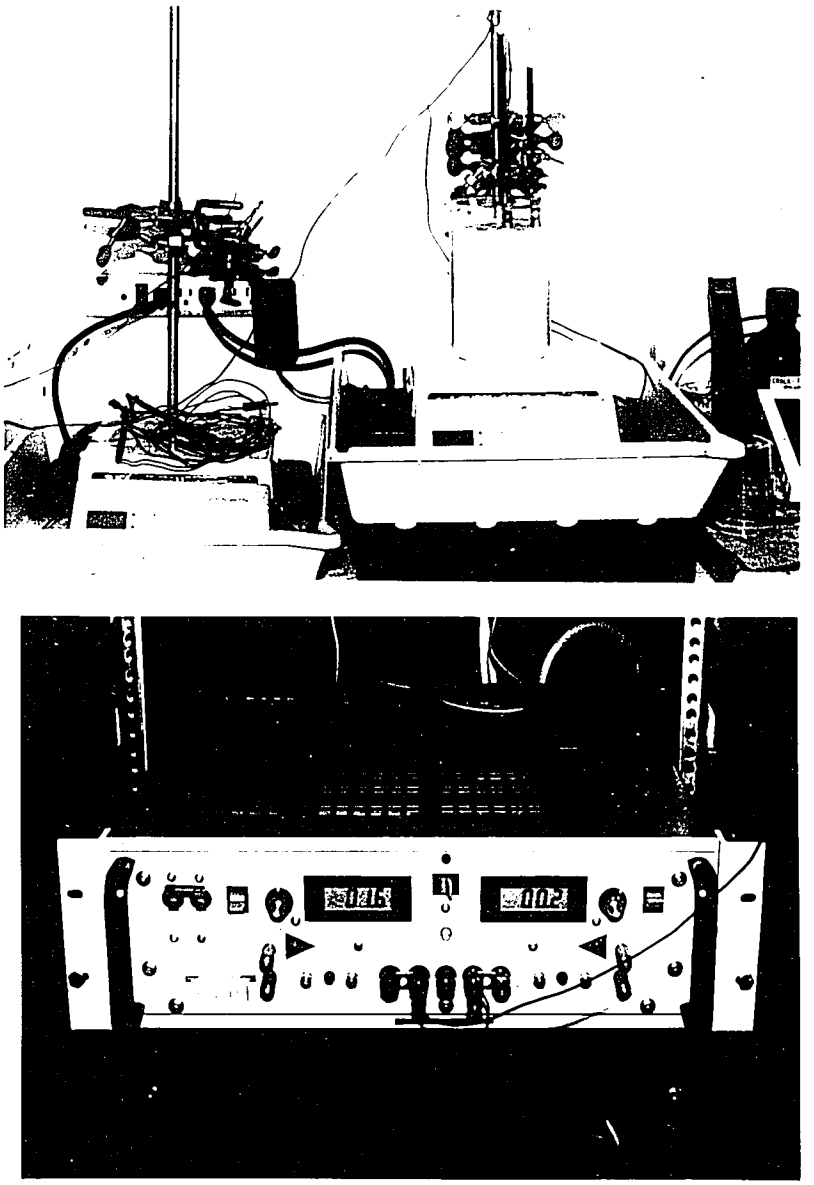

Figure 19. Picture of electrodeposition facilities and power source at Lehigh University

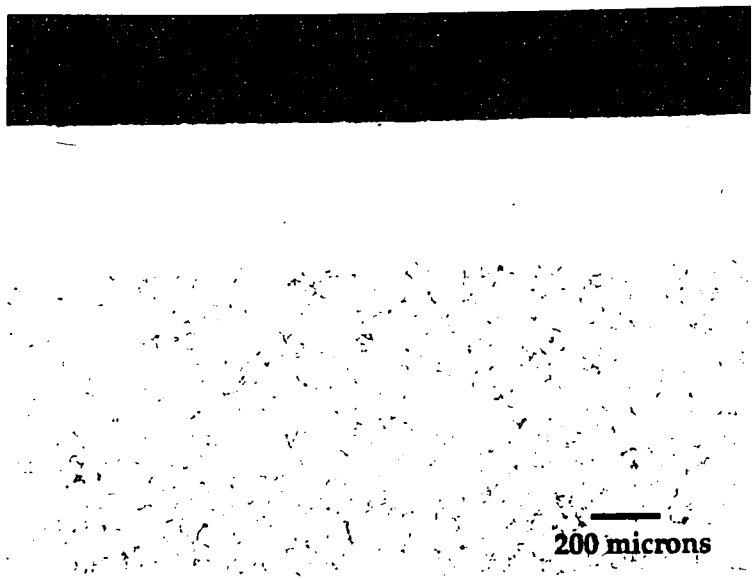

Figure 20a. Cross-sectional light optical micrograph of iron-carbon substrate after one hour of decarburization (50x)

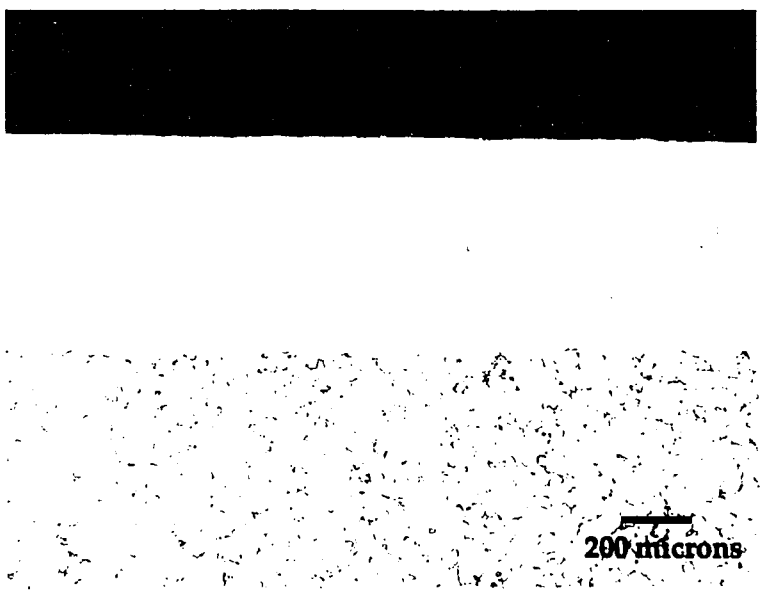

Figure 20b. Cross-sectional light optical micrograph of iron-carbon substrate after two hours of decarburization (50x)

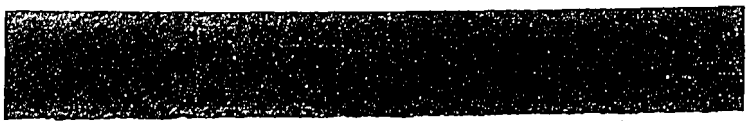

200 microns

Figure 20a. Cross-sectional light optical micrograph of iron-carbon substrate after one hour of decarburization (50x)

200 microns

Figure 20b. Cross-sectional light optical micrograph of iron-carbon substrate after two hours of decarburization (50x)

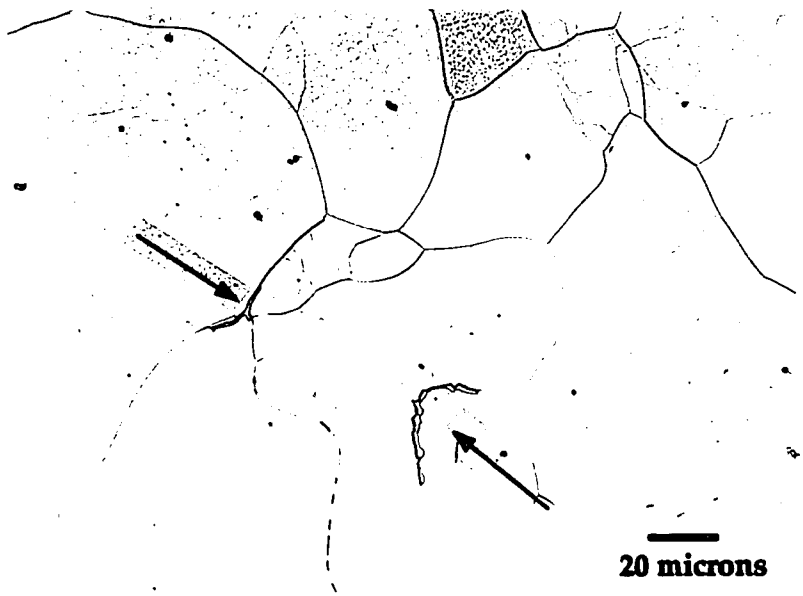

Figure 21. Carbides seen in the equiaxed grain structure in the decarburized region of the iron-carbon substrates (500x)

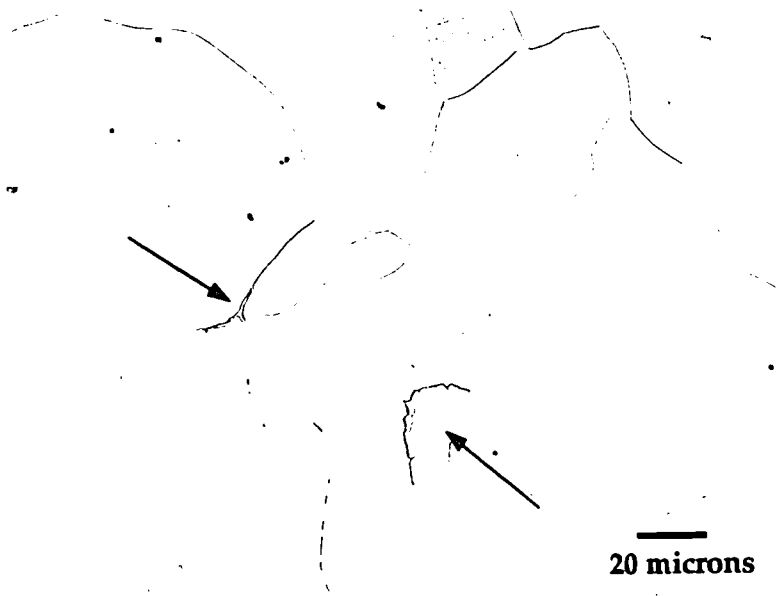

Figure 21. Carbides seen in the equiaxed grain structure in the decarburized region of the iron-carbon substrates (500x)

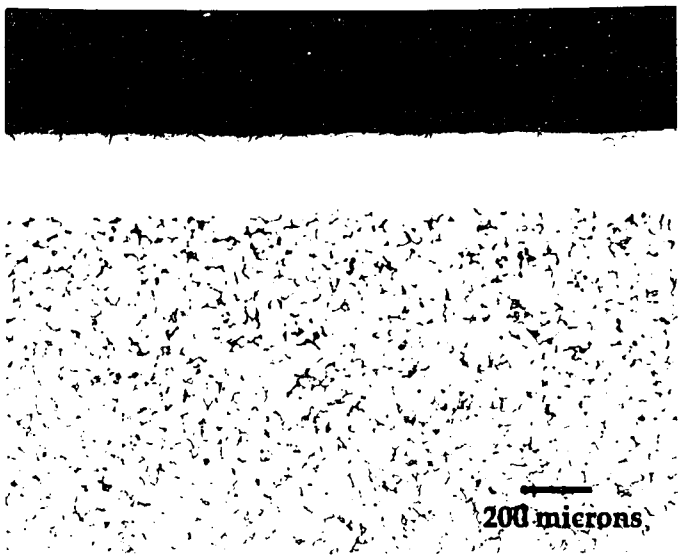

Figure 22a. Cross-sectional light optical micrograph of decarburized sample after grinding and polishing operations. The depth of the decarburization is 200μm (50x)

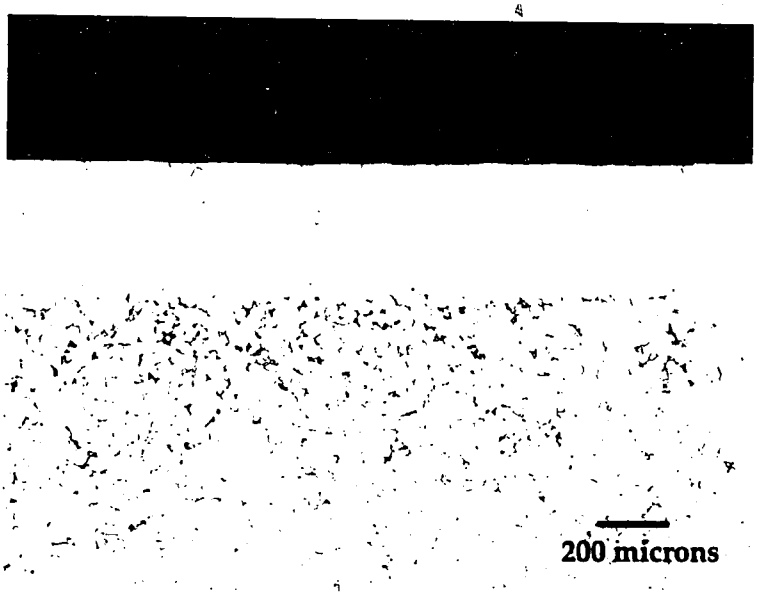

Figure 22b. Cross-sectional light optical micrograph of decarburized sample after grinding and polishing operations. The depth of the decarburization is 400μm (50x)

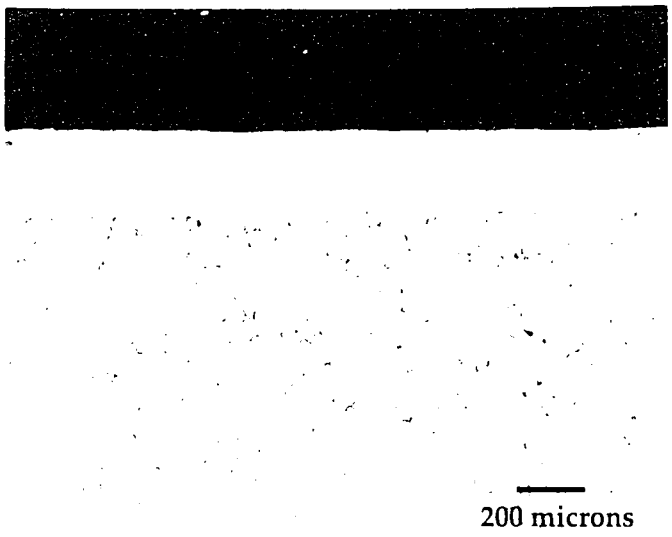

Figure 22a. Cross-sectional light optical micrograph of decarburized sample after grinding and polishing operations. The depth of the decarburization is 200μm (50x)

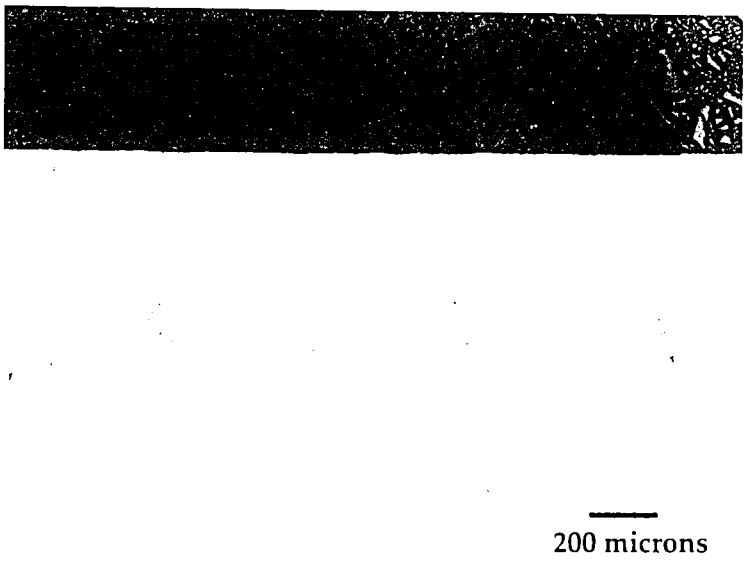

Figure 22b. Cross-sectional light optical micrograph of decarburized sample after grinding and polishing operations. The depth of the decarburization is 400μm (50x)

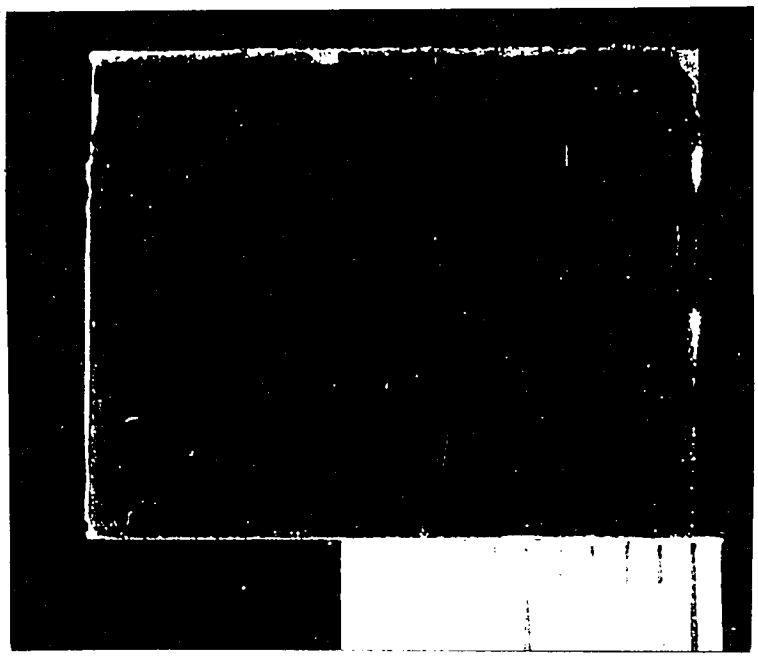

Figure 23. Optical macrograph of surface of as-plated ABCD sample

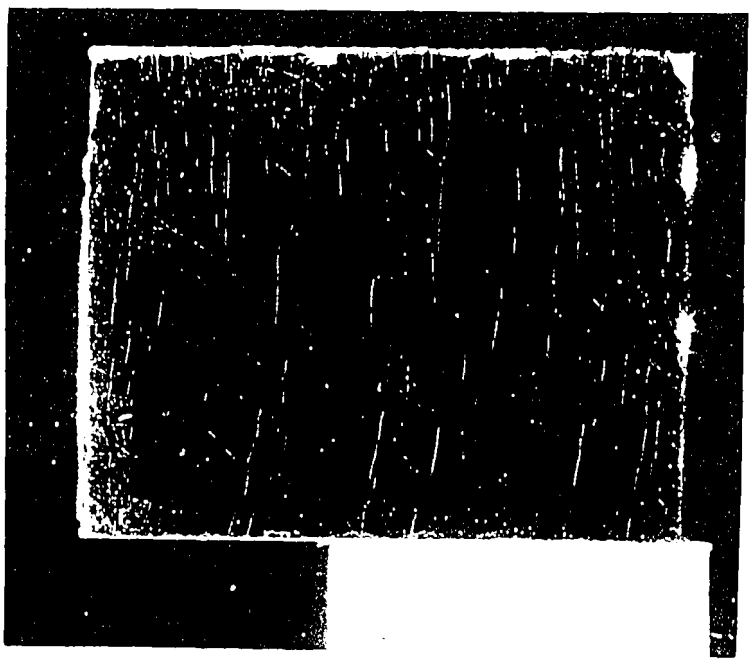

Figure 23. Optical macrograph of surface of as-plated ABCD sample

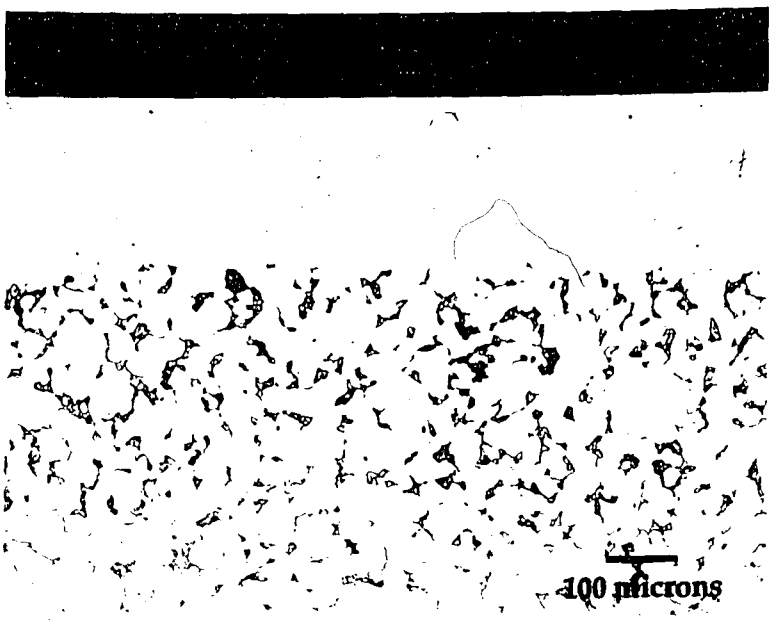

Figure 24. Cross-sectional light optical micrograph of ABCD plate on top of decarburized substrate (100x)

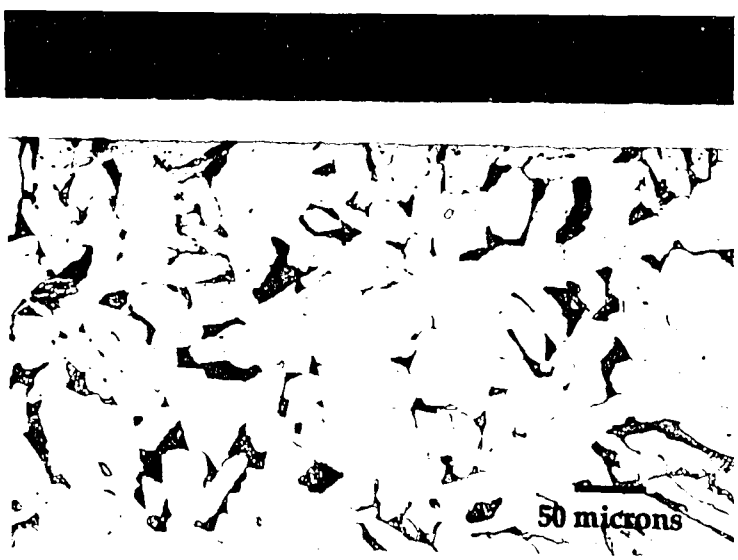

Figure 25. Cross-sectional light optical micrograph of ABCD plate on top of non-decarburized substrate (200x)

Figure 24. Cross-sectional light optical micrograph of ABCD plate on top of decarburized substrate (100x)

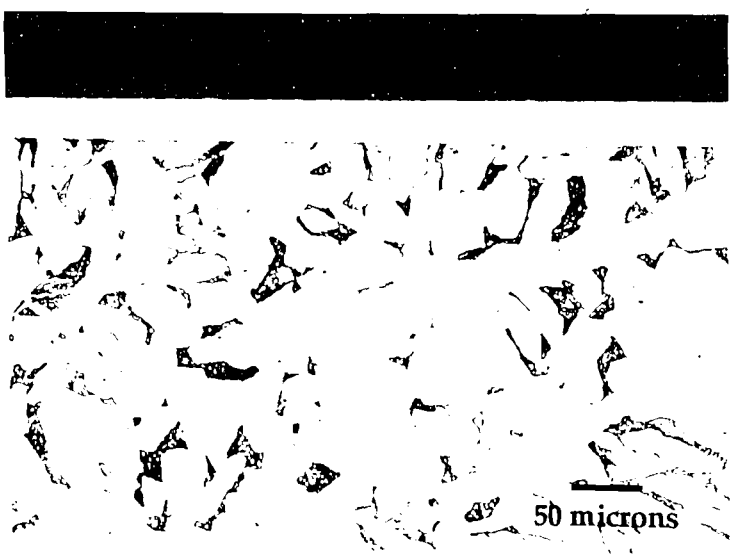

Figure 25. Cross-sectional light optical micrograph of ABCD plate on top of non-decarburized substrate (200x)

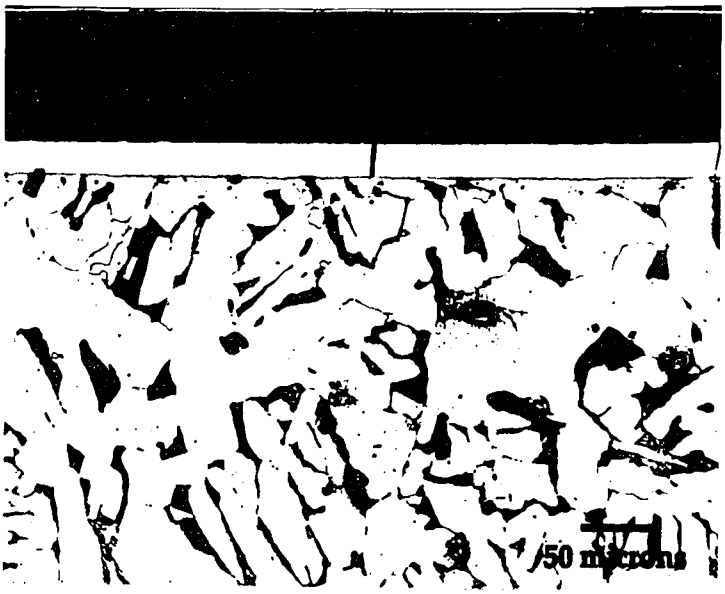

Figure 26. Cross-sectional light optical micrograph of macrocrack in ABCD plate (200x)

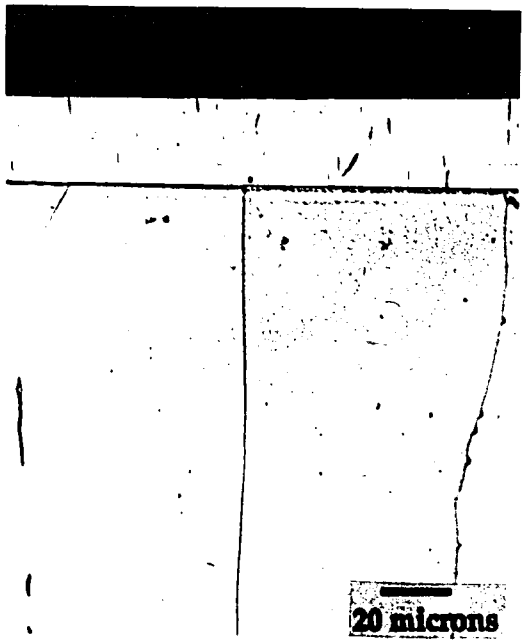

Figure 27. Cross-sectional light optical micrograph of microcracks in conventional chromium plate (500x) (Agarwal, 1993)

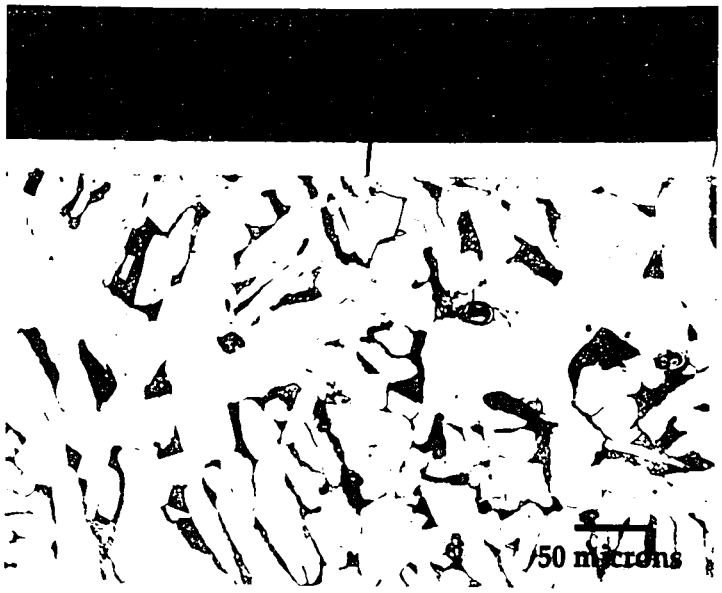

Figure 26. Cross-sectional light optical micrograph of macrocrack in ABCD plate (200x)

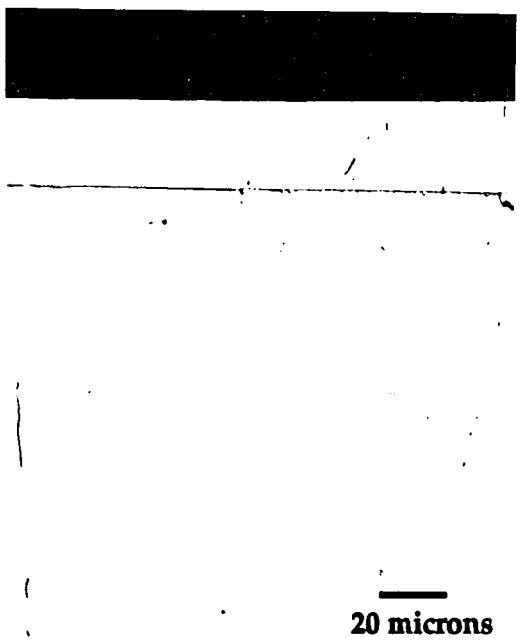

Figure 27. Cross-sectional light optical micrograph of microcracks in conventional chromium plate (500x) (Agarwal, 1993)

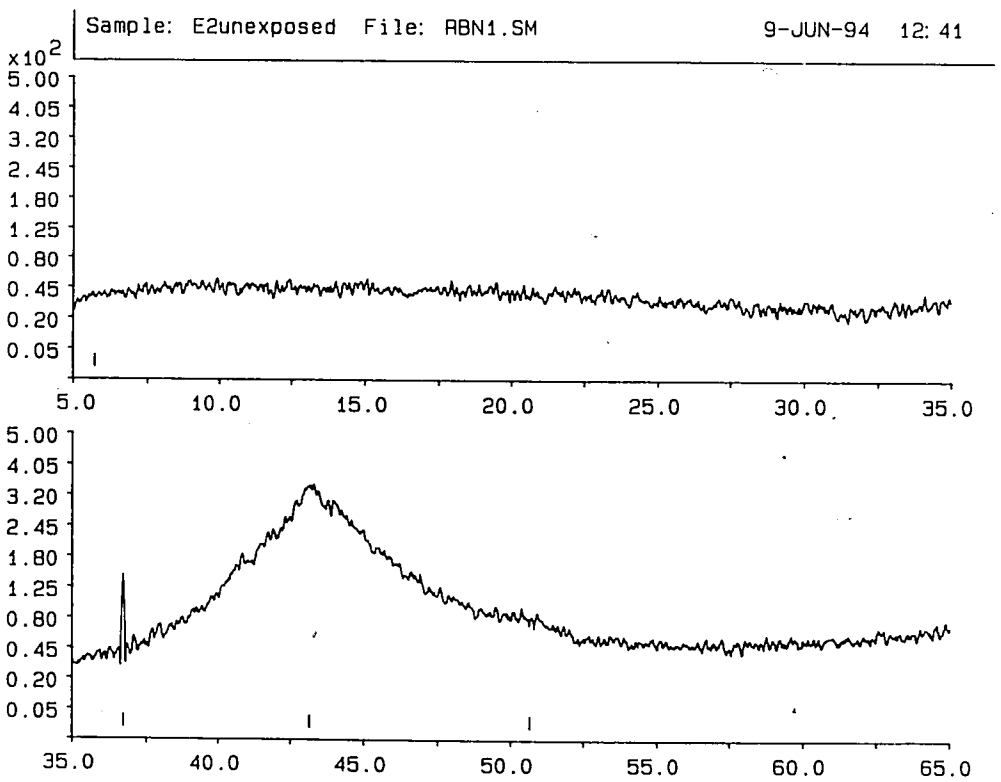

Figure 28a. X-ray diffraction pattern of as-plated ABCD coating

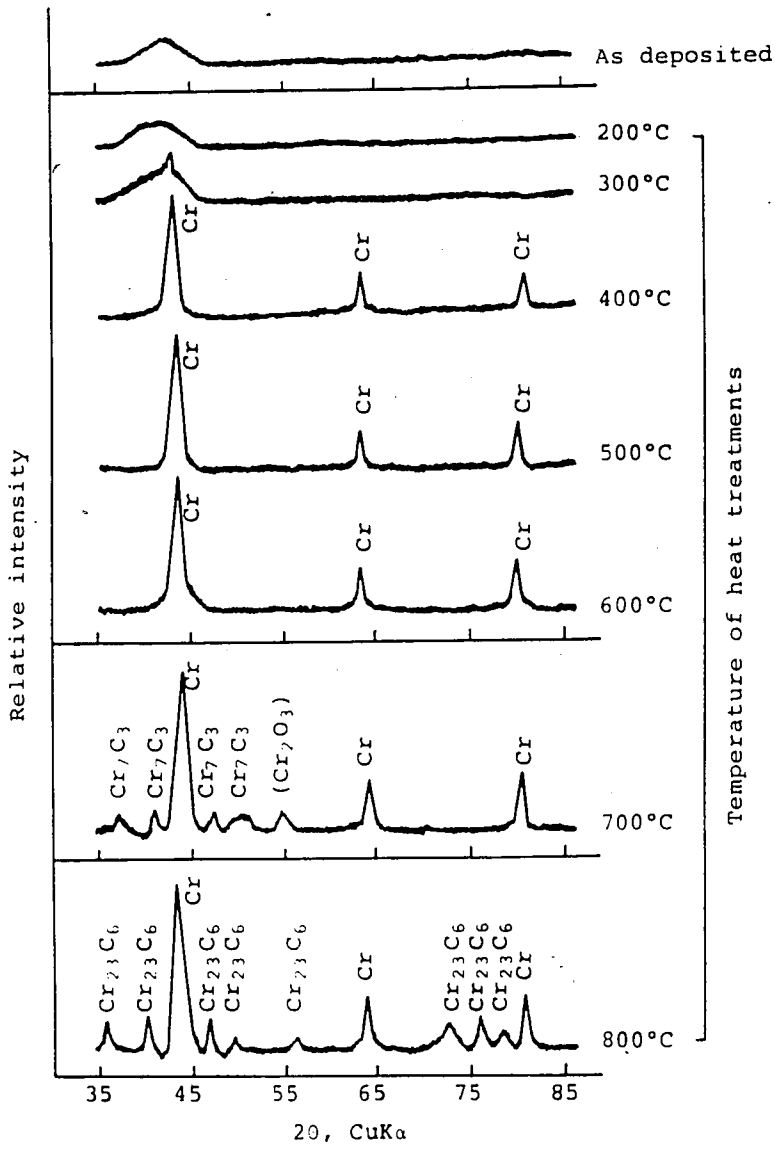

Figure 28b. X-ray diffraction pattern of as-plated ABCD coating as observed by Hoshino et al. (1986)

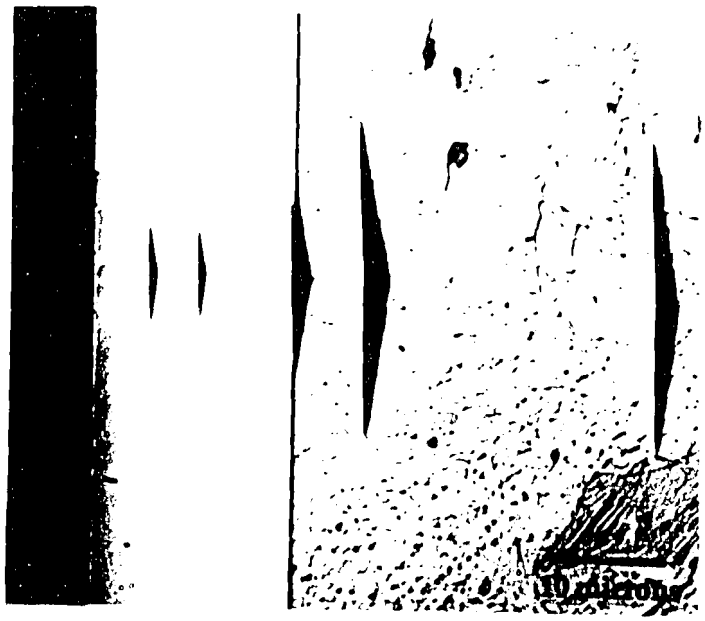

Figure 29a. Cross-sectional light optical micrograph of representative trace of Knoop indentations across as-plated coating (1500x)

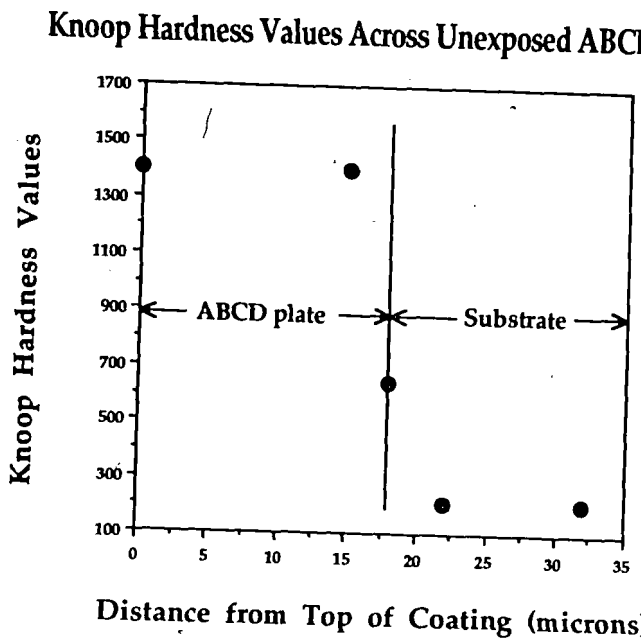

Figure 29b. Knoop hardness values obtained from cross sectional trace of as-plated ABCD coating

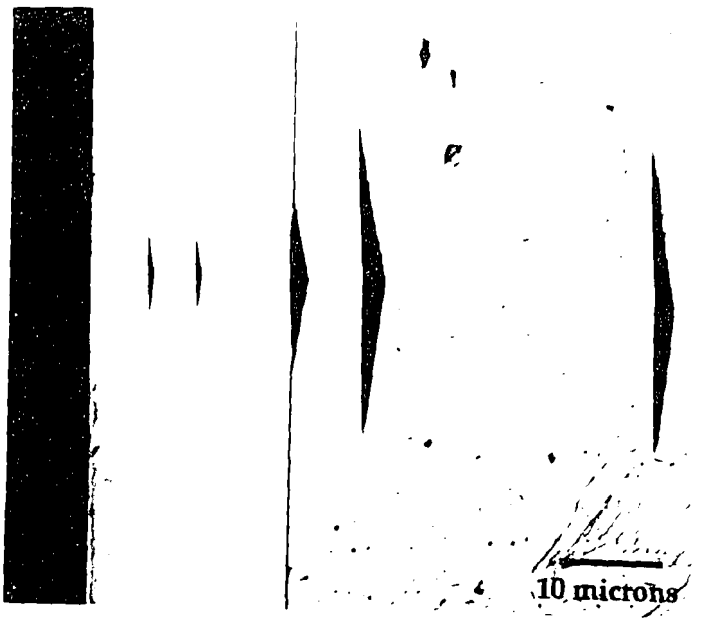

Figure 29a. Cross-sectional light optical micrograph of representative trace of Knoop indentations across as-plated coating (1500x)

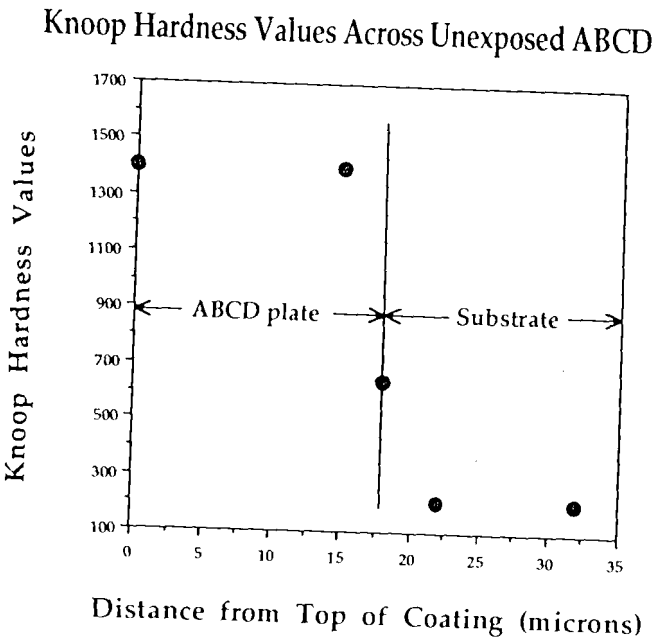

Figure 29b. Knoop hardness values obtained from cross sectional trace of as-plated ABCD coating

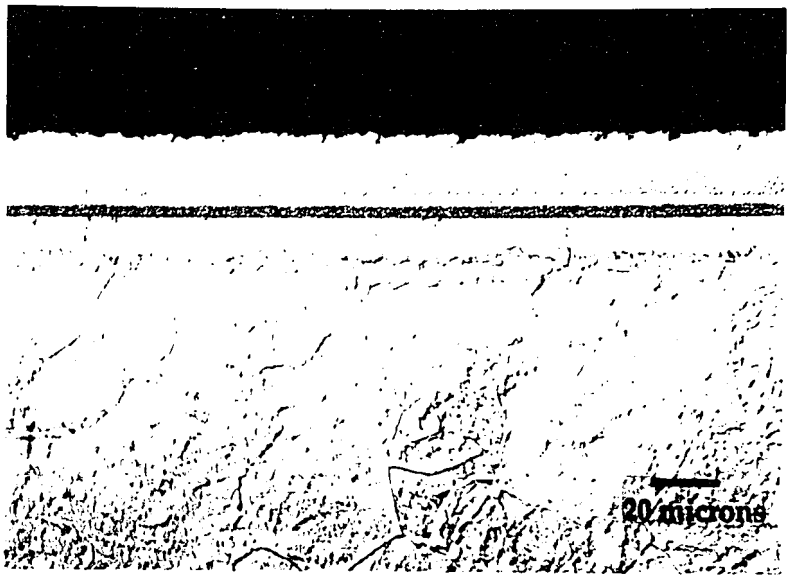

Figure 30a. Cross-sectional light optical micrograph of encapsulated sample after 200 hours of exposure. The sample was etched with Murakami's agent and viewed with a Nomarski filter (500x)

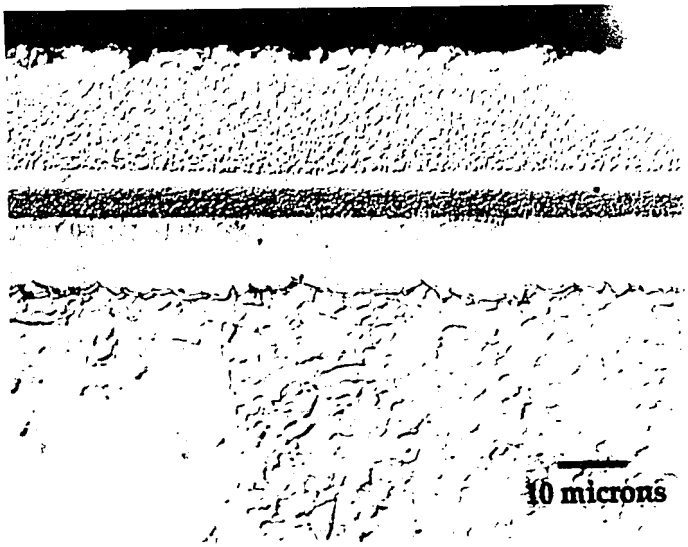

Figure 30b. Cross-sectional light optical micrograph of encapsulated sample after 200 hours of exposure. The sample was etched with Murakami's agent and viewed with a Nomarski filter (1000x)

20 microns

Figure 30a. Cross-sectional light optical micrograph of encapsulated sample after 200 hours of exposure. The sample was etched with Murakami's agent and viewed with a Nomarski filter (500x)

10 microns

Figure 30b. Cross-sectional light optical micrograph of encapsulated sample after 200 hours of exposure. The sample was etched with Murakami's agent and viewed with a Nomarski filter (1000x)

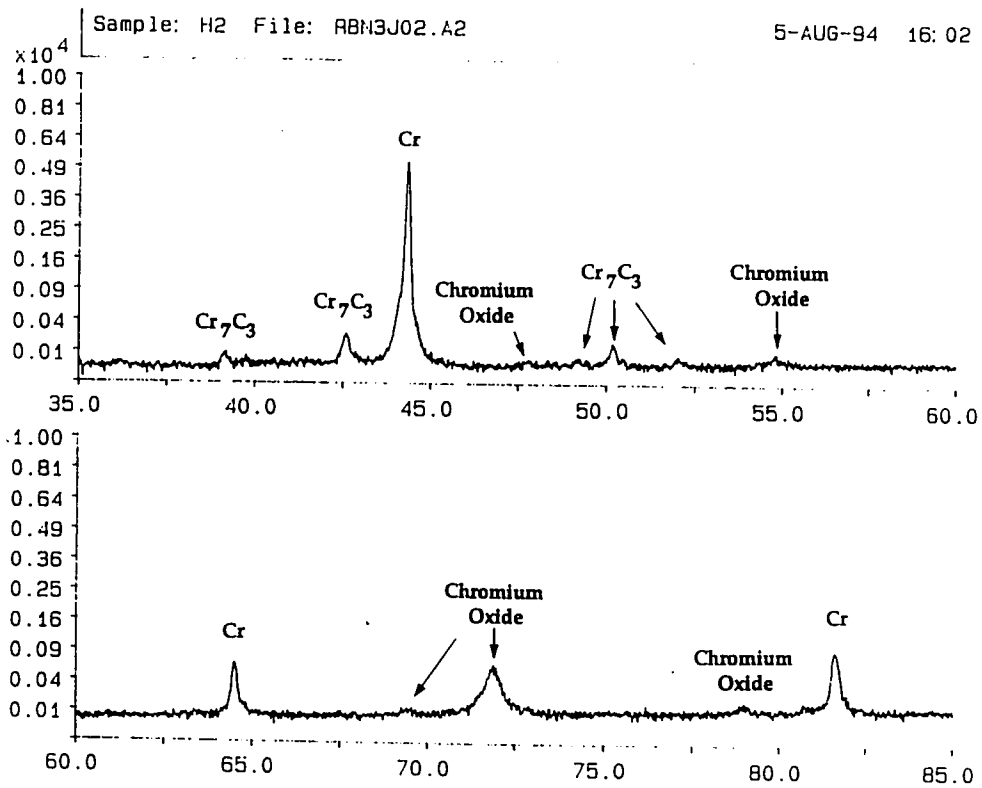

Figure 31a. X-ray diffraction pattern of ABCD coating after 1 hour of exposure at 700°C

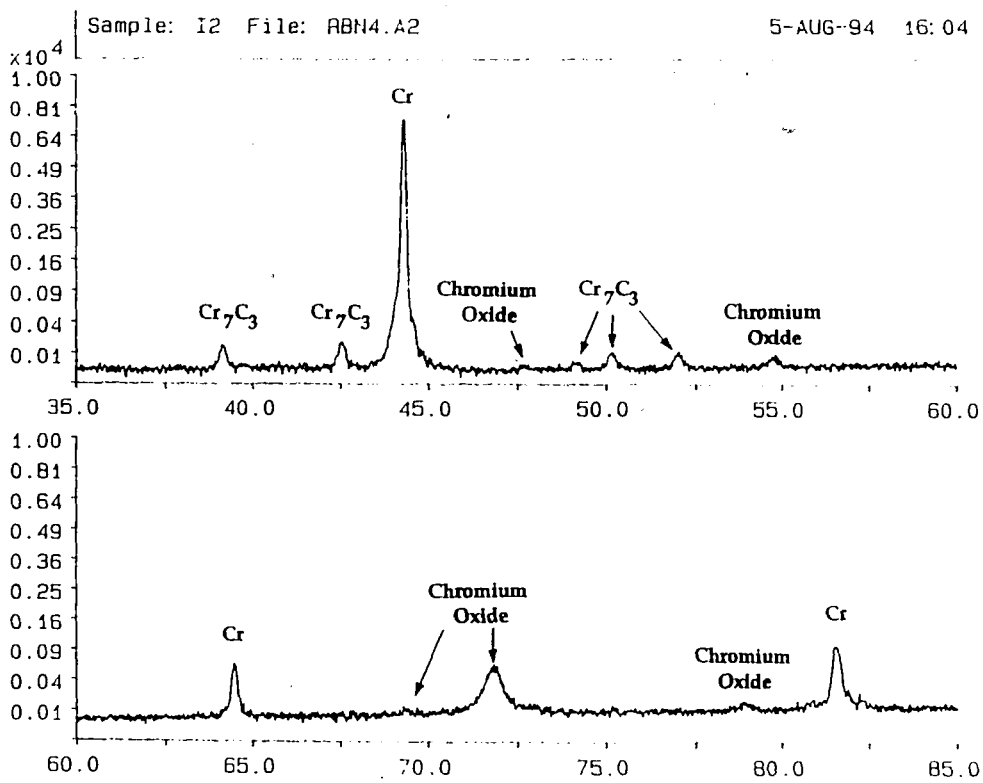

Figure 31b. X-ray diffraction pattern of ABCD coating after 5 hours of exposure at 700°C

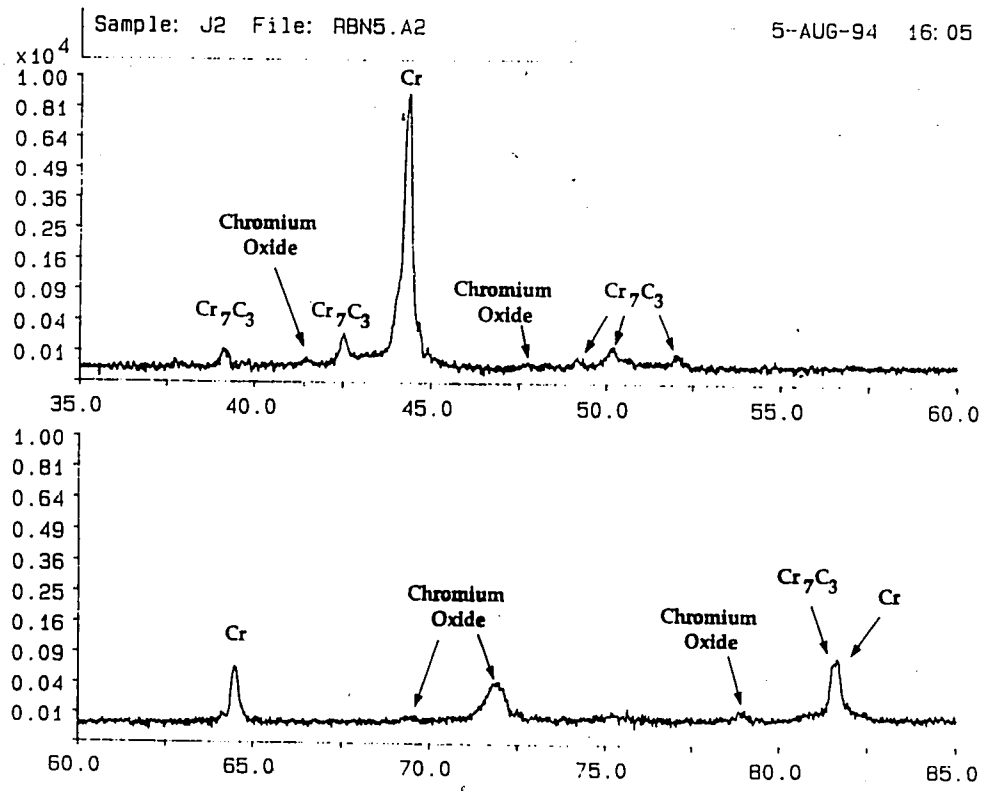

Figure 31c. X-ray diffraction pattern of ABCD coating after 22 hours of exposure at 700°C

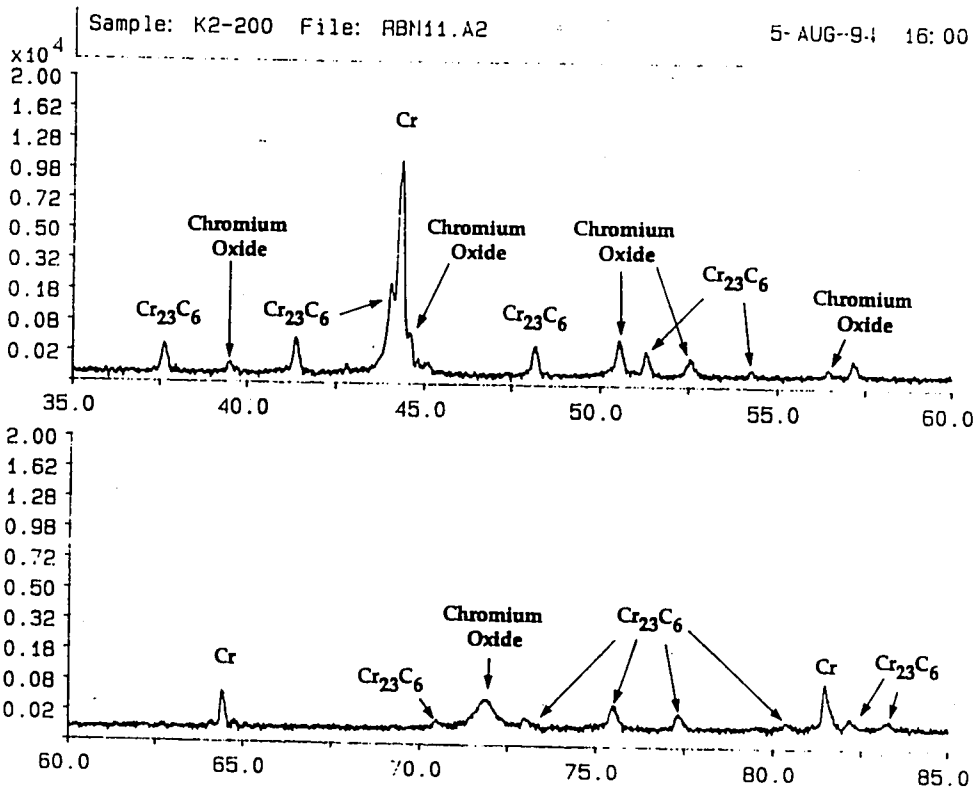

Figure 31d. X-ray diffraction pattern of ABCD coating after 200 hours of exposure at 700°C

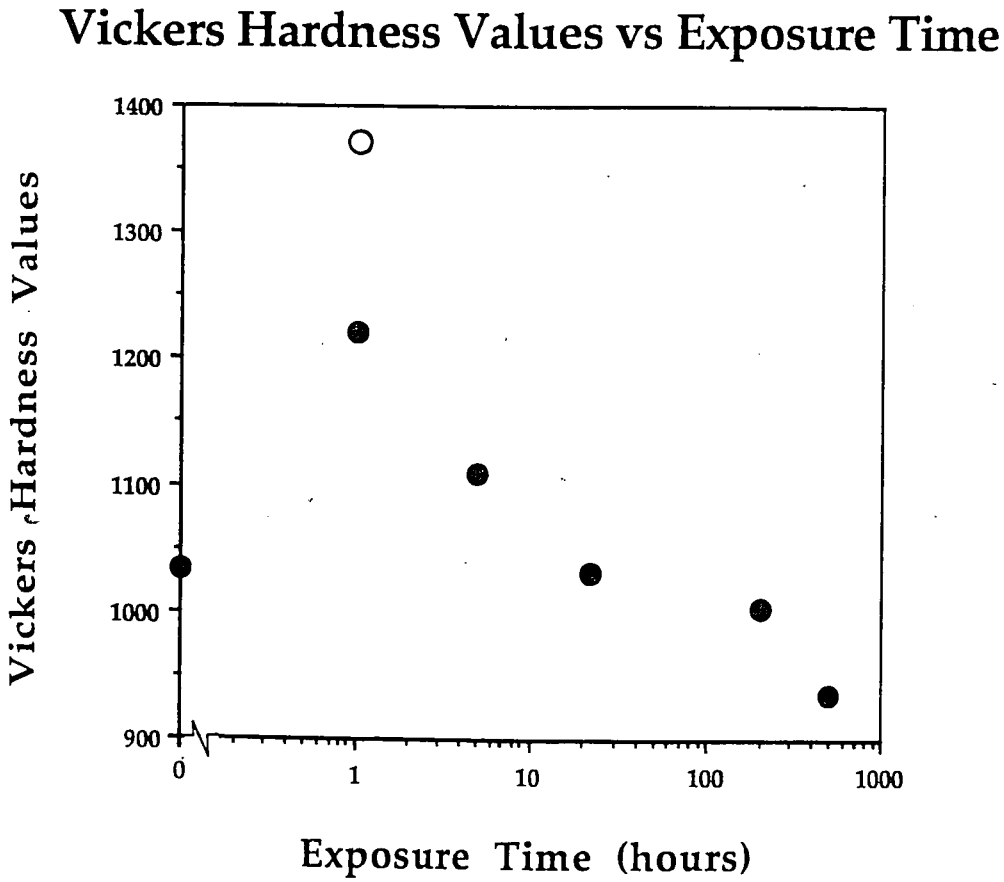

Figure 32. Vickers hardness values as a function of exposure time. The temperature of exposure was 700°C. The open circle represents the value measured by Hoshino et al (1986)

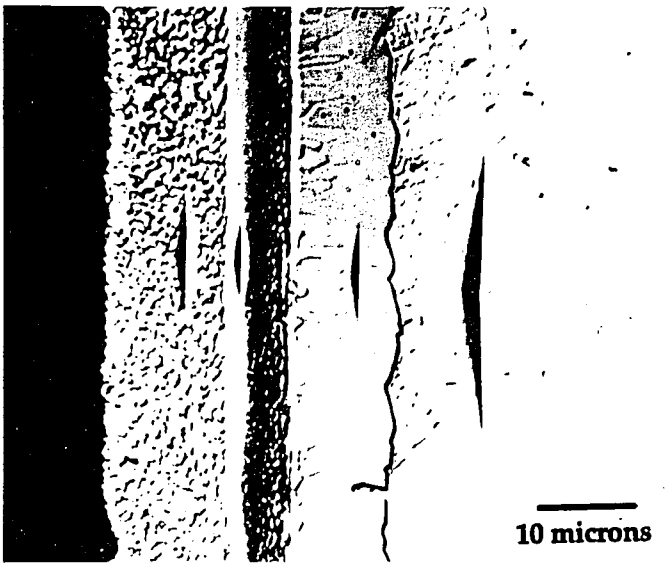

Figure 33a. Cross-sectional light optical micrograph of representative trace of Knoop indentations across exposed coating. The coating was exposed for 200 hours at 700°C (1500x)

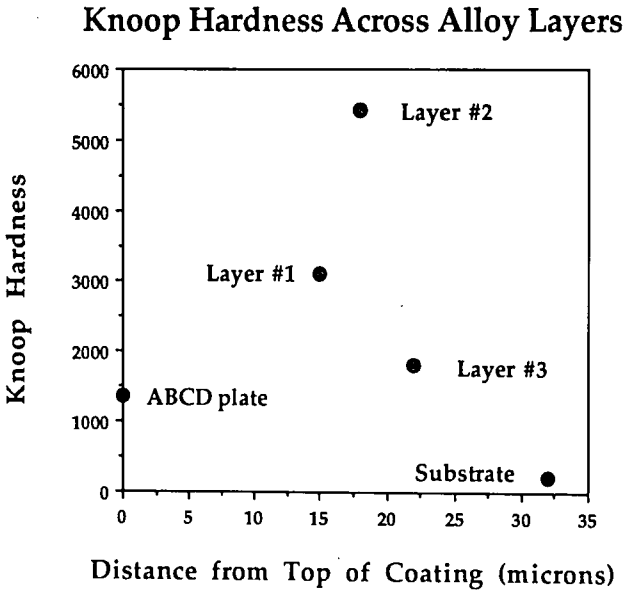

Figure 33b. Knoop hardness values obtained from cross sectional trace of exposed ABCD coating

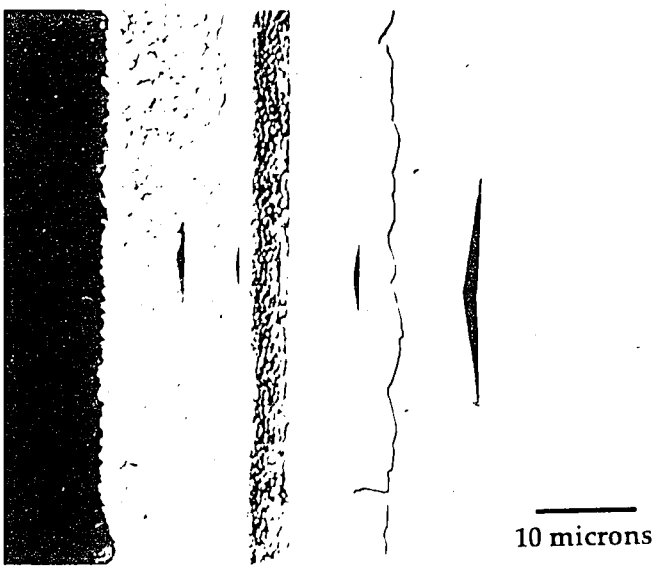

Figure 33a. Cross-sectional light optical micrograph of representative trace of Knoop indentations across exposed coating. The coating was exposed for 200 hours at 700°C (1500x)

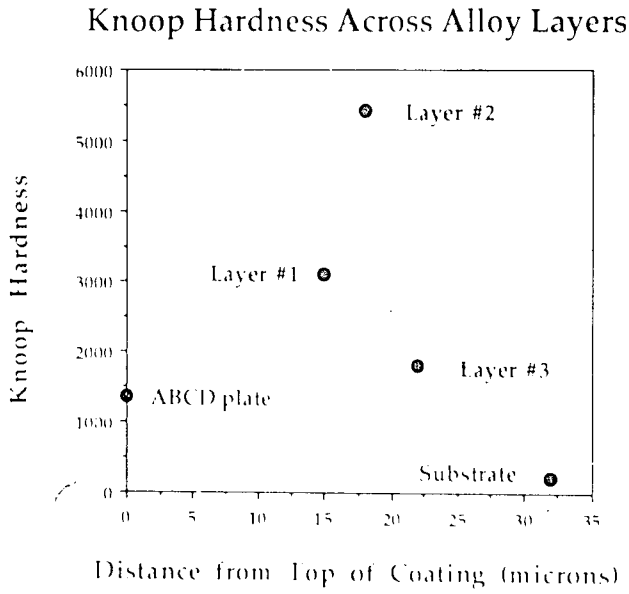

Figure 33b. Knoop hardness values obtained from cross sectional trace of exposed ABCD coating

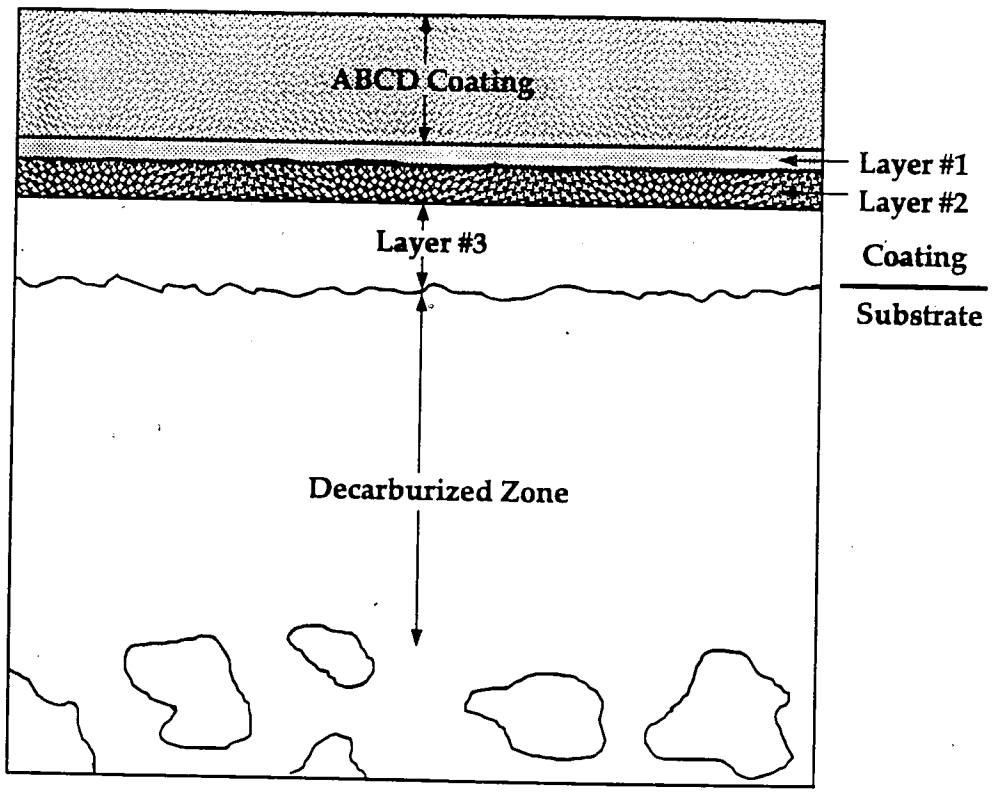

Figure 34. Schematic diagram of alloy layers that form upon exposure of ABCD plate

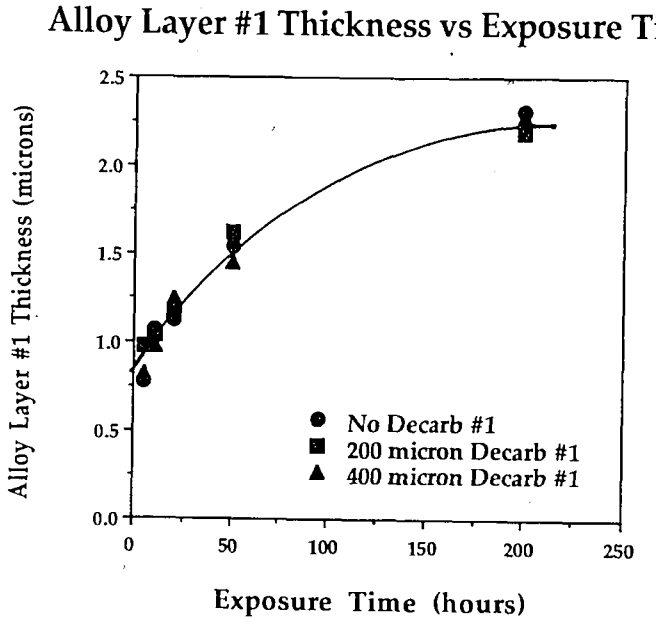

Figure 35a. Thickness of alloy layer #1 versus exposure time

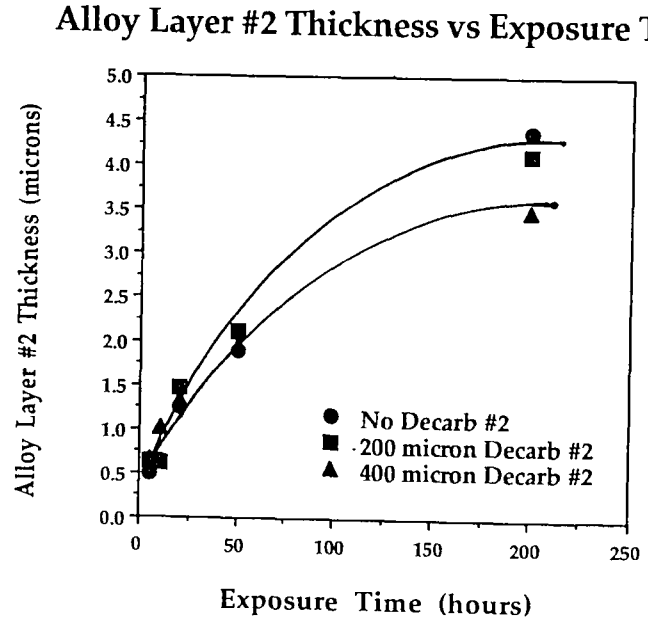

Figure 35b. Thickness of alloy layer #2 versus exposure time

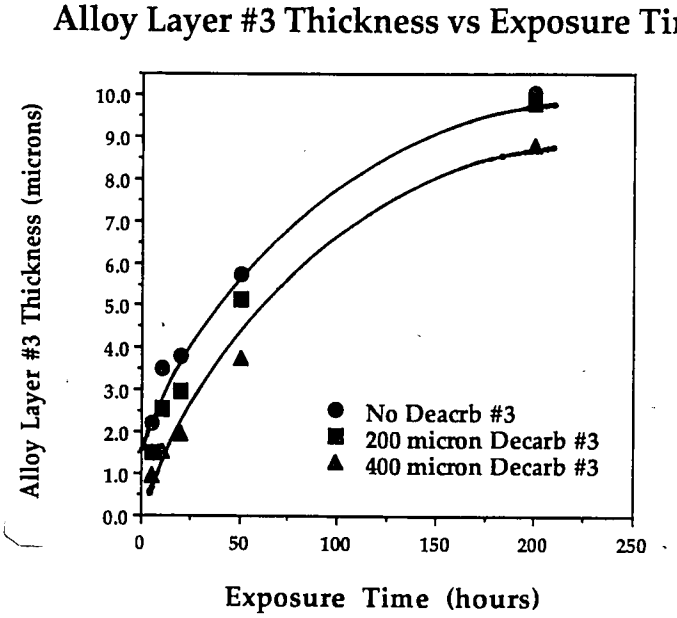

Figure 35c. Thickness of alloy layer #3 versus exposure time

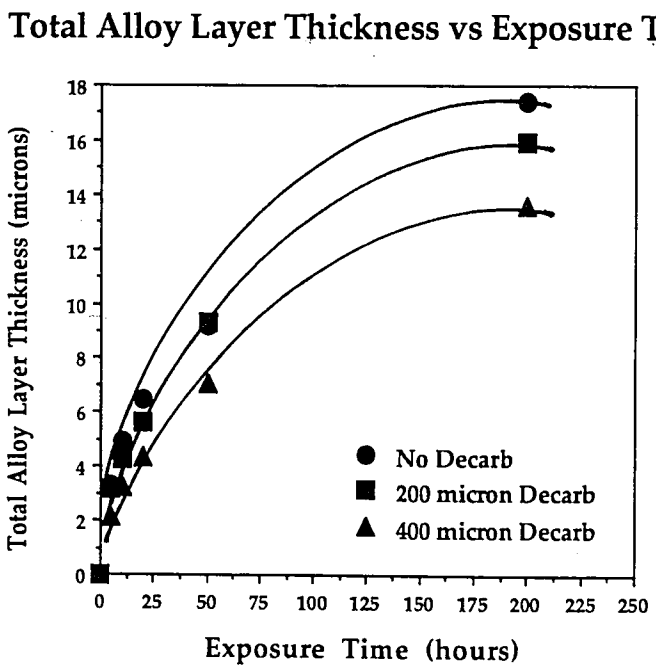

Figure 35d. Thickness of total alloy layer versus exposure time

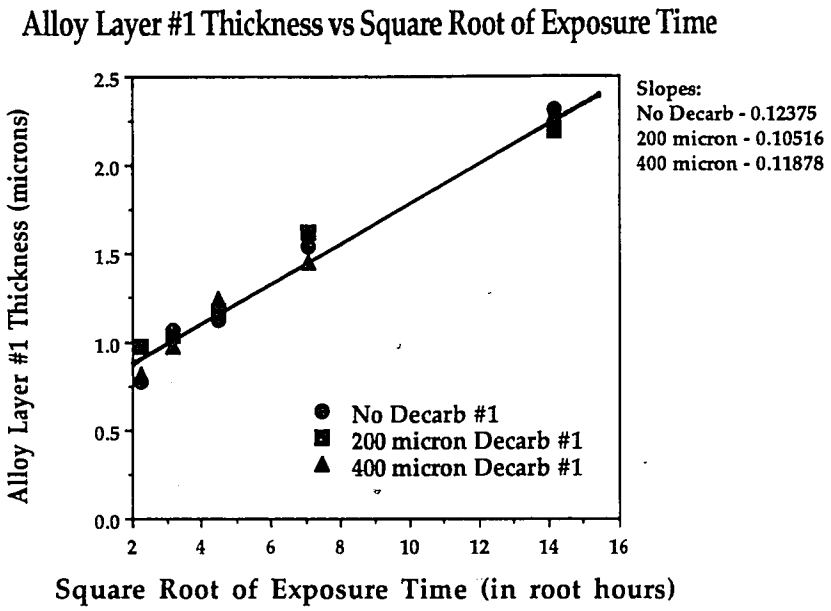

Figure 36a. Thickness of alloy layer #1 versus the square root of exposure time

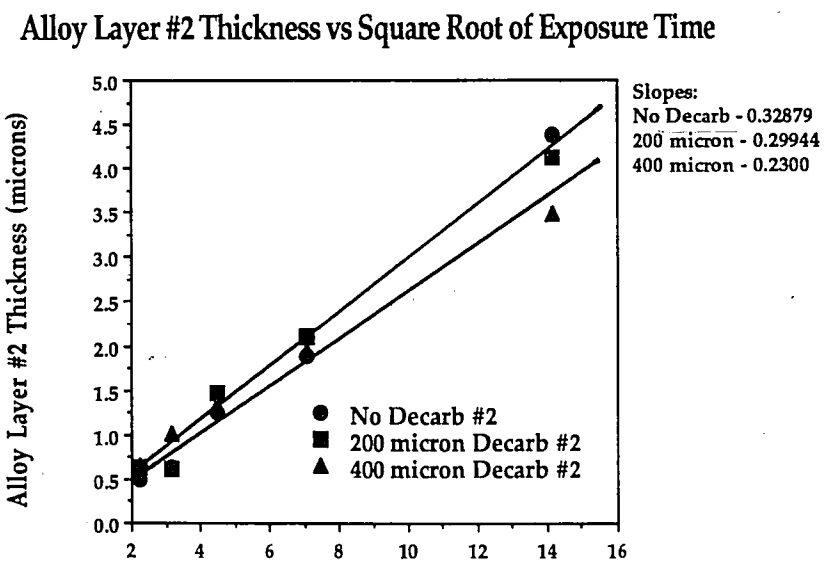

Figure 36b. Thickness of alloy layer #2 versus the square root of exposure time

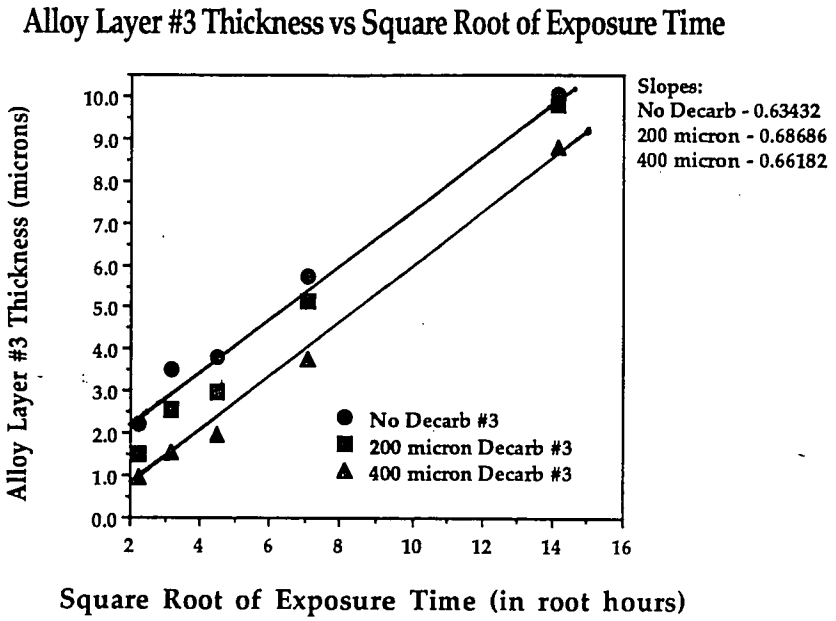

Figure 36c. Thickness of alloy layer #3 versus the square root of exposure time

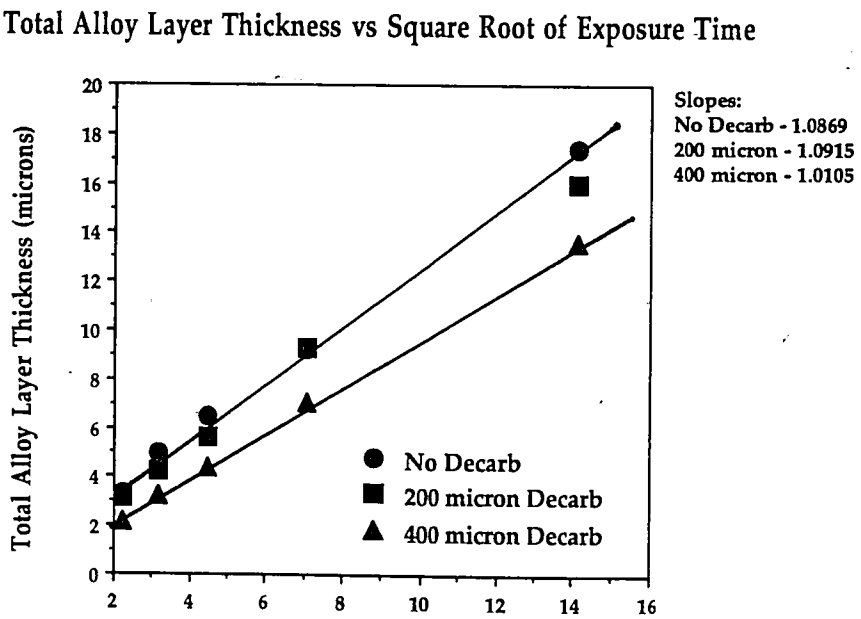

Figure 36d. Thickness of total alloy layer versus the square root of exposure time

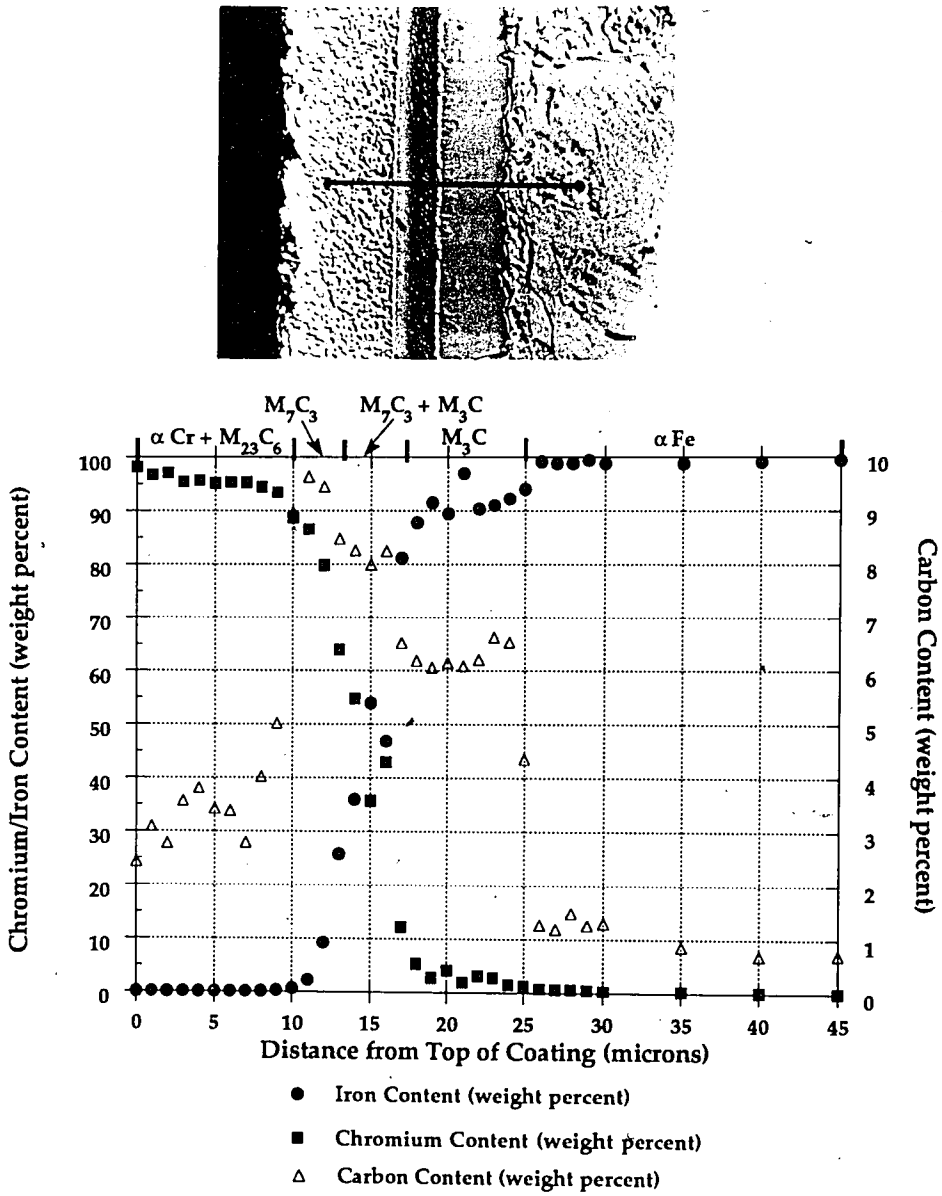

Figure 37. Compositional trace of ABCD coating on non-decarburized substrate after 200 hours of exposure at 700°C according to the Bastin PROZA Phi(ρz) correction scheme. The micrograph represents the probe trace through the alloy layers

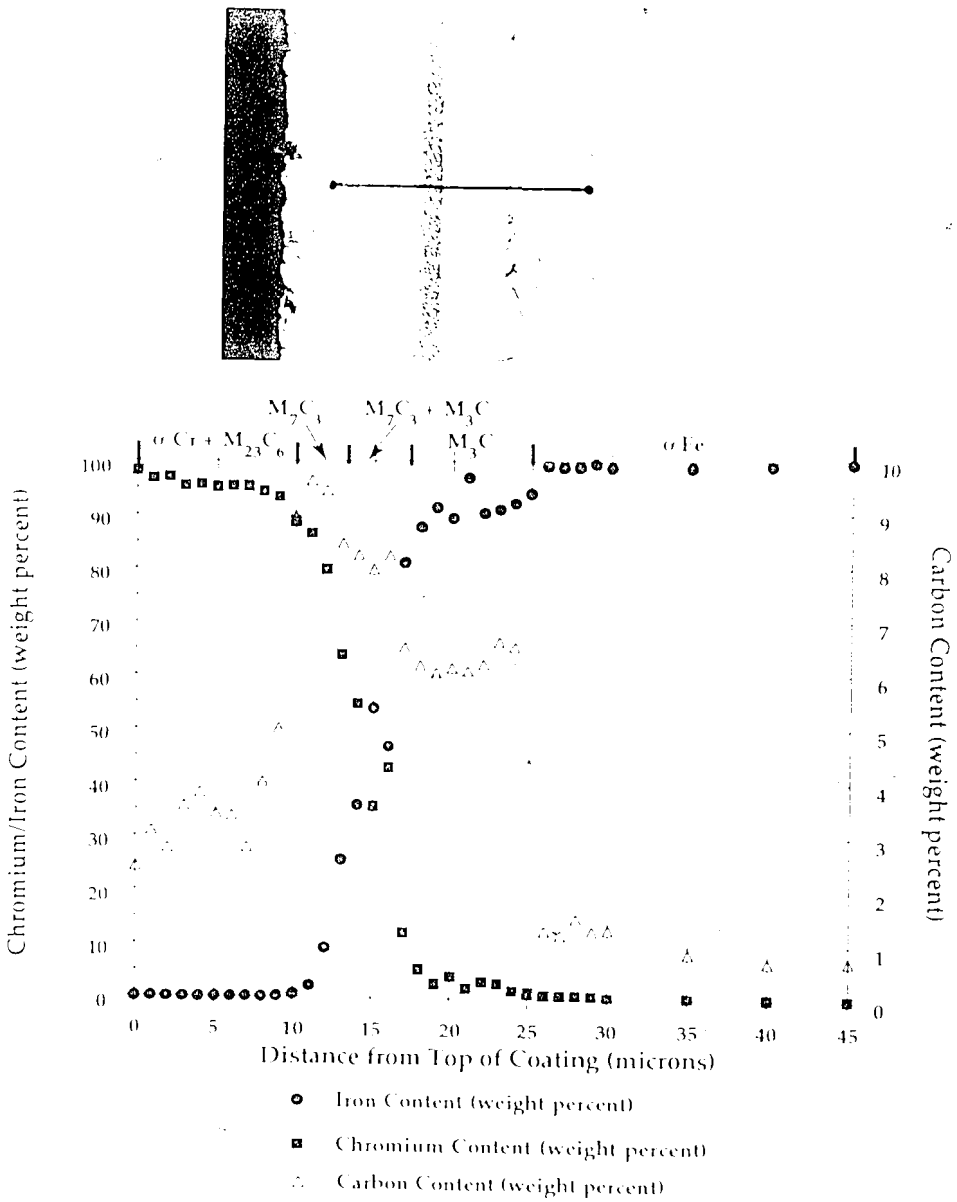

Figure 37. Compositional trace of ABCD coating on non-decarburized substrate after 200 hours of exposure at 700°C according to the Bastin PROZA Phi(ρz) correction scheme. The micrograph represents the probe trace through the alloy layers

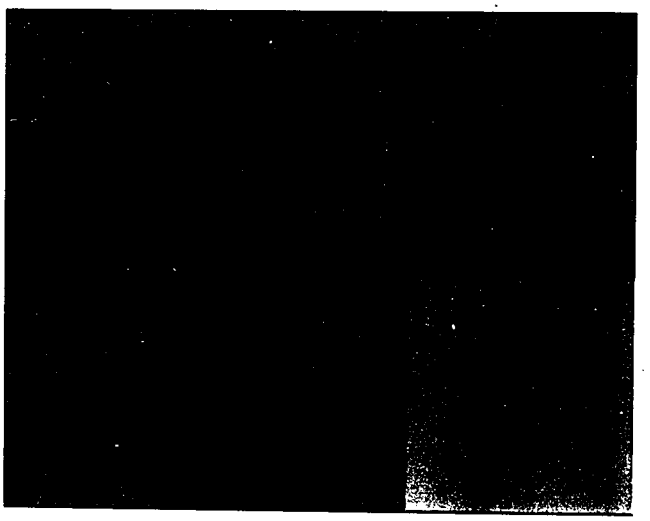

Figure 38. Elemental dot (WDS) maps of analyzed region. *Top Left*: Iron map; *Top Right*: Chromium map; Bottom Left: Carbon map; *Bottom Right*: Secondary image of region

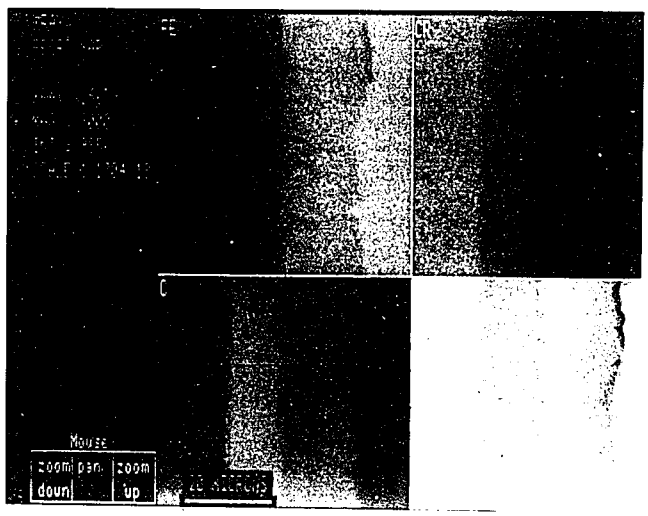

Figure 38. Elemental dot (WDS) maps of analyzed region. *Top Left*: Iron map; *Top Right*: Chromium map; Bottom Left: Carbon map; *Bottom Right*: Secondary image of region

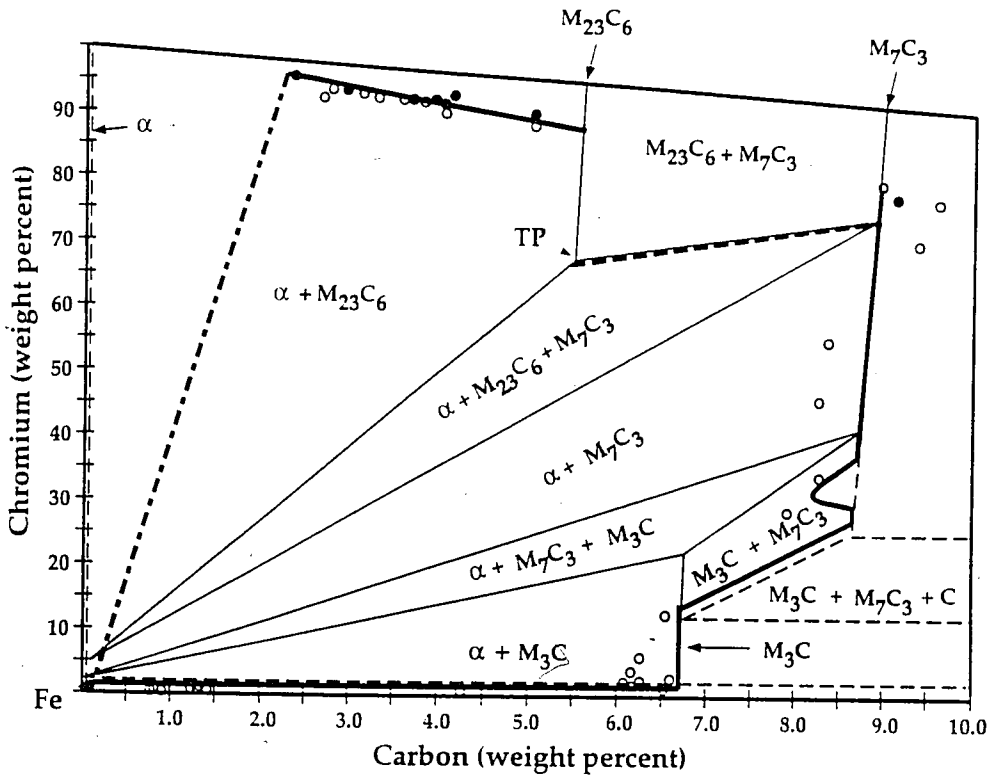

Figure 39. 700°C isotherm of iron-chromium-carbon ternary phase diagram (Rivlin, 1984) with actual compositional points and proposed diffusion path. The open circles are from the trace on the 200 hour sample and the closed circles are from the 500 hour sample.

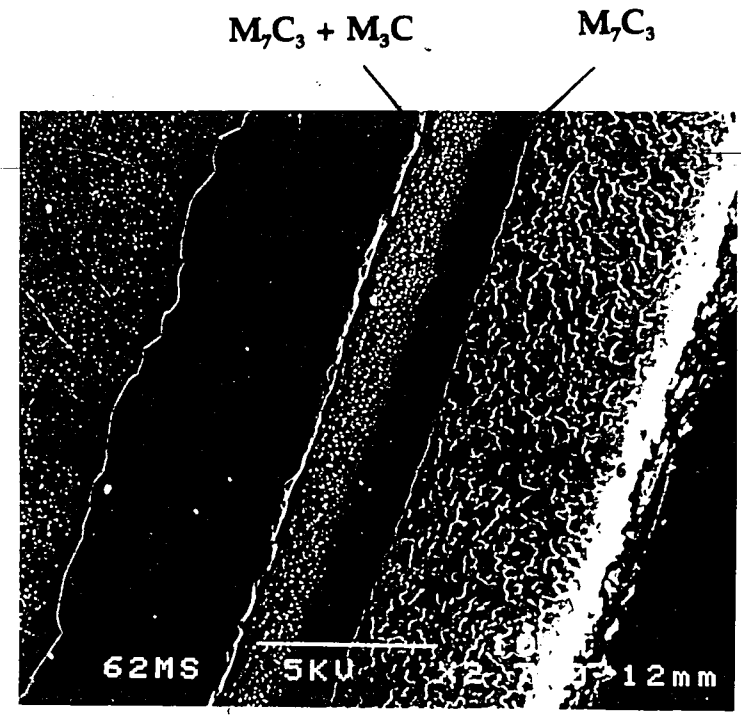

Figure 40. SEM micrograph of the diffusion zone in an non-decarburized sample after 200 hours of exposure at 700°C. The sample was etched with Murakami's agent (2700x)

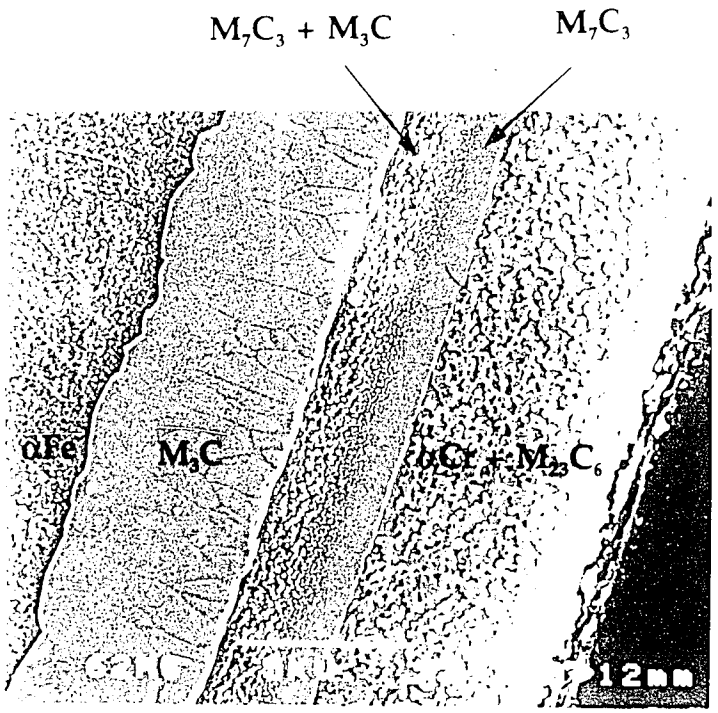

Figure 40. SEM micrograph of the diffusion zone in an non-decarburized sample after 200 hours of exposure at 700°C. The sample was etched with Murakami's agent (2700x)

Figure 41. Backscattered SEM micrograph of diffusion zone in an non-decarburized sample after 200 hours of exposure at 700°C. The sample is in the as-polished condition.

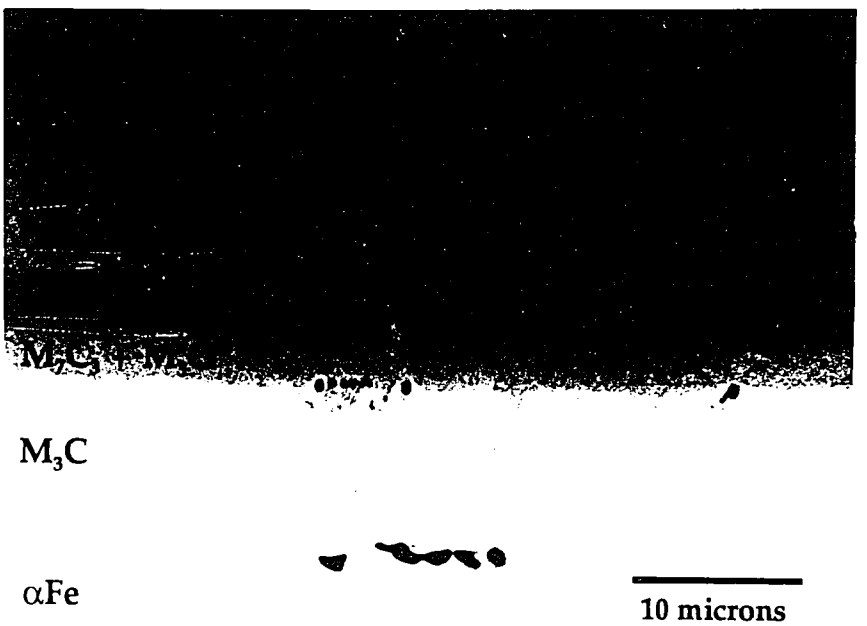

Figure 41. Backscattered SEM micrograph of diffusion zone in an non-decarburized sample after 200 hours of exposure at 700°C. The sample is in the as-polished condition.

Figure 42. Backscattered SEM micrograph of ABCD plate after 200 hours of exposure at 700°C. Two distinct phases are apparent -- a relatively heavy atomic species (light regions) in a light matrix (dark matrix) (5000x)

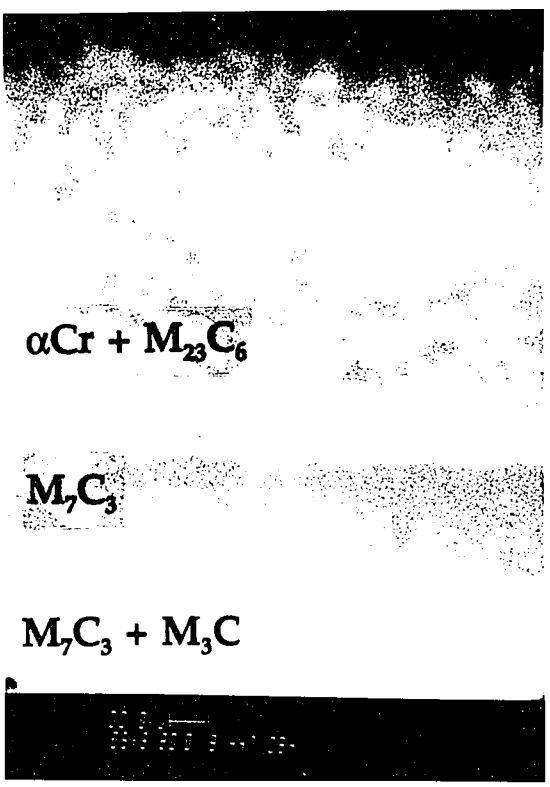

Figure 42. Backscattered SEM micrograph of ABCD plate after 200 hours of exposure at 700°C. Two distinct phases are apparent -- a relatively heavy atomic species (light regions) in a light matrix (dark matrix) (5000x)

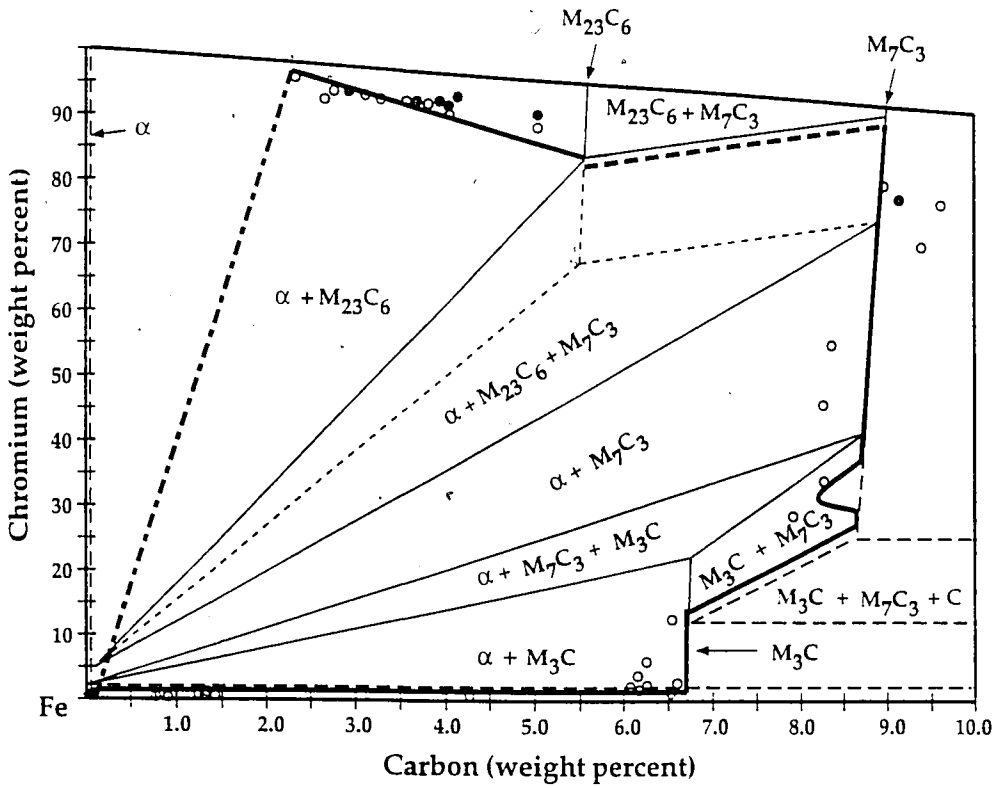

Figure 43. 700°C isotherm of iron-chromium-carbon phase diagram with proposed position of the triple point. The dotted lines indicate the "old" position of the triple point. The actual measured compositional values and diffusion path are also shown.

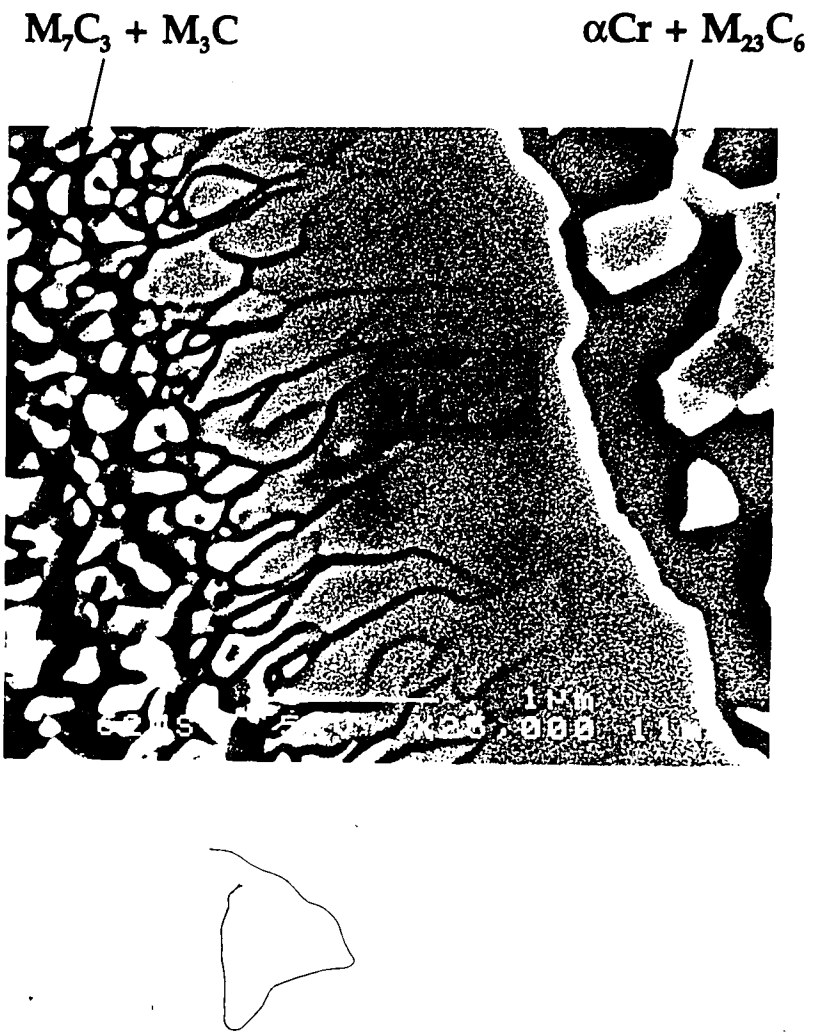

Figure 44. SEM micrograph of alloy layers #1 and #2. Layer #2 appears to precipitate out of layer #1. The needle-like morphology of layer #1 is typical of M_7C_3 layers (25000x)

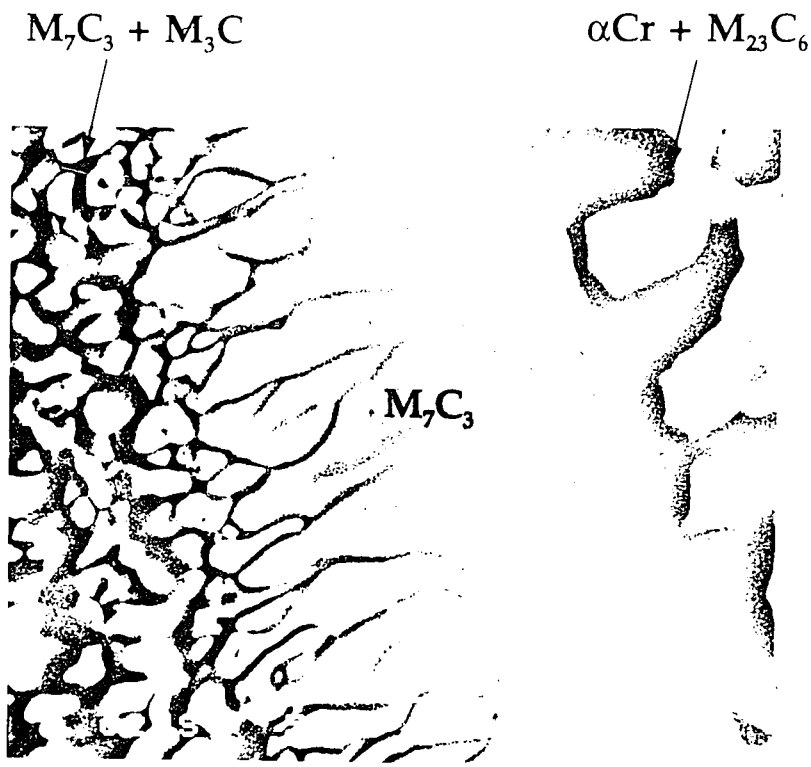

Figure 44. SEM micrograph of alloy layers #1 and #2. Layer #2 appears to precipitate out of layer #1. The needle-like morphology of layer #1 is typical of M_7C_3 layers (25000x)

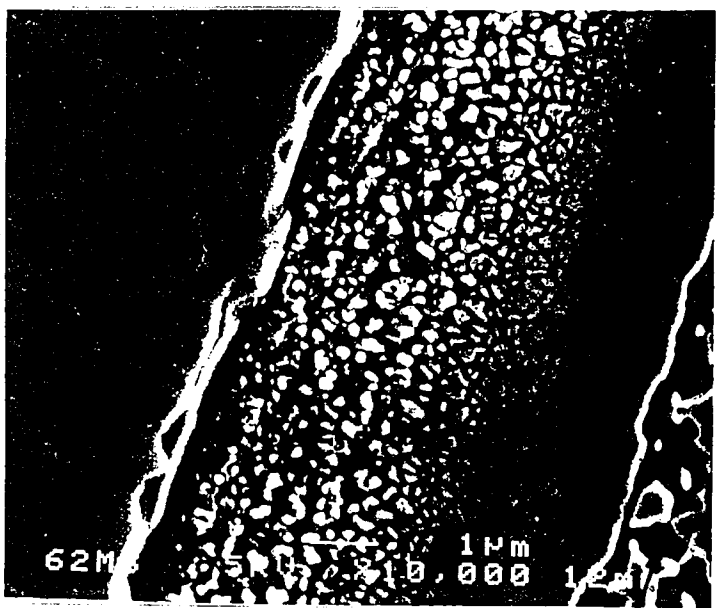

$\alpha Cr + M_{23}C_6$

Figure 45. SEM micrograph of the interface between layer #2 and layer #3. The two-phase nature of layer #2 and single-phase appearance of layer #3 is evident (10000x)

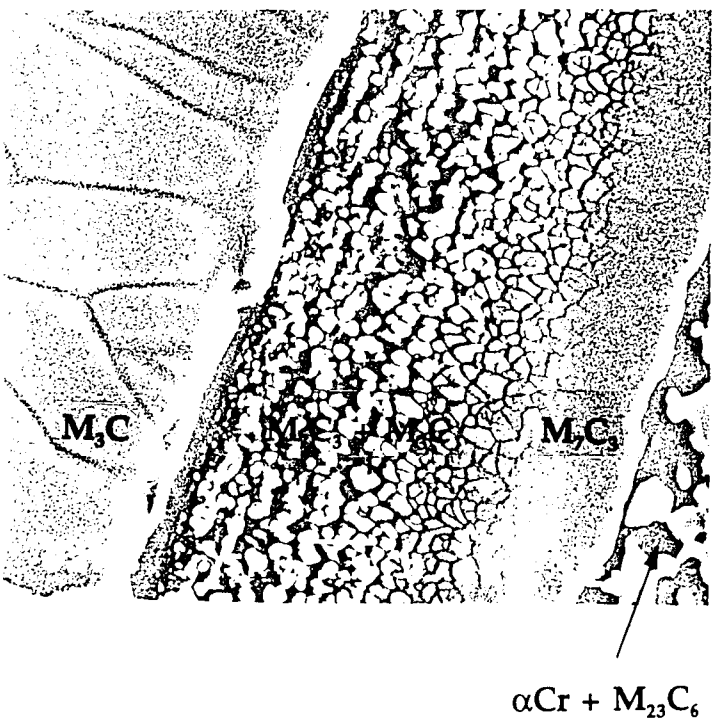

Figure 45. SEM micrograph of the interface between layer #2 and layer #3. The two-phase nature of layer #2 and single-phase appearance of layer #3 is evident (10000x)

Figure 46. ABCD sample after 1200 hours of exposure at 700°C in an oxidizing environment

Figure 46. ABCD sample after 1200 hours of exposure at 700°C in an oxidizing environment

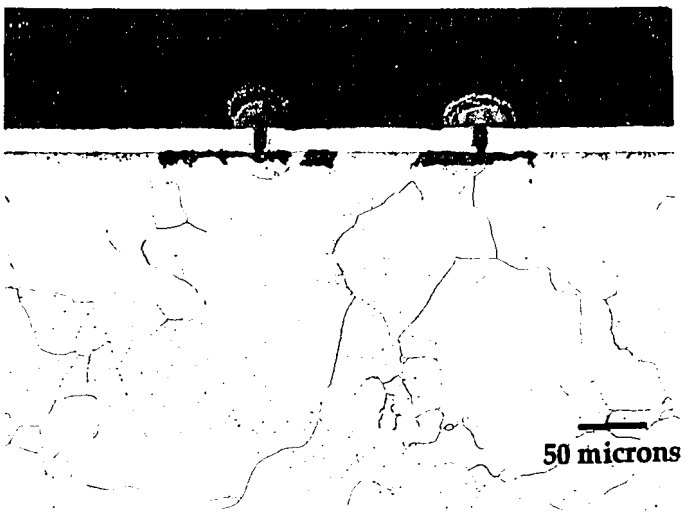

Figure 47a. Cross-sectional light optical micrograph of ABCD plate oxidized for 200 hours at 700°C (200x)

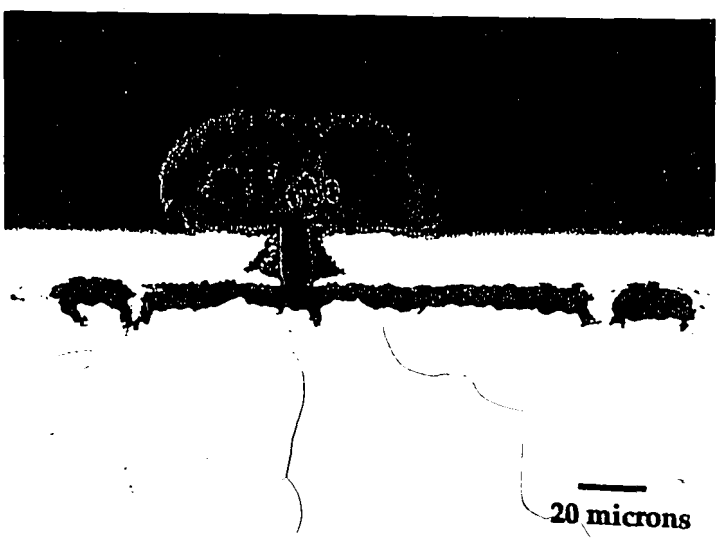

Figure 47b. Cross-sectional light optical micrograph of ABCD plate oxidized for 200 hours at 700°C (500x)

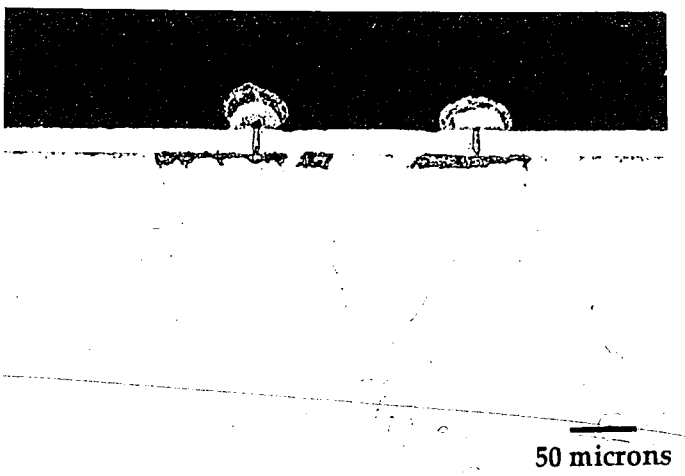

Figure 47a. Cross-sectional light optical micrograph of ABCD plate oxidized for 200 hours at 700°C (200x)

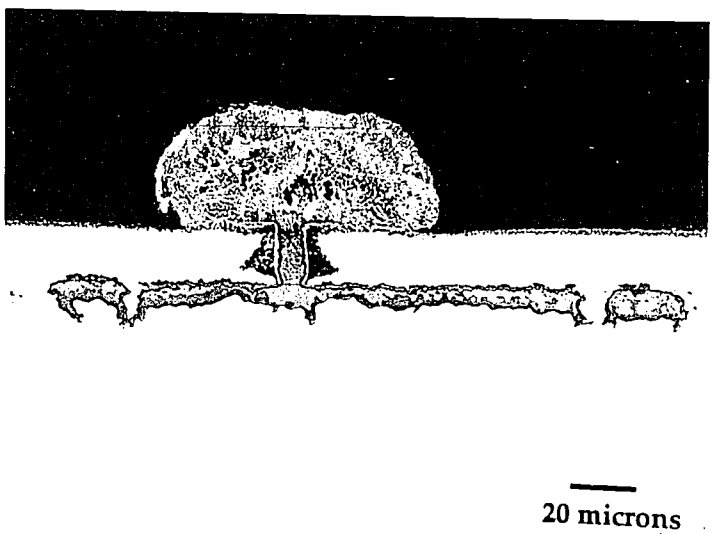

Figure 47b. Cross-sectional light optical micrograph of ABCD plate oxidized for 200 hours at 700°C (500x)

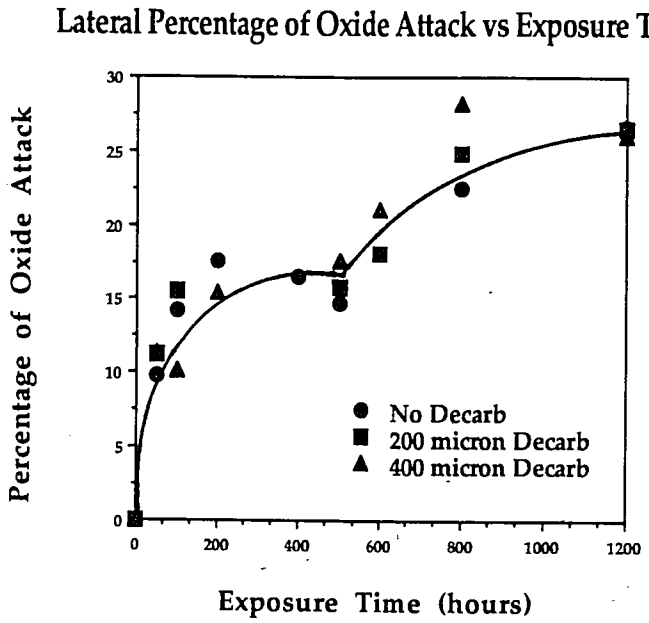

Figure 48. Lateral percentage of oxide attack as a function of exposure time

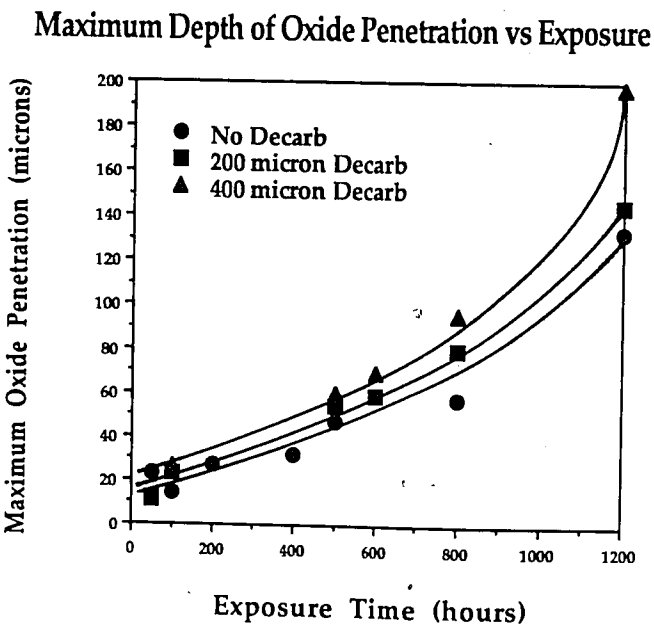

Figure 49. Maximum depth of oxide penetration as a function of exposure time

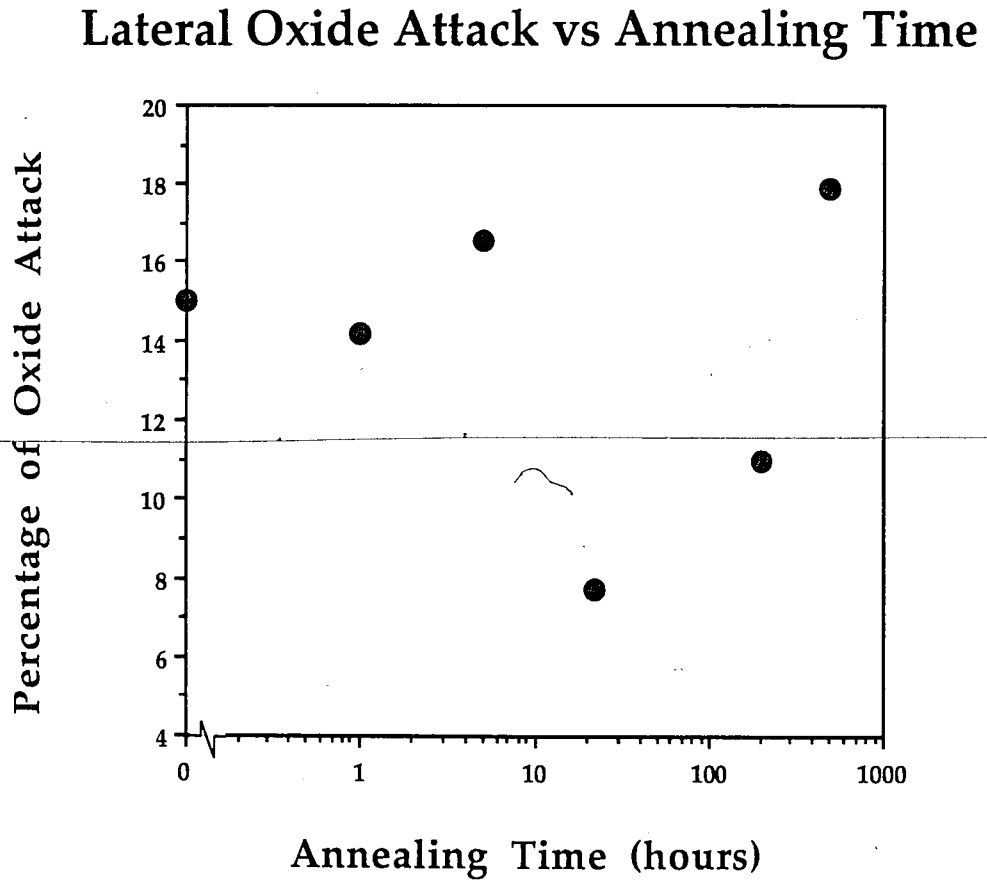

Figure 50. Lateral percentage of oxide attack versus the pre-anneal exposure time at 700°C. Each sample was exposed to an oxidizing atmosphere for 500 hours

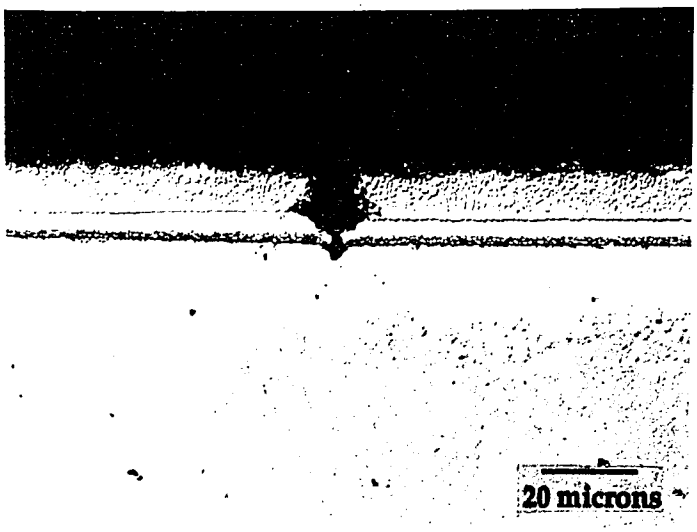

Figure 51. Cross-sectional light optical micrograph of unaffected macrocrack in the ABCD plate after 22 hour anneal and 500 hour oxidation at 700°C. The sample was etched with Murakami's agent and viewed with a Nomarski filter (500x)

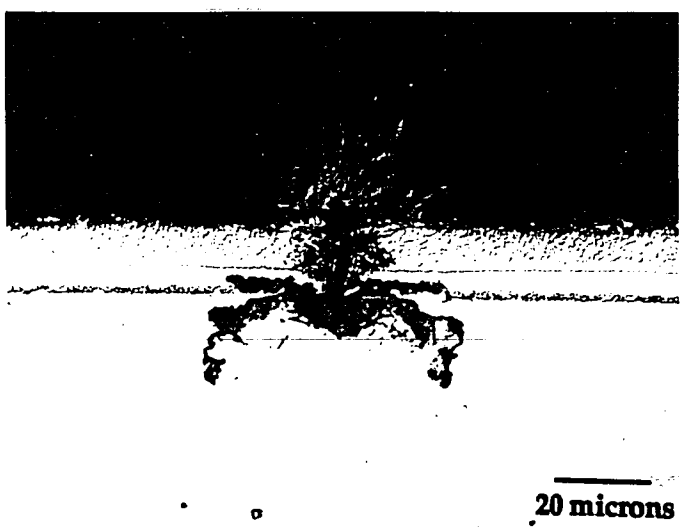

Figure 52. Cross-sectional light optical micrograph of oxide attack at a pre-existing macrocrack in the ABCD plate after 22 hour anneal and 500 hour oxidation at 700°C. The sample was etched with Murakami's agent and viewed with a Nomarski filter (500x)

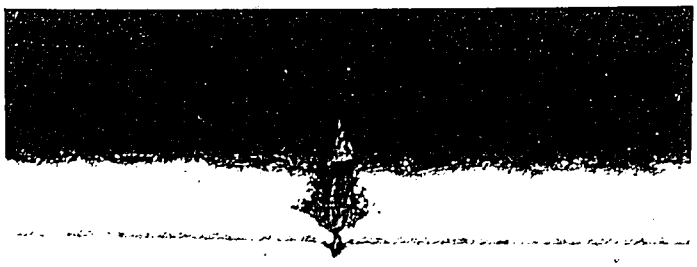

20 microns

Figure 51. Cross-sectional light optical micrograph of unaffected macrocrack in the ABCD plate after 22 hour anneal and 500 hour oxidation at 700°C. The sample was etched with Murakami's agent and viewed with a Nomarski filter. (500x)

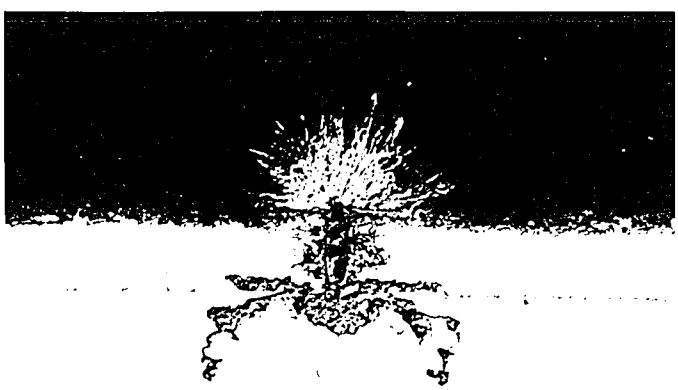

20 microns

Figure 52. Cross-sectional light optical micrograph of oxide attack at a pre-existing macrocrack in the ABCD plate after 22 hour anneal and 500 hour oxidation at 700°C. The sample was etched with Murakami's agent and viewed with a Nomarski filter (500x)

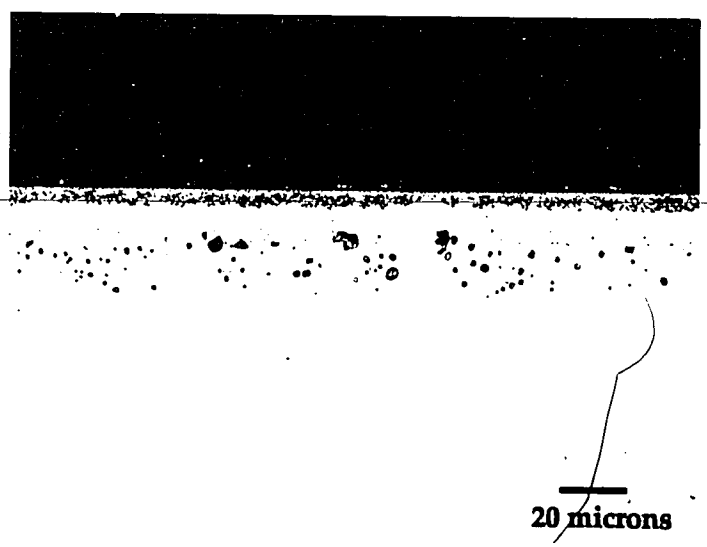

Figure 53. Cross-sectional light optical micrograph of spherical penetration of oxide at coating/substrate interface in ABCD plate after 500 hour anneal and 500 hour oxidation at 700°C (500x)

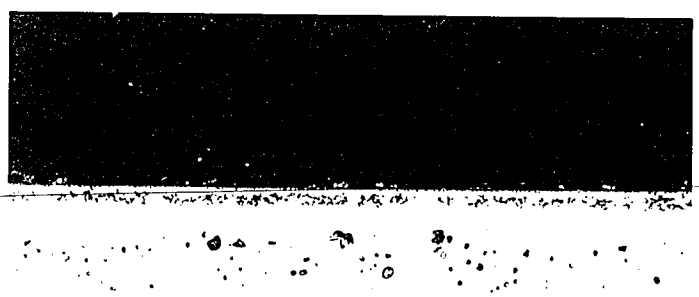

20 microns

Figure 53. Cross-sectional light optical micrograph of spherical penetration of oxide at coating/substrate interface in ABCD plate after 500 hour anneal and 500 hour oxidation at 700°C (500x)

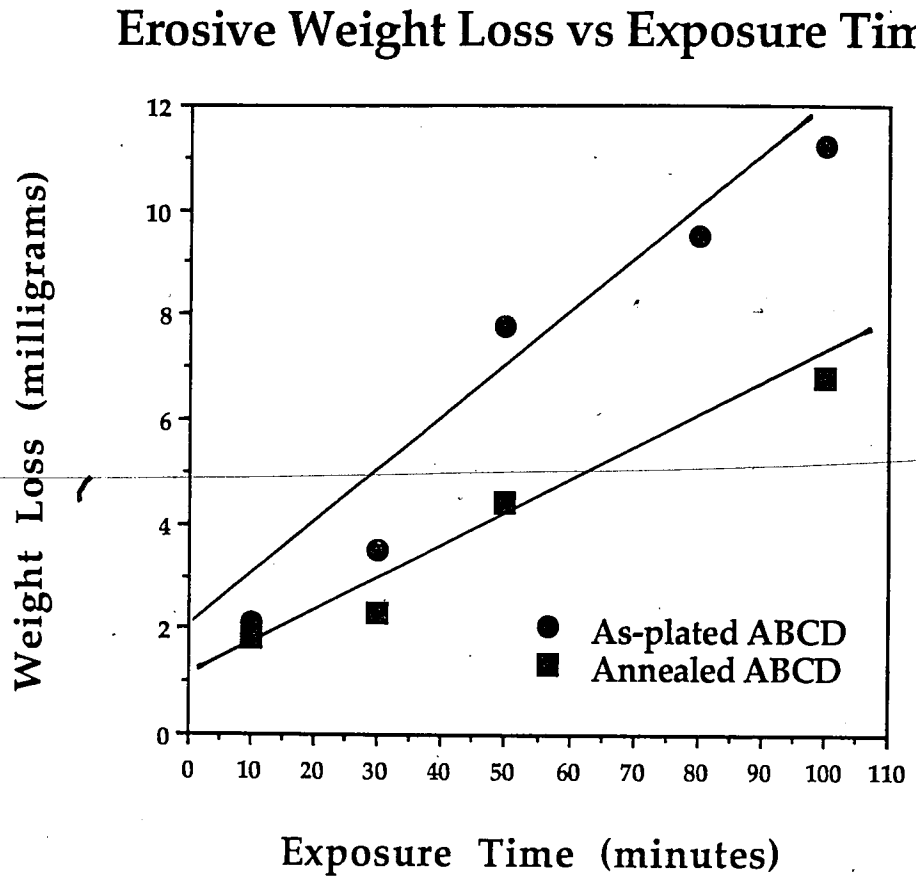

Figure 54. Erosion weight loss versus exposure time for as-plated and annealed ABCD plates

Table 1. Crystal structure data for the Iron-Carbon system (ASM, 1990)

Special Points of the Fe-C System

Reaction	Composition, at.% C			Temperature, °C	Reaction type
Stable Fe-C (graphite) system					
g ↔ L		0		2862	Boiling
L ↔ δFe		0		1538	Melting
δFe ↔ γFe		0		1394	Allotropic
γFe ↔ αFe		0		912	Allotropic
L + (δFe) ↔ (γFe)	2.43	0.40	0.74	1493	Peritectic
(γFe) ↔ (αFe) + (C)	2.97	0.096	100	740	Eutectoid
L ↔ (γFe) + (C)	17.1	9.06	100	1153	Eutectic
g ↔ C (graphite)		100		3827	Sublimation
Metastable Fe-Fe_3C (cementite) system					
(γFe) ↔ (αFe) + Fe_3C	3.46	0.104	25	727	Eutectoid
L ↔ (γFe) + Fe_3C	17.3	9.23	25	1147	Eutectic
L ↔ Fe_3C		25		1252	Congruent

Fe-C Crystal Structure Data

Phase	Composition, at.% C	Pearson symbol	Space group	Strukturbericht designation	Prototype
(δFe)	0 to 0.4	*cI*2	$Im\bar{3}m$	*A*2	W
(γFe)	0 to 9.06	*cF*4	$Fm\bar{3}m$	*A*1	Cu
(αFe)	0 to 0.096	*cI*2	$Im\bar{3}m$	*A*2	W
(C)	100	*hP*4	*P*6$_3$/*mmc*	*A*9	C(graphite)
Metastable/high-pressure phases					
(εFe)	0	*hP*2	*P*6$_3$/*mmc*	*A*3	Mg
Martensite	<9	*tI*4	*I*4/*mmm*	*L'*2	...
Fe_4C	20	*cP*5	$P\bar{4}3m$	...	...
Fe_3C (θ)	25	*oP*16	*Pnma*	$D0_{11}$	Fe_3C
Fe_5C_2 (χ)	28.6	*mC*28	*C*2/*c*	...	...
Fe_7C_3	30	*hP*20	*P*6$_3$*mc*	$D10_2$	Fe_3Th_7
Fe_7C_3	30	*oP*40	*Pnma*	...	...
Fe_2C (η)	33.3	*oP*6	*Pnnm*	...	...
Fe_2C (ε)	33.3	*hP**	*P*6$_3$22	...	...
Fe_2C	33.3	*hP**	$P\bar{3}m1$	...	...
(C)	100	*cF*8	$Fd\bar{3}m$	*A*4	C(diamond)

Note: Key references for Fe-C crystal structure data are [28Wes], [43Pet], [50Jac], [56Pin], [64Her], [66Jac], [68Dug], [69Fru], and [72Hir].

Table 2. Crystal structure data for the Iron-Chromium system (ASM 2, 1990)

Fe-Cr Crystal Structure Data

Phase	Composition, at.% Cr	Pearson symbol	Space group	Strukturbericht designation	Prototype
(αFe,Cr)	0 to 100	*cI2*	$Im\bar{3}m$	*A2*	W
(γFe)	0 to 11.9	*cF4*	$Fm\bar{3}m$	*A1*	Cu
σ	44.5 to 50	*tP30*	$P4_2/mnm$	*D8b*	σCrFe

Table 3. Crystal structure data for the Chromium-Carbon system (ASM, 1990)

Special Points of the Cr-C System

Reaction	Composition, at.% C			Temperature, °C	Reaction type
L ↔ Cr		0		1863	Melting
L + C ↔ Cr_3C_2	37	100	40	1813 ± 12	Peritectic
L ↔ Cr_7C_3		30		1768 ± 10	Congruent
L ↔ Cr_7C_3 + Cr_3C_2	32.6 ± 0.6	30	~40	1729 ± 8	Eutectic
L + Cr_7C_3 ↔ $Cr_{23}C_6$	17	28.5	21	1577 ± 16	Peritectic
L ↔ (Cr) + $Cr_{23}C_6$	14 ± 0.5	~0.3	20	1532 ± 12	Eutectic

Cr-C Crystal Structure Data

Phase	Composition, at.% C	Pearson symbol	Space group	Strukturbericht designation	Prototype
(Cr)	0 to 0.3	*cI2*	$Im\bar{3}m$	*A2*	W
$Cr_{23}C_6$	~20 to ~21	*cF116*	$Fm\bar{3}m$	*D84*	$Cr_{23}C_6$
Cr_3C(a)	~25	*oP16*	*Pnma*	*D011*	Fe_3C
Cr_7C_3	~30	*oP40*	*Pnma*	*D101*	Cr_7C_3
Cr_3C_2	~40	*oP20*	*Pnma*	*D510*	Cr_3C_2
CrC(?)	~50	...	...	...	...
(C)	~100	*hP4*	$P6_3/mmc$	*A9*	C(graphite)

Note: Lattice parameter data can be found in [26Wes], [28Wes], [33Hel], [33Sau], [33Wes], [59Kos], [64Ste], [65Mon], [70Rou], [74Pra], and [79Ino]. (a) Metastable.

Table 4. Binary solid phases in the Chromium-Carbon and Iron-Chromium systems (Rivlin, 1984)

System	Formula	Crystal structure
C—Cr	(Cr)	bcc (A2)
	$Cr_{23}C_6$	Complex fcc, $D8_4$, 116 atoms/unit cell $a = 1.0655$ nm
	Cr_7C_3	Hexagonal, 80 atoms/unit cell $a = 1.401$ nm, $c = 0.4525$ nm
	Cr_3C_2	Orthorhombic, $D5_{10}$, 20 atoms/unit cell $a = 1.147$ nm, $b = 0.5545$ nm, $c = 0.2830$ nm
	C	Hexagonal (A9, graphitic)
Cr—Fe	(Cr)	*see* above
	σ or FeCr	Tetragonal, $D8_b$, 30 atoms/unit cell $a = 0.87995$ nm, $c = 0.45442$ nm (at 44.7%Cr)

Table 5. Tie-lines in the Iron-Chromium-Carbon ternary system at 770, 750, and 700°C (Rivlin, 1984)

Temperature, °C		Composition, wt-% C	Cr
770	γFe	0.48	0.52
	αFe	0.01	0.31
	γFe	0.46	0.99
	αFe	0.01	0.56
	γFe	0.73	0.69
	M_3C	6.73	8.52
	γFe	0.67	1.11
	M_3C	6.77	15.58
750	γFe	0.57	0.52
	αFe	0.02	0.29
	γFe	0.72	0.64
	M_3C	6.74	10.65
700	αFe	0.01	0.12
	M_3C	6.71	4.44
	αFe	0.01	0.14
	M_3C	6.74	10.00
	αFe	0.01	0.34
	M_3C	6.76	14.85

Table 6. Parabolic rate constants (k_p) for the individual alloy layers and the total alloy layer as a function of initial decarburization

Alloy Layer	No Decarburization ($\mu m/h^{1/2}$)	200μm Decarburization ($\mu m/h^{1/2}$)	400μm Decarburization ($\mu m/h^{1/2}$)
Total	1.0869	1.0914	1.0105
M_7C_3 (layer#1)	0.1238	0.1052	0.1188
M_7C_3 + M_3C (layer #2)	0.3288	0.2994	0.2300
M_3C (layer #3)	0.6343	0.6869	0.6618

Table 7. Calculated interdiffusion coefficients for the total alloy layer growth from previous research and the present work. The values are given as functions of carbon content and temperature of diffusion.

Carbon Content (wt %)	Temperature of Diffusion (°C)	Interdiffusion Coefficient (cm^2/sec)	Reference
0.04	950	$2.6x10^{-10}$	Menzies and Mortimer (1966)
0.16	950	$7.0x10^{-11}$	"
0.20	1000	$4.0x10^{-11}$	Zancheva et al., (1978)
0.20	700	$8.3x10^{-13}$	Present work

Table 8. Actual compositional values from the probe trace according to the Bastin PROZA Phi(ρz) correction scheme. The asterisk denotes the one data point not within the 2% acceptable error.

Distance from the top of the Coating (μm)	Iron Content (wt.%)	Chromium Content (wt %)	Carbon Content (wt %)	Sum of Weight Percents
1	0.14	98.17	2.44	100.75
2	0.15	96.74	3.09	99.98
3	0.10	97.09	2.78	99.97
4	0.15	95.45	3.56	99.16
5	0.14	95.69	3.81	99.64
6	0.15	95.18	3.42	98.75
7	0.16	95.37	3.38	98.91
8	0.18	95.33	2.74	98.25
9	0.22	94.43	4.02	98.67
10	0.37	93.41	5.02	98.80
11	0.73	88.71	8.98	98.42
12	2.27	86.56	9.64	98.47
13	9.32	79.82	9.45	98.59
14	25.85	63.95	8.48	98.28
15	35.97	54.82	8.26	99.05
16	54.04	35.70	7.99	97.73*
17	46.90	42.99	8.25	98.14
18	81.20	12.22	6.52	99.94
19	87.82	5.39	6.19	99.40
20	91.58	2.78	6.06	100.42
21	89.51	4.18	6.15	99.84
22	92.03	1.99	6.09	100.11

Table 8 (cont). Actual compositional values from the probe trace according to the Bastin PROZA Phi(ρz) correction scheme.

Distance from the top of the Coating (μm)	Iron Content (wt %)	Chromium Content (wt %)	Carbon Content (wt %)	Sum of Weight Percents
23	90.41	3.15	6.21	99.77
24	91.04	2.87	6.63	100.54
25	92.29	1.56	6.54	100.39
26	94.11	1.27	4.36	99.74
27	99.21	0.78	1.27	101.26
28	98.91	0.63	1.19	100.73
29	98.89	0.63	1.49	101.01
30	99.48	0.54	1.26	101.28
31	98.82	0.43	1.30	100.55
36	98.79	0.36	0.87	100.02
41	99.12	0.22	0.70	100.04
46	99.46	0.17	0.72	100.35

Table 9. Summary of the equilibrium phases found after 200 hours of exposure at 700°C

Original Layer Name	True Layer Identity	Range of Fe Content (wt %)	Range of Cr Content (wt %)	Range of C Content (wt %)
ABCD plate	$\alpha Cr + M_{23}C_6$	trace	98.17 - 93.41	2.44 - 5.02
Layer #1	M_7C_3	trace - 9.32	88.71 - 79.82	8.98 - 9.45
Layer #2	$M_7C_3 + M_3C$	25.85 - 46.90	63.95 - 42.99	8.48 - 8.25
Layer #3	M_3C	81.20 - 94.11	12.22 - 1.27	6.52 - 4.36
Substrate	αFe	99.21 - 99.46	trace	1.27 - trace

Vita

Richard Paul Baron was born to Ronald and Carol Baron on September 21, 1971. He has one older brother, Jeffrey, one younger brother, Gregory, and one younger sister, Cassandra. He grew up in Alden, Pennsylvania, a suburb of a suburb, and attended John S. Fine Senior High School in Nanticoke, Pennsylvania. After high school, he attended Lehigh University where he graduated with high honors with a Bachelor of Science in Materials Science and Engineering in May, 1993.

Qualifing for the five year BS/MS in materials science, Richard immediately entered graduate school at Lehigh University. The fruits of his labor are exhibited in this thesis.

Upon completion of the current research, Richard will further his education in materials science and engineering at the University of Virginia. Someday, he plans on entering the "real world" and finding a job.

END OF TITLE